Automated Segmentation in 3D Pediatric Echocardiographic Images

Maartje Nillesen

Automated Segmentation in 3D Pediatric Echocardiographic Images Maartje Nillesen

AUTOMATED SEGMENTATION IN 3D PEDIATRIC ECHOCARDIOGRAPHIC IMAGES

MAARTJE M. NILLESEN

Automated segmentation in 3D pediatric echocardiographic images
Nillesen, Maartje M.
Thesis, Radboud University Nijmegen

ISBN 978-90-9025416-6

Typesetting in LaTeX 2_{ε}
Cover design by Jan Kees Schelvis (www.schelvisontwerp.nl)
Printed by Ipskamp Drukkers, Enschede, the Netherlands

AUTOMATED SEGMENTATION IN 3D PEDIATRIC ECHOCARDIOGRAPHIC IMAGES

Een wetenschappelijke proeve op het gebied van de
Medische Wetenschappen

Proefschrift

ter verkrijging van de graad van doctor
aan de Radboud Universiteit Nijmegen
op gezag van de rector magnificus prof. mr. S. C. J. J. Kortmann,
volgens besluit van het college van decanen
in het openbaar te verdedigen op maandag 5 juli 2010
om 15.30 uur precies

door

Maartje Marjolein Nillesen
geboren op 15 februari 1974
te Heemstede

Promotores

Prof. dr. ir. J. M. Thijssen

Prof. dr. R. de Groot

Copromotores

Dr. ir. C. L. de Korte

Dr. L. Kapusta

Manuscriptcommissie

Prof. dr. C. C. A. M. Gielen

Prof. dr. J. L. R. M. Smeets

Dr. ir. J. G. Bosch (Erasmus University)

This research has been supported by the Dutch Technology Foundation STW (project 06466) and Philips Medical Systems.

Financial support by the Netherlands Heart Foundation for the publication of this thesis is gratefully acknowledged.

Financial support for the publication of this thesis was kindly provided by:
· Medison
· Philips Medical Systems
· Dutch Technology Foundation STW

Contents

1

INTRODUCTION

1

1.1 Motivation

In children with congenital heart disease, cardiac malformations might induce a chronic volume or pressure overload of the ventricles. In these children, monitoring the heart function at regular intervals is of crucial importance to prevent heart failure: after thickening of the heart muscle (hypertrophy) to compensate for the increased workload, fibrosis of the myocardium might occur. Contrary to hypertrophy, fibrosis is an irreversible process that reduces the contractility of the heart muscle and may eventually lead to heart failure. Although the incidence of congenital heart disease in the neonatal age remained stable over the past decades, the population of patients in western countries with congenital cardiac malformations is steadily growing due to successful cardiac surgery. Hence, the demand for reliable, non-invasive diagnostic methods for monitoring patients with a (congenital) heart disease has become evident.

During the past decade, echocardiography has become a very competitive imaging modality because of its non-invasive nature and high temporal resolution. With the introduction of real-time 3D echocardiography, assessments of the 3D geometry of the heart and of wall deformation without geometrical assumptions were made possible. Investigation of the exact three-dimensional geometry is extremely important in children with cardiac malformations. The extra information present in 3D echocardiography (compared to 2D echocardiography) might be very helpful in clinical decision making in these children.

Although an experienced cardiologist is able to diagnose most congenital malformations by visual inspection, quantitative analysis of the heart function is required to derive clinically relevant parameters such as cardiac output and strain. The latter stands for the relative deformation of the heart muscle. Since manual analysis of 3D echocardiographic images to derive these parameters is tedious and subject to intra- and inter-observer variability, automated analysis might be preferred. In this thesis, the research was focused on automated assessment of the 3D geometry of the heart without relying on strong geometrical assumptions about the shape of the cardiac structures. This enables analysis of cardiac anatomies that do not satisfy the average standard adult heart geometry as well as of cardiac structures other than the left ventricle. To fully exploit the possibilities of real-time 3D echocardiography, temporal information was incorporated as an additional feature in the mathematical procedures to assess the three-dimensional dynamic structures of the heart.

1.2 Ultrasonic imaging

1.2.1 Ultrasound imaging principles

Ultrasonic imaging is performed by transmitting and receiving high frequency ultrasound (> 20 kHz). Ultrasound waves are reflected or scattered at boundaries between materials with different acoustic impedance (ratio between mass density and speed of sound) e.g. air, blood, bone and soft tissue. The development of ultrasonic imaging started off with the discovery of the piezo-electric effect [Curie and Curie 1880a,b]. The elements of an ultrasound transducer consist of piezo-electric material. When a changing electrical field is applied to such a material, it starts vibrating. If the frequency is sufficiently high, ultrasound waves are emitted. Conversely, when ultrasound waves hit the material, a mechanical deformation is converted into an electric voltage. The piezoelectric effect can thus be used to transmit and receive ultrasound beams. Since the average speed of sound through soft biological tissue is approximately constant (1540 m/s), the time between transmission of the sound wave and receiving the echo can be directly related to the distance between source and reflector.

Throughout the years, various imaging modes have been developed for ultrasonic imaging of the heart. By receiving echos from different depths, a one-dimensional (1D) image line (A-mode) can be displayed. To study the motion of the underlying tissue, for example opening and closing valves in the heart, an M-mode (motion-) image can be generated by recording this image line over time [Edler and Hertz 1954]. A so-called B-mode (brightness-) image is built up by transmitting and receiving ultrasound beams under different angles and combining them to a single two-dimensional (2D) image. In the early period, B-mode imaging was performed by sweeping the ultrasound beam mechanically. Nowadays, real-time 2D imaging without moving the transducer is possible using different kinds of array transducers. Linear array transducers contain an array of acoustic elements and subgroups of adjacent elements are electronically switched on and off in sequence to obtain a 2D image without moving the transducer itself. Phased-array transducers use all the elements quasi synchronously and, by varying the short time-delays between the activation of neighboring elements, steer and focus the ultrasound beam under a certain angle.

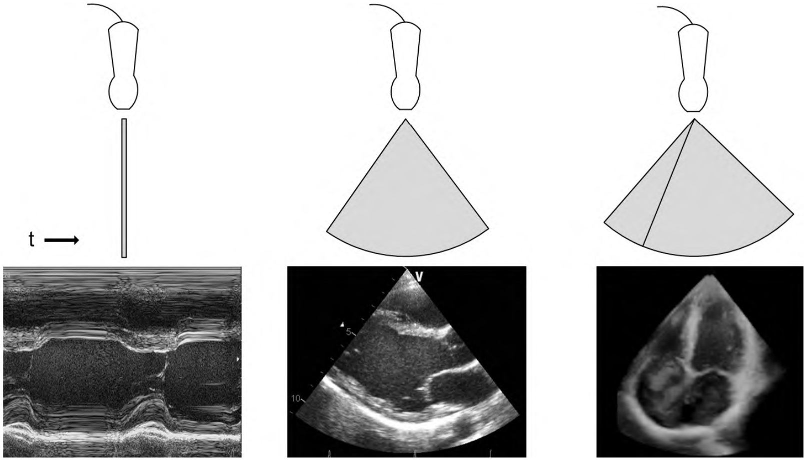

Figure 1.1: Development of echocardiography: from 1D to 3D. *Left*: an M-mode (motion) image, showing a one-dimensional image line over time. *Middle*: A two-dimensional B-mode (brightness) image, showing a cross-section of the left ventricle. *Right*: 3D echographic four-chamber view of the heart.

By analogy with the extension from 1D to 2D ultrasound imaging, a three-dimensional (3D) image volume can be reconstructed from subsequently acquired 2D image planes by manually (freehand scanning) or mechanically moving a 2D transducer. The first mechanical 3D scanner was designed by Kretz Technik (Zipf, Austria), the Combison system (1989). Currently, 3D real-time imaging is available by using matrix array transducers. These transducers contain a 2D array of tiny elements and use 3D electronic beam steering throughout the entire 3D image volume. Figure 1.1 illustrates the development of echocardiograpic imaging from 1D to 3D.

1.2.2 Ultrasound image characteristics

The quality of ultrasound images depends partly upon the characteristics of the ultrasound transducer. The axial image resolution of an ultrasound image is directly related to the frequency bandwidth, corresponding to the duration of transmitted ultrasound pulse. A large bandwidth implies a high axial resolution. Since in practice the resonance frequency / bandwidth ratio (Q-factor) is fixed, the axial resolution is indirectly also increasing with increasing resonance frequency of a transducer. However, there is a trade-off between frequency and penetration depth of the ultrasound beam: the higher the frequency (i.e., resolution), the stronger the attenuation of the ultrasound beam (i.e., decrease of penetration depth). Transducers with transmit frequencies of 2-4 MHz are typically used for echographic imaging of the adult heart, enabling penetration depths of 10-15

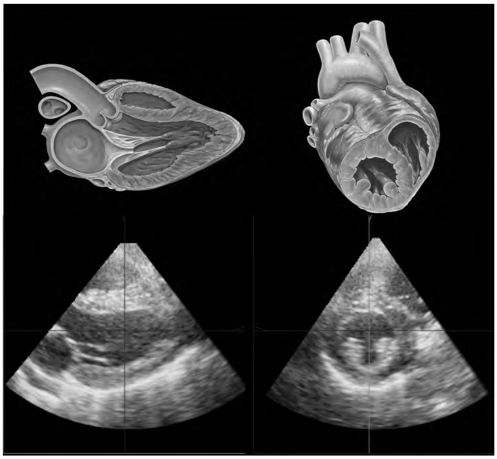

Figure 1.2: Anatomical cross-sections *(upper panel)* of the left ventricle and corresponding two-dimensional cross-sections obtained from a 3D (pediatric) echocardiographic volume *(lower panel)*. *Left panel*: long-axis view of the left ventricle with mitral valve, trabeculations and part of the left atrium. *Right panel*: mid-cavity short-axis view of the left ventricle with papillary muscles and part of the right ventricle. Anatomical illustrations: courtesy of CC Patrick J. Lynch and C. Carl Jaffe, Yale University, 2006.

cm. In pediatric echocardiography, slightly higher frequencies can be used (2-7 MHz) because of the smaller size of the pediatric heart. The overall width of the transducer elements used for a transmit beam influences the width of the focused beam. Furthermore, the resonance frequency and the depth of the transmit focus are influencing the lateral size of the beam in focus and thereby determine the lateral resolution. The volume corresponding to the axial, lateral and elevational beam sizes in focus is called the resolution cell of the transducer. The number of beams that can be transmitted and received per second is limited by the speed of sound. Therefore, the number of frames that can be acquired per second (frame rate) is limited by the pulse repetition frequency, the required depth range and by the number of lines per frame.

Ultrasound images from scattering media, such as tissues, are characterized by the presence of speckle. This granular pattern arises from inhomogeneities and structures with dimensions smaller than the resolution cell of the ultrasound beam and it degrades resolution and adds spatial noise to the images. The granularity of the speckle pattern results from interference that occurs at reception of the backscattered ultrasound waves. Although the speckle pattern that is seen in ultrasound images does not visualize underlying structure directly in most healthy tissues, the local echogenicity corresponds to the scattering level and number density of the underlying scatterers. The texture of the speckle pattern depends on the spatial distribution of the scatterers. Speckle statistics might, therefore, provide information about tissue structure indirectly. Speckle has a strong influence on the image quality and is therefore often considered as undesired noise. However, speckle can also be considered as a feature that characterizes tissue (micro) structure.

Conventional B-mode images, i.e., the images displayed on the video screen of the ultrasound machine, are derived from the envelopes of raw ultrasound scan lines in radio frequency (RF) format. Construction of a B-mode image consists of several steps: overall gain and time gain compensation (TGC), band pass filtering, amplitude demodulation, log compression, analog to digital conversion and post-processing. Post-processing includes scan-conversion and the transformation to gray levels using a linearized post-processing curve. In B-mode images, the phase information present in the reflected ultrasound beam is discarded. However, this phase information can be of great importance, for example in the field of strain imaging, where the deformation of the tissue is tracked over time by estimating displacements and deformation between subsequent time frames. More accurate displacement estimations can be obtained by adding high-resolution phase information [Varghese and Ophir 1997] present in the RF-signal than by using envelope-based speckle tracking.

1.3 3D echocardiography

By using a 2D matrix array transducer, the entire left ventricle can be acquired at once (3D echography) and any required 2D plane can be selected off-line from this 3D volume (Fig 1.2). Surgeons, who already 'think' in 3D, do no longer have to build up a 3D mental image of the heart by combining 2D images, but they can now look right into a realistic 3D reproduction of the heart.

Real-time 3D echocardiography was introduced in the early 1990s by von Ramm and colleagues [Smith et al. 1991; von Ramm et al. 1991]. They built the first matrix sparse-array transducer consisting of 256 non-simultaneously firing elements, acquiring a pyramidal volume of 60 x 60 degrees. The first commercially available 3D-real time phased array system was also developed by this group (Volumetrics Model 1, Volumetrics Medical Imaging, Durham, NC). Frame rates were low and image quality was still inferior to 2D imaging. Further improvements in engineering led to a next generation transducers, developed by Philips Medical Systems (Andover, USA, 2003) and later on by General Electric (Milwaukee, Wisconsin, USA, 2004). Current matrix array transducers typically contain around 2500 elements and operate in the frequency range from 2 to 7.5 MHz. The Philips SONOS 7500 real-time ultrasound system with the X4 matrix array transducer enables ECG-gated full volume imaging that allows inclusion of a large cardiac volume. Four narrow pyramidical scans (obtained over four to seven consecutive heart beats) are merged to one large pyramidical scan (70 x 76 degree) with a maximal frame rate of 25 Hz. More sophisticated transducer materials and higher frequencies are used in the latest generation of transducers. For example, the iE33

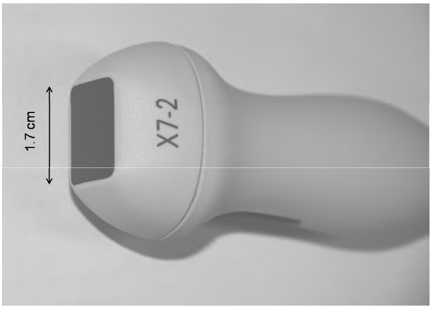

Figure 1.3: A 3D matrix array transducer for pediatric imaging (X7-2, Philips Medical Systems, Bothell, WA, USA)

system (Philips Medical Systems, Andover, USA) with the X7-2 transducer (Fig. 1.3, pediatric) enables ECG-gated full volume imaging of a 90° x 90° volume with a volume rate up to 75 Hz, using four to seven consecutive heart beats.

Although 3D echocardiography is now widely available, conventional 2D echocardiography is often used for functional assessment, e.g., measurement of ejection fraction and cardiac output. As 2D echocardiography lacks information about the spatial arrangement of cardiac structures, the use for volumetric studies is inherently limited and geometrical assumptions about the shape of the ventricle have to be made. Also foreshortening may easily occur as the position of the 2D cross-sectional plane within the 3D heart is not exactly known. In comparison to two-dimensional (2D) echocardiography, 3D echocardiography obviates the necessity for 2D geometrical assumptions. These geometrical assumptions comprise a simplified shape of the ventricle and may lead to inaccurate ventricular function estimation in diseased hearts and in foreshortened 2D images of the ventricle. 3D echocardiographic imaging therefore enables a more accurate assessment of ventricular volume and derived functional parameters as ejection fraction and cardiac output [Gopal et al. 1995; Bruining et al. 2000]. The availability of 3D ultrasound has also boosted the development of 3D "strain" (i.e., relative deformation) imaging techniques as it enables simultaneous estimation of strain in 3 orthogonal directions in the heart muscle. Inaccurate strain estimates due to out-of-plane motion can thus be prevented.

1.4 Automatic analysis of echocardiographic images

3D echocardiography is pre-eminent in visualizing the complex 3D structure of the heart with high temporal resolution. Visual inspection of these images by a trained observer yields insight into the geometry and function of the heart. However, manual analysis of 3D images is time-consuming and the interpretation of the images depends strongly on the interpretation of the expert user. Automated analysis techniques aim at decreasing the inter-observer variability and increas-

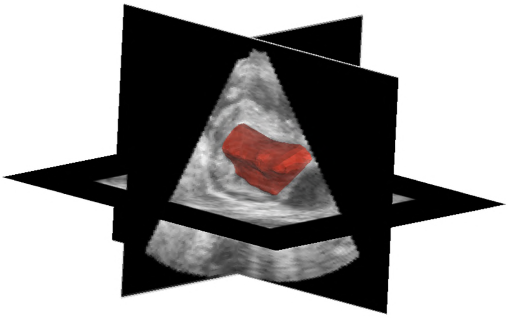

Figure 1.4: A 3D ultrasound image of the left ventricle (view from mitral valve) with the endocardial surface in red. The 3D endocardial surface was obtained by automated segmentation.

ing the reproducibility of the results. Most importantly, the aim of automated analysis is to derive quantitative information from these images. For example, automated segmentation (Fig. 1.4) can be a helpful tool in volumetric studies for the estimation of ventricular volumes and related, clinically relevant parameters such as cardiac output (CO) and ejection fraction (EF). Automated segmentation can also serve as an important pre-processing step in tissue characterization and the automated assessment of functional muscle characteristics by means of strain estimation. Automated segmentation of the left ventricle may thus be a helpful tool for clinical analysis of 3D echocardiographic images and it may substantially support clinical diagnosis of heart disease at an early stage.

Automated segmentation of ultrasound images is a challenging task due to the influence of the speckle noise caused by the interference pattern of received backscattering. The granular appearance of these images makes it difficult to identify the exact border between different media (e.g., blood and myocardial tissue). Also, ultrasound images may suffer from artefacts such as reverberations and shadowing. Reduced contrast between blood and myocardial wall can be expected in regions where the orientation of the muscle fibers is parallel to the propagation direction of the ultrasound beam. In the development of methods for automated segmentation, one should consider these typical ultrasound image characteristics.

Apart from the negative effect of speckle noise on the differentiation of tissues, speckle can also be used a feature that contains information about the underlying tissue and the motion of the tissue. Two-dimensional deformation of the tissue can be assessed by speckle tracking of tissue movement [Bohs and Trahey 1991; Ramamurthy and Trahey 1991; Chaturvedi et al. 1998] or by RF-based strain estimation [Konofagou and Ophir 1998; D'hooge et al. 2002; Sutherland et al. 2004; Lopata et al. 2009]. Once the movement is known, it can be used to track the local position of the tissue and to support the segmentation process.

Many approaches for segmenting the endocardial wall in adult echocardiographic images have been proposed. A detailed overview can be found in Noble and Boukerroui [2006]. Segmentation can be either considered as a region-based or edge-based problem. Region-based methods use the assumption that an image can be described in terms of areas with similar image properties. Bayesian statistics can be used to assess the maximum a posteriori probability in a region based approach [Ashton and Parker 1995; Boukerroui et al. 2003].

Edge-based methods aim at detecting borders between regions. The use of an edge-based method for segmentation of the endocardial wall is not straightforward as the contrast between blood and myocardium depends on the relative orientation of the border to the direction of the ultrasound beam.

Deformable models, also referred to as active contours often use gradient information and can be used to segment the endocardial wall by deforming a contour or surface under internal (elasticity, stiffness) and external (gradient) forces. Deformable models are popular in medical image analysis because of their flexibility to segment structures without a predefined shape. Several methods have been proposed for segmenting 3D echocardiograms using deformable models (amongst others, Angelini et al. [2001]; Gerard et al. [2002]; Montagnat et al. [2003]; Walimbe et al. [2006]).

Level set methods have also been successfully applied for edge-based segmentation of echocardiograms [Corsi et al. 2002; Angelini et al. 2005; Sarti et al. 2005]. Level sets use a similar principle as deformable models to evolve a contour or surface, however the contour or surface is now embedded in a level-set function of a higher dimension. As level sets can handle changes in topology, they can also be used for segmentation of 'splitting objects' for example at bifurcations of the arteries. A combination of edge-based and region-based information, using level sets, can be found in Lin et al. [2003].

Active shape models and active appearance models [Cootes et al. 2001] are also often used in medical image analysis. These models both use object shape and image appearance to build a statistical model and are trained by a set of manually segmented images. These models have been successfully applied for segmentation of the left ventricle in echocardiographic images [Bosch et al. 2002; Hansegard et al. 2007; van Stralen et al. 2007; Leung et al. 2008].

1.5 Outline of this thesis

The ultimate goal of automated analysis of 3D echocardiographic images is to provide objective, quantitative measures of clinically important parameters to support the diagnosis of cardiac disease. Automated segmentation can be used to assess the geometry of the heart with minimal observer interaction. Detection of the endocardial border of the left ventricle is an important step to obtain cardiac output and ejection fraction to monitor global cardiac function and to visualize (congenital) malformations in cardiac anatomy. Furthermore, segmentation is an important pre-processing step for strain imaging. On the other hand segmentation can be combined with strain imaging to perform tracking of the cardiac muscle. Segmentation methods are often based on the assumption of a normal anatomy of the adult heart in standard echo views, which precludes accurate analysis in non-standard images, for example in children with congenital cardiac malformations.

The methods described in this thesis are aiming at automated segmentation in echocardiographic images without incorporating a *priori* knowledge on the average shape of the heart. Also a new RF-based feature that uses temporal correlation was introduced to improve segmentation in echocardiographic images.

As a first step towards automated segmentation of echocardiographic images, we have looked into the field of speckle statistics. In chapter 2, we investigated the envelope statistics of *in vivo* normal myocardial tissue and blood in echocardiographic images by fitting statistical distributions to the image gray level histogram. Knowledge about the speckle statistics of the demodulated RF-data could serve as valuable information for classifying tissue and thus for automated segmentation. Parametric imaging is performed to study the capability of the parameters of the best fitting distribution to differentiate blood from myocardium. The most promising parameter is used in an edge preserving, speckle reduction technique. This so-called adaptive filtering procedure uses local information to steer the degree of low pass filtering and it results in less speckle noise in homogeneous regions and in the preservation of image information at edges.

Chapter 3 builds on the knowledge on speckle statistics as obtained in chapter 2. Segmentation in ultrasound imaging is challenging because of the presence of speckle noise. This chapter describes a method to reduce the influence of speckle noise. The method joins knowledge about underlying statistical characteristics of the tissue with the advantage of adaptivity. The effect of adaptive filtering on the distinction between blood and myocardial tissue is studied. We present a semi-3D segmentation method to segment the endocardial surface in 3D images using adaptive filtering. Based on the continuous deformation of the heart, spatio-temporal continuity is incorporated in the method.

Accurate, non-invasive measurement of cardiac output remains a great challenge, in particular in newborn children. In chapter 4, a 3D segmentation method that automatically detects the endocardial surface in 3D images is described. The method is validated quantitatively *in vivo* in an animal model by comparing cardiac output as obtained from the segmented volumes with cardiac output values measured invasively from the volume flow in the pulmonary artery. The method is based on adaptive filtering and a deformable model and is tested in non-standard echocardiographic images.

More information can be extracted from echographic images by using the temporal correlation between subsequently acquired images. This temporal information might yield new features that can optimize the distinction between different structures such as blood vs. myocardial tissue and could thus facilitate the segmentation process. Correlation-based techniques are widely used for displacement and strain estimation to measure the deformation of tissue. Chapter 5 describes a method for displacement and strain estimation using phased array 2D RF-data. The performance of the method is tested by a simulation and a phantom study.

Chapter 6 studies the feasibility of using the cross-correlation values as derived in chapter 5 as a new feature for segmentation of the endocardial surface. The technique is based on the principle that the motion of the blood in the ventricles is faster than the motion of the surrounding myocardial tissue.

Chapter 7 builds on the results described in chapter 6 and is devoted to a segmentation method that uses 3D correlation techniques. The correlation values are used as an additional feature in the segmentation process. The method is evaluated in pediatric echocardiographic images.

Finally, Chapter 8 concludes this thesis with a discussion of the investigated methods and recommendations for future research.

2

MODELING ENVELOPE STATISTICS OF BLOOD AND MYOCARDIUM FOR SEGMENTATION OF ECHOCARDIOGRAPHIC IMAGES

Based on: M. M. Nillesen, R. G. Lopata, I. H. Gerrits, L. Kapusta, J. M. Thijssen, and C. L. de Korte. Modeling Envelope Statistics of Blood and Myocardium for Segmentation of Echocardiographic Images. *Ultrasound Med Biol* 34(4):674-680, 2008.

2

Abstract

The objective of this study was to investigate the use of speckle statistics as a preprocessing step for segmentation of the myocardium in echocardiographic images. Three-dimensional (3D) and biplane image sequences of the left ventricle of two healthy children and one dog (beagle) were acquired. Pixel-based speckle statistics of manually segmented blood and myocardial regions were investigated by fitting various probability density functions (pdf). The statistics of heart muscle and blood could both be optimally modeled by a K-pdf or Gamma-pdf (Kolmogorov-Smirnov goodness-of-fit test). Scale and shape parameters of both distributions could differentiate between blood and myocardium. Local estimation of these parameters was used to obtain parametric images, where window size was related to speckle size (5 × 2 speckles). Moment-based and maximum-likelihood estimators were used. Scale parameters were still able to differentiate blood from myocardium; however, smoothing of edges of anatomical structures occurred. Estimation of the shape parameter required a larger window size, leading to unacceptable blurring. Using these parameters as an input for segmentation resulted in unreliable segmentation. Adaptive mean squares filtering was then introduced using the moment-based scale parameter (σ^2/μ) of the Gamma-pdf to automatically steer the two-dimensional (2D) local filtering process. This method adequately preserved sharpness of the edges. In conclusion, a trade-off between preservation of sharpness of edges and goodness-of-fit when estimating local shape and scale parameters is evident for parametric images. For this reason, adaptive filtering outperforms parametric imaging for the segmentation of echocardiographic images.

2.1 Introduction

Echocardiographic imaging is a noninvasive imaging technique that has high temporal resolution and important diagnostic capabilities. Recent developments in transducer design have led to improved image quality. However, ultrasound images from scattering media, such as tissues, are characterized by the presence of speckle, a granular pattern that degrades resolution and adds spatial noise to the images. In addition to undesirable shadows and dropouts in structures that are parallel to the propagation direction of ultrasound, the speckle has a strong influence on image quality. Interpretation of speckle might be twofold. Speckle often is considered as noise and, therefore, as an undesirable characteristic that seriously affects image quality. However, speckle can also be considered as a feature that characterizes tissue (micro) structure.

The granularity of the speckle pattern results from interference that occurs at reception of the backscattered ultrasound waves. Although the speckle pattern that is seen in ultrasound images does not visualize underlying structure directly in most healthy tissues, the local echogenicity corresponds to the scattering level and number density of the underlying scatterers. The texture of the speckle pattern depends on the spatial distribution of the scatterers. Speckle statistics might, therefore, provide information about tissue structure indirectly.

Automatic segmentation of ultrasound images is a challenging task due to the influence of the speckle noise. Segmentation of the heart muscle within echocardiographic images is an important preprocessing step for both volumetric studies and tissue characterization. Segmentation can be a helpful tool to visualize abnormalities in cardiac anatomy and to assess cardiac function and composition. When segmenting ultrasound images, it is a choice to either reduce the speckle or to profit from the information contained in the speckle pattern. A number of speckle reduction techniques have been investigated in literature (see Verhoeven and Thijssen [1993] for a survey).

Speckle statistics of biological tissue have been described by various probability density functions (pdfs). Tissue can be modeled as randomly distributed, discrete point scatterers [Wagner et al. 1983; Burckhardt 1978; Thijssen 2003]. The most commonly used pdf to describe the statistic of the envelope signal is the Rayleigh distribution [Jakeman and Tough 1987]. This distribution only fits well to the echo envelope data when the speckle is fully developed, i.e., the resolution cell of the system contains a large number of randomly distributed scatterers. The Rayleigh pdf is leading to a pixel signal-to-noise ratio (SNR) of 1.91. However, in most cases the speckle statistics are sub-Rayleigh ($SNR < 1.91$).

The K distribution has been proposed for structures having a smaller "effective" number of scatterers per resolution cell [Jakeman and Pussey 1976; Shankar 1995]. It was shown that speckle statistics of myocardium [Clifford et al. 1993], breast and liver [Molthen et al. 1998] can be described well by this distribution. Other distributions describing speckle statistics are Rician [Rice 1948], Weibull

Weibull [1951], (generalized) Gamma [Stacy 1962] and Nakagami [Nakagami 1960] distributions. Once the underlying statistical process is known to be modeled well by one of the distributions, parameters of this distribution might be used to generate parametric images or maximum a posteriori (MAP) filtering [Ashton and Parker 1995] could be applied to reduce the speckle. The parameters could also serve as the input for an adaptive filtering process [Bamber and Daft 1986]. In each of these cases, the speckle pattern is seen as a feature that contains information about underlying tissue that can be implicitly used to facilitate segmentation. One of the difficulties when using the statistical parameters for segmentation purposes is that an optimal fit of the pdf to the data requires a large data set from a homogeneous tissue. In practice, when using parametric imaging or MAP filtering, the risk of undesired blurring of edges of anatomical structures limits the size of the data set (image window) that can be used for fitting the pdf.

In this study, speckle statistics of *in vivo* normal myocardium and left ventricular blood pool regions were investigated. Five different pdfs were fitted to the data and statistical analysis was used to determine which pdf best models the backscattering characteristics of blood and myocardium. Shape and scale parameters of the best fitting distributions were visualized and compared for both myocardial and blood pool regions. Parametric imaging was performed to study the capability of the parameters to differentiate blood from myocardium as a first step in segmentation of the myocardium. The most promising parameter was used in an adaptive filtering procedure to reduce the speckle noise.

Probability density functions that model the backscattered envelope from tissues in ultrasound images have been elaborately described in recent literature [Eltoft 2006; Raju and Srinivasan 2002]. For this reason, only short descriptions of the five candidate pdfs are given in this article.

Rayleigh Distribution

The probability density function of the envelope, $p(x)$, under the Rayleigh model is given by:

$$p(x) = \frac{x}{s^2} e^{-\left(\frac{x^2}{2s^2}\right)} \qquad (x \geq 0; s > 0) \tag{2.1}$$

where x is the demodulated signal and s^2 is the signal power. The maximum likelihood estimator for s^2 is given by:

$$s^2 = \frac{1}{2n} \sum_{i=1}^{n} {x_i}^2 \tag{2.2}$$

The central limit theorem implies that for a scattering medium containing a large number ($n \geq 10$ per resolution cell) of randomly distributed scatterers, the backscattered radio-frequency (RF) echo signals are Gaussian distributed and the signal envelope follows a Rayleigh distribution [Burckhardt 1978; Jakeman and Tough 1987; Papoulis 1976].

K Distribution

It has been shown that when the resolution cell contains relatively few scatterers or the scatterers have randomly varying cross sections, the K distribution provides a good fit to the backscattered envelope [Jakeman and Pussey 1976]. The pdf of the K distribution is given by:

$$p(x) = \frac{2}{a\Gamma(v+1)} \left(\frac{x}{2a}\right)^{v+1} K_v \left(\frac{x}{a}\right) \qquad (x \geq 0, a > 0, v > -1) \tag{2.3}$$

where: a is the scale parameter.
Γ is the Gamma function and K is the modified Bessel function of the second kind of order v. The parameter v is the shape parameter, and $v+1$ denotes the effective number of scatterers in the resolution cell [Shankar 1995].

The parameters a and v can be estimated using second and fourth order moments. This moment-based method only works for large data sets. Maximum-likelihood methods lead to accurate parameter estimation but are computationally expensive. Iskander et al. [1999] proposed a new method that combines the moments method with the maximum likelihood principle resulting in accurate and computationally nonexpensive parameter estimates.

Gamma Distribution

The Gamma distribution shows some similarity with the K distribution but is analytically less complex and its pdf is given by:

$$p(x) = x^{k-1} \frac{e^{-\frac{x}{\theta}}}{\theta^k \Gamma(k)} \tag{2.4}$$

The scale parameter θ and shape parameter k can be estimated by maximum-likelihood estimation. Moment-based estimators for θ and k are given by:

$$\theta = \frac{s^2}{\bar{x}} \tag{2.5}$$

$$k = \left(\frac{\bar{x}}{s}\right)^2 \tag{2.6}$$

with $\bar{x}$ the sample mean and s^2 the sample variance. The Gamma distribution is a special case of the generalized Gamma distribution that has already been used to model speckle statistics [Raju and Srinivasan 2002]. The Gamma distribution is analytically less complex than K- and generalized Gamma distributions.

Nakagami Distribution

The Nakagami distribution has been proposed in literature as a model to describe the statistics of the backscattered envelope from scatterers with varying cross sections and number densities [Shankar 2000]. This distribution only requires partial correlation between the scatterers. The Nakagami distribution is given by:

$$p(x) = \frac{2m^m x^{2m-1}}{\Gamma(m)\Omega^m} e^{-\frac{m}{\Omega}x^2} \tag{2.7}$$

with m the Nakagami parameter and Ω the scale parameter, representing the average power of the envelope. Ω can be estimated by:

$$\Omega = \frac{1}{n}\sum_{i=1}^{n} {x_i}^2 \tag{2.8}$$

The Nakagami parameter m can be estimated by maximum likelihood estimation [Kolar et al. 2004]. The Nakagami distribution includes the Rayleigh distribution as a special case ($m = 1$) and if the variate x follows a Nakagami distribution, then x^2 follows a Gamma distribution.

Inverse Gaussian Distribution

The inverse Gaussian distribution was not described in literature as a candidate pdf for backscattered envelope but was derived empirically by the authors as a possible model. The pdf $p(x)$ and maximum likelihood estimator λ are given by:

$$p(x) = \sqrt{\frac{\lambda}{2\pi x^3} e^{-\frac{\lambda(x-\mu)}{2x\mu^2}}} \qquad (x > 0) \tag{2.9}$$

$$\lambda = \frac{n}{\sum_{i=1}^{n}\left(\frac{1}{x_i} - \frac{1}{\bar{x}}\right)} \tag{2.10}$$

2.2 Materials and Methods

Echocardiographic images of two children and one beagle were obtained. The two healthy children (8- and 10-y old) were referred to the pediatric cardiology department for the exclusion of heart disease (cardiomyopathy) and appeared to be cardiologically normal, as assessed by an experienced pediatric cardiologist (LK). The parents gave their informed consent for using the echographic data for this research project. Echographic imaging of the beagle was approved by the local animal ethics committee. Image sequences of the left ventricle were taken using transthoracic short and long axis views. RF-data were acquired using a Philips SONOS 7500 live three-dimensional (3D) ultrasound system (Bothell, WA,

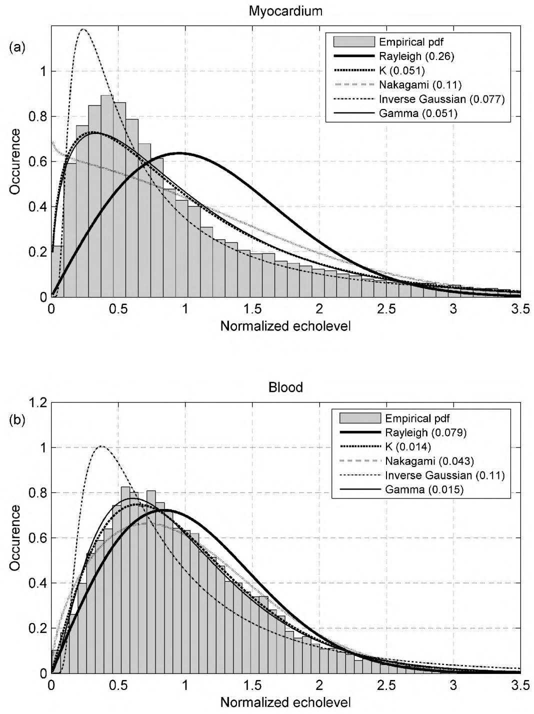

Figure 2.1: Histograms of empirical data (beagle) of myocardial (a) and blood (b) regions and probability density functions fitted to the data. The data were normalized such that $\mu = 1$. Areas under the histograms and pdfs were normalized to unity. The values between brackets in the legend denote Kolmogorov-Smirnov (KS) goodness of fit errors.

USA), equipped with an RF-interface and an X4 matrix array transducer (2 to 4 MHz). Beagle data were obtained in biplane mode (an image mode in which two perpendicular planes are acquired), with an axial depth span of 7.5 cm and consisting of 62 lateral and elevational lines. The human data were acquired in 3D live mode (an image mode that provides real-time 3D data for a reduced volume) with an axial depth span of 8.5 cm, containing 46 lateral and 18 elevational lines. RF-data were sampled at 19.5 MHz and were transmitted to a workstation (Hewlett-Packard Nederland, Utrecht, The Netherlands) using a USB 2.0 interface. For the analysis of the speckle statistics we used 11 axial-lateral planes of the beagle data and for each child 5 axial-lateral planes were selected from the 3D live data sets. Matlab (The MathWorks Inc., Natick, MA, USA) was used to perform all calculations.

The RF-data were band-pass filtered (FIR least squares filter [2 to 3.6 MHz]) and amplitude demodulated using the Hilbert transform. Blood and myocardial regions were interactively segmented in the two-dimensional (2D) axial-lateral image plane by an experienced pediatric cardiologist (LK). Rayleigh, K, inverse Gaussian, Nakagami and Gamma pdfs were fitted to 100-bin histograms of the pixels contained in these regions to compare the suitability of these pdfs with the data. For each region, the data were normalized such that $\bar{x} = 1$, and all histograms were normalized to unity. The goodness-of-fit for each of these pdfs was tested by evaluating the sum of the absolute differences between empirical and candidate pdf and the Kolmogorov-Smirnov (KS) error, which is defined as the maximum absolute difference between the empirical cumulative distribution function (cdf) and the candidate cdf [Conover 1980]. These two test-statistics were used as a relative goodness-of-fit measure to rank the candidate pdfs.

Scale and shape parameters of the pdfs best fitting to the data were compared for blood pool and myocardial regions. Statistical analysis (Wilcoxon rank sum test) was performed to test whether these parameters could differentiate between blood and myocardium.

Parametric imaging was performed for the most suitable pdfs. Shape and scale parameters were imaged by using a sliding kernel technique. The 2D sector image of the phased array scanning device was processed along the scan lines to maintain the lateral speckle size depth independency [Oosterveld et al. 1985; Valckx et al. 2000]. For this reason, fixed kernel dimensions could be chosen for all depths. Kernel size was related to speckle size (5 x 2 speckles). Obviously, there is a trade-off between preservation of spatial resolution and wanted statistical properties.

The most promising parameter of the Gamma distribution, the moment-based scale parameter $s^2/\bar{x}$ (estimate of θ, eqn 2.5) was incorporated in an adaptive mean squares (AMS) speckle reduction filtering technique (Chapter 3). This filter uses the scale parameter that represents the homogeneity of the tissue, to automatically steer the degree of filtering. Therefore, the sharpness of the edges of various structures was preserved since regions that contain edges are inhomogeneous and will be less smoothed than homogeneous areas.

2.3 Results

Blood pool and myocardial regions were segmented manually for 11 biplane data sets of one healthy beagle and five axial-lateral planes of 3D live data sets of each healthy child. Figure 2.1 shows the histogram of empirical data of myocardial and blood regions with corresponding representative pdf fits for five distributions. For the myocardial region, it can be seen that the histogram of the empirical data were sub-Rayleigh and consistently, the Rayleigh distribution fitted poorly to the data. Both the K- and the analytically simpler Gamma distribution fitted to the empirical data well and led to small KS errors. The inverse Gaussian and Nakagami distributions did not model the envelope statistics adequately. It can be concluded

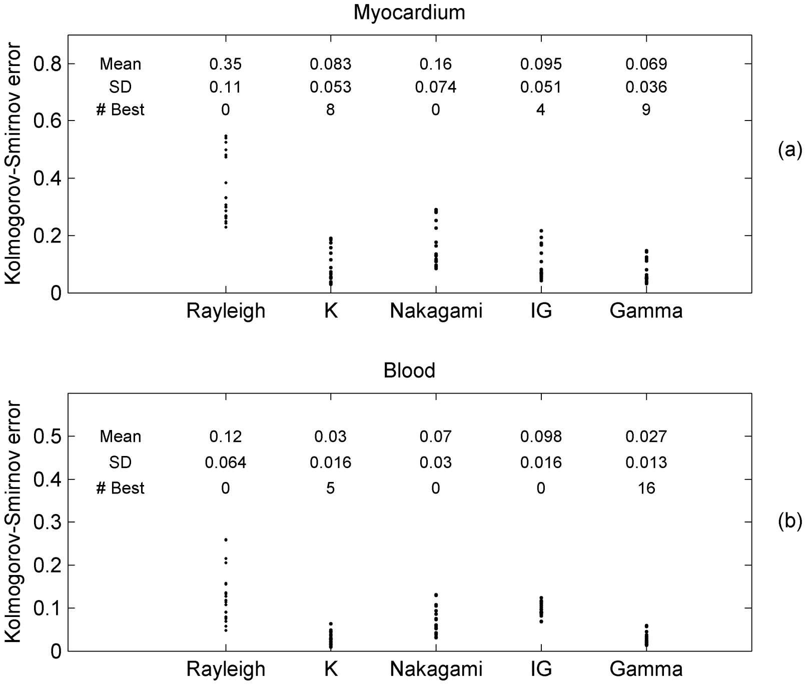

Figure 2.2: Overview of Kolmogorov-Smirnov (KS) goodness of fit values between fitted distributions and empirical data for myocardium (a) and blood (b) for 21 data sets of beagle and human data. Each data point represents a data set. Mean and standard deviation (SD) are given for each pdf.

from the lower panel of Fig. 2.1 that, although envelope statistics of blood were less sub-Rayleigh than envelope statistics of the myocardium, the Rayleigh distribution still yielded a poor fit to the data. As for the myocardial region, Gamma and K distribution provided good fits for the empirical data of the blood region.

KS goodness of fit measures are given in Fig. 2.2 for all candidate distributions for myocardial and blood pool regions. It can be concluded from these measures that the mean KS error is the smallest for the Gamma distribution. This pdf had the smallest KS measure in the majority of the cases. The K distribution also provided a good fit to the data. Tables 2.1 and 2.2 are indicative of the ranking of the pdfs for human and beagle data, respectively. It should be noted that the number of histogram bins affects the absolute value of the KS error, however, the ranking of the pdfs is unaffected.

Only parameters of the K- and Gamma distribution were studied. Parameters

Table 2.1: Sum of the squared differences (SSD) and Kolmogorov Smirnov (KS) test statistic for human myocardium and left ventricular blood pool (*in vivo*). The five candidate pdfs are ranked from 1 (best fit) to 5 for the two test statistics.

Human data		Candidate pdfs				
Tissue type	Error	Rayleigh	K	Nakagami	Inv. Gaussian	Gamma
Myocardium	SSD	5	2	4	3	1
	KS	5	3	4	2	1
Blood	SSD	5	2	3	4	1
	KS	5	2	4	3	1

Table 2.2: Sum of the squared differences (SSD) and Kolmogorov Smirnov (KS) test statistic for myocardium and left ventricular blood pool of beagle data (*in vivo*). The five candidate pdfs are ranked from 1 (best fit) to 5 for the two test statistics.

Beagle data		Candidate pdfs				
Tissue type	Error	Rayleigh	K	Nakagami	Inv. Gaussian	Gamma
Myocardium	SSD	5	2	4	3	1
	KS	5	2	4	3	1
Blood	SSD	4	1	3	5	2
	KS	4	2	3	5	1

of Rayleigh-, Nakagami- and Inverse Gaussian pdfs were not taken into consideration because of their poor fit to the data. Table 2.3 lists average values and standard deviations for shape and scale parameters of the Gamma and K distributions. All parameters were obtained by using maximum-likelihood estimators. A Wilcoxon rank sum test revealed significant differences between blood and myocardial tissue for all parameters ($p < 0.001$).

According to the ranking results in Tables 2.1 and 2.2, fitting results for human data and beagle data hardly show any differences. Table 2.3 shows that there are absolute differences in parameter values for human data compared with beagle data. However, relative differences between parameters for blood and myocardium are comparable for human and beagle data. The parameters of the Gamma distribution showed less variability (5% to 23%) with respect to the mean than parameters of the K distribution. Figure 2.3a shows the original echocardiogram for one data set and Fig. 2.3b and c show parametric images of the scale parameters of the K and Gamma distribution, respectively. The moment-based estimator $s^2/\bar{x}$ was used for estimating the scale parameter of the Gamma distribution, as this method is less complex than maximum-likelihood estimation and, moreover, it yielded similar results. Although the parameters differentiated between blood and myocardium, unacceptable blurring of the edges occurred.

Table 2.3: Average scale and shape parameters for K- and Gamma distributions, differentiated for blood and myocardial regions.

	K distribution		Gamma distribution	
	Shape par. v	Scale par. a	Shape par. k	Scale par. θ
Myocardium (human)	-0.52 ± 0.15	0.48 ± 0.15	1.05 ± 0.24	1.00 ± 0.23
Blood (human)	0.53 ± 0.46	1.53 ± 0.46	2.04 ± 0.25	0.50 ± 0.064
Myocardium (beagle)	-0.18 ± 0.081	0.82 ± 0.081	1.52 ± 0.09	0.66 ± 0.032
Blood (beagle)	2.58 ± 1.81	3.58 ± 1.81	2.54 ± 0.21	0.40 ± 0.033

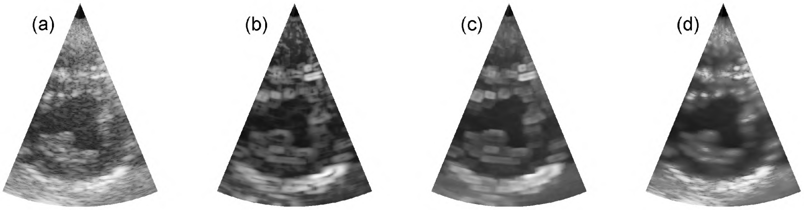

Figure 2.3: Comparison between parametric imaging and adaptive filtering for a single plane of a 3D data set (human). From left to right: (a) unprocessed data, (b) parametric image of scale parameter a of K-distribution, (c) parametric image of moment-based scale parameter of Gamma distribution and (d) data after AMS filtering. Equal window size was used for both parametric imaging and adaptive filtering (5 x 2 speckles).

Using smaller kernel sizes was not a solution to this problem since it resulted in unreliable pdf-fits. However, using the most promising parameter θ in the AMS filtering procedure generated good segmentation results. A representative example of the result of AMS filtering is shown in Fig. 2.3d. The filter clearly reduces speckle noise, while preserving the sharpness of edges of anatomical structures. This leads to an optimized discrimination between blood and myocardium, facilitating further segmentation.

2.4 Discussion and Conclusion

Statistical characteristics of myocardial tissue and blood were investigated for usage in a preprocessing step for segmentation of the myocardium. Clifford et al.

[1993] concluded that the K distribution provides the best fit for backscatter statistics of myocardial tissue. The generalized Nakagami distribution appeared to fit best to envelope statistics of the heart (including myocardium and blood) according to the findings of Eltoft [2006]. However, in a substantial part of the cases, the generalized Nakagami could not be fitted to the data in the latter study, which makes this pdf not a robust model for describing backscatter statistics of the heart.

Although the K distribution provided a good fit for both myocardium and blood in our analysis, the Gamma distribution slightly outperformed the K distribution. In comparison with the K distribution, the Gamma distribution is analytically much simpler and its parameters are easier and more robust to estimate. Therefore, the authors suggest that the Gamma distribution is a more adequate and elegant distribution for describing speckle statistics of blood and myocardium.

This study showed that both scale- and shape parameters of the K- and Gamma distributions are capable in discriminating blood from myocardium. However, the trade-off between preservation of sharpness of edges and goodness-of-fit, when estimating these parameters locally, results in improper segmentation of the myocardium when using parametric imaging. It is concluded that adaptive mean squares filtering, based on the scale parameter of the Gamma distribution, successfully joins knowledge about underlying statistical characteristics of the tissue with the advantage of adaptivity and edge preservation.

Acknowledgements

This work was supported by Philips Medical Systems and the Dutch Technology Foundation (STW), project 06466.

3

SEGMENTATION OF THE HEART MUSCLE IN 3D PEDIATRIC ECHOCARDIOGRAPHIC IMAGES

Based on: M. M. Nillesen, R. G. Lopata, I. H. Gerrits, L. Kapusta, H. J. Huisman, J. M. Thijssen, and C. L. de Korte. Segmentation of the Heart Muscle in 3D Pediatric Echocardiographic Images. *Ultrasound Med Biol*, 33(9):1453-1462, 2007.

3

Abstract

This study aimed to show segmentation of the heart muscle in pediatric echocardiographic images as a preprocessing step for tissue analysis. Transthoracic image sequences (2D and 3D volume data, both derived in radiofrequency format, directly after beam forming) were registered in real time from four healthy children over three heart cycles. Three preprocessing methods, based on adaptive filtering, were used to reduce the speckle noise for optimizing the distinction between blood and myocardium, while preserving the sharpness of edges between anatomical structures. The filtering kernel size was linked to the local speckle size and the speckle noise characteristics were considered to define the optimal filter in one of the methods. The filtered 2D images were thresholded automatically as a first step of segmentation of the endocardial wall. The final segmentation step was achieved by applying a deformable contour algorithm. This segmentation of each 2D image of the 3D + time (i.e., 4D) datasets was related to that of the neighboring images in both time and space. By thus incorporating spatial and temporal information of 3D ultrasound image sequences, an automated method using image statistics was developed to perform 3D segmentation of the heart muscle.

3.1 Introduction

The objective of this study was to segment the myocardium in echographic images of children. Because ultrasound is a noninvasive modality for imaging the heart with excellent temporal resolution, it is very suitable for cardiac imaging in children. However, the interpretation of echocardiographic images depends strongly on the interpretation of the expert user. Automatic segmentation can be a helpful tool to diminish this intra-expert variability. It can help to visualize (congenital) abnormalities in cardiac anatomy and to assess cardiac function. At the same time, it can serve as an important preprocessing step in the automatic assessment of functional muscle characteristics by means of strain imaging. Thus, it may substantially support clinical diagnosis of (congenital) heart disease at an early stage.

The availability of real-time 3D ultrasound provides rich information about the 3D deformation cycle and the structure of the heart. However, echographic images are difficult to analyze. This is mainly because of the high level of speckle noise and the reduced echogenicity of structures that are parallel to the propagation direction of ultrasound. Segmentation of cardiac ultrasound is therefore a challenging scientific problem and many approaches for analyzing adult echocardiographic images have been published in recent literature [Angelini et al. 2005; Bosch et al. 2002; Dydenko et al. 2003; Gerard et al. 2002; Lin et al. 2003]. Unfortunately, segmentation of the heart muscle in pediatric ultrasound images faces some additional difficulties. One of them is that the image quality achieved in children may be relatively poor because of the relatively small intercostal spaces in 3D transthoracic short-axis view imaging of the left ventricle. The transmitted ultrasound pulse is then affected by the ribs, which causes both shadowing and clutter appearance in the echocardiographic images. Another difficulty is that papillary muscles fill up a relatively large part of the left ventricle compared with the adult heart. Furthermore, echocardiography in children is geared toward detection of abnormal anatomy as a result of congenital malformations in contrast to adult cardiology, where echography is used in the majority of the cases to determine cardiac output and other properties. Therefore, segmentation methods that strongly rely on *a priori* knowledge of shape and appearance of anatomical structures are less suitable for echocardiographic images of children with congenital heart disease.

Automatic segmentation of echocardiographic images can be either region based or edge based [Noble and Boukerroui 2006; Angelini et al. 2005; Davignon et al. 2005]. Among others, the approaches include region classifiers, deformable model methods and active appearance models (AAMs). Region classifiers use the assumption that an image can be described in terms of homogeneous areas. Bayesian statistics can be used to assess the maximum *a posteriori* probability [Ashton and Parker 1995]. Deformable models [Angelini et al. 2005; Cohen 1991; Gerard et al. 2002; Kass et al. 1987], also referred to as active contours, can be used to segment the heart muscle by deforming a contour or surface under internal and external forces. These models use edge information, e.g., gradient information, as external force, and elasticity and stiffness terms as internal forces. AAMs [Bosch et al. 2002] describe both object shape and image appearance to build a statistical model. The models are trained by a set of manually segmented images. Although AAMs are robust when segmenting standard heart geometries, they are not dedicated to detecting anatomical abnormalities. Deformable model methods do not have this limitation and, therefore, may be more suitable for detecting congenital heart disease and visualizing abnormalities in cardiac anatomy.

The nonisotropic backscatter characteristics of the heart wall and the multiplicative character of speckle noise affect the image quality considerably. Furthermore, the myocardium produces a low echo level at longitudinal incidence of the ultrasound beam, with respect to fiber orientation. This causes the contrast between blood and myocardium to be considerably reduced and the myocardial contours become ill defined. For segmentation purposes, it is important that edge information of various anatomical structures can be extracted from the image. For example, when deformable models are used, gradient information steers the external forces to find edges. Applying such a technique to noisy ultrasound images will meet various difficulties. This quality problem induces the need for preprocessing before any analysis of myocardial images. Preprocessing should start with reducing the basic nonhomogeneous characteristics of echographic images. In general, a Rayleigh probability distribution function (pdf) is assumed to govern speckle statistics of images from parenchymal tissues. This assumption is valid in the special case that the number density of scatterers is high enough to yield 10 or more scatterers per resolution cell, and the spatial distribution of scatterers is homogeneous and isotropic. However, it was shown [Clifford et al. 1993] that the K-pdf [Jakeman and Pussey 1976] gives a better description of echograms obtained from the heart muscle. This pdf is still a case of multiplicative noise, i.e., the variance (as well as standard deviation) is related to the mean level. The K-pdf may be called sub-Rayleigh, implying that the effective number of scatterers is below the previously mentioned limit of 10.

Properties of the preprocessing step should be the reduction of speckle noise (denoising) while preserving, or even enhancing, the edges between different structures, i.e., between regions with different echographic characteristics. Denoising methods are performed locally (sliding kernel methods) and are often described as *nonisotropic* filtering, or as *adaptive filtering*. The adaptive algorithm should use an adequate inhomogeneity or gradient detection strategy to be able to find edges and thus to be able to prevent smoothing of the borders of various anatomical structures. Adaptive filtering might be based on the original B-mode gray level images, but various other gray level encodings have also been tried. Local first-order and second-order statistical parameters that were used are: mean [Bamber and Daft 1986], median [Loupas et al. 1989], signal-to-noise ratio (inverse of the coefficient of variation; Verhoeven et al. [1991]), root-mean-squares [Kotropoulos and Pitas 1992] and mean squares (this paper). For a general assessment of adaptive filtering see Verhoeven and Thijssen [1993]. Nonadaptive filtering may be used by using gray level transforms that preserve, or enhance, contour information. An example of this method is the local entropy encoding of the windowed gray levels [Kapur et al. 1985; Mao et al. 2000; Zimmer et al. 1996]. This approach was also investigated in the present study.

This paper purports segmentation of the heart muscle by using speckle reduction, based on image statistics, automatic thresholding and deformable models.

The preprocessing should result in a segmentation of the heart muscle for the purpose of tissue strain imaging, image texture analysis or ultrasound spectroscopy. The quality of the speckle reduction was tested elaborately. The 3D endocardial surface was segmented by using the 3D + t (time) information available.

3.2 Materials and Methods

Echocardiographic images of four healthy children were obtained. These four healthy children (8, 10, 12 and 15 years old) were referred to the Pediatric Cardiology Department for the exclusion of heart disease (cardiomyopathy) and they appeared to be cardiologically normal, as assessed by an experienced pediatric cardiologist. The parents gave their informed consent for using the echographic data for this research project. Image sequences of the left ventricle were taken using transthoracic short- and long-axis views. Two-dimensional and 3D radiofrequency (RF) data were acquired using a Philips SONOS 7500 live 3D ultrasound system (Bothell, WA, USA), equipped with an RF-interface. An X4 matrix array transducer (2-4 MHz) for adult was used to perform 3D imaging. In addition, 2D images were obtained using an S8 phased array transducer (3-8 MHz). RF-data were sampled at 19.5 MHz and 39 MHz for the X4 and S8 transducer, respectively, and were transmitted to a workstation using a USB 2.0 interface. The 2D datasets (S8 transducer) only served as additional testing material for the preprocessing methods; the actual segmentation was performed on the 3D datasets (X4 transducer). MATLAB (The Mathworks, Inc., Natick, MA, USA) scripts were used to perform all calculations.

3.2.1 Segmentation Method

The algorithm for segmentation of the myocardium in 3D + t images consisted of four steps that are illustrated by the flow chart in 3.1. First, spatial filtering was used as a preprocessing step to reduce the influence of speckle noise, while preserving the sharpness of the edges and at the same time increasing the contrast between blood and myocardium. Next, automatic thresholding served as a first segmentation step to separate blood from the myocardium. Then homomorphic filtering was applied to improve the result by removing spurious echoes. Finally, a deformable contour algorithm was applied to the thresholded images to extract the endocardial borders from the 3D dataset. The assumption of spatio-temporal continuity of the heart movement imposes limitations on the variations between endocardial contours in consecutive planes both in time and space. This continuity assumption was used to optimize the deformable contour algorithm.

3.2.2 Preprocessing of echographic images

A general characteristic of echographic images is the nonisotropic texture as a result of the difference in axial and lateral spatial resolutions and speckle sizes.

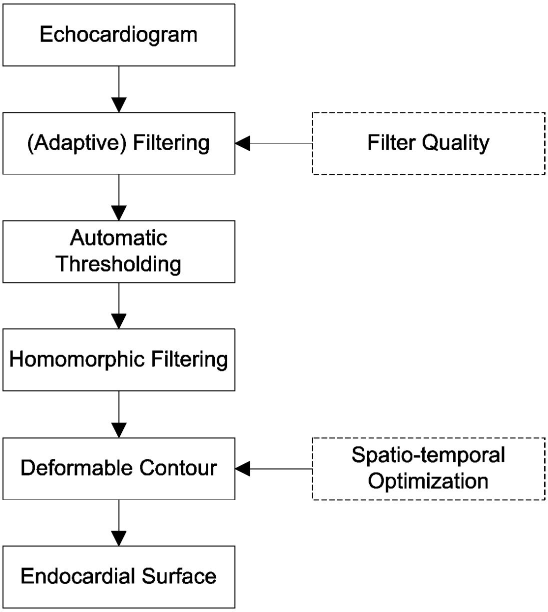

Figure 3.1: Flow chart of software algorithms used in this paper. Adaptive filtering stands for preprocessing of the images by speckle noise suppression. Thresholding and homomorphic filtering create the bimodal image for the deformable contour algorithm to find the optimal endocardial contour.

In addition, speckle dimensions are depth dependent because of beam diffraction and focusing, as well as attenuation. It was found that lateral speckle size increases proportionally to depth [Oosterveld et al. 1985; Thijssen and Oosterveld 1988]. The axial speckle size appeared to be practically constant over depth. In addition, image anisotropy can be induced by nonisotropic characteristics of the scattering by tissues, like the myocardium. Finally, because of attenuation in tissue, the mean echo level decreases with penetration depth. To make the lateral speckle size depth independent, the 2D sector image of the phased array scanning device was processed along the scan lines, i.e., the image was processed in a rectangular format [Oosterveld et al. 1985; Valckx et al. 2000] before sector imaging. Consequently, the data could be filtered using a sliding kernel with fixed dimensions for all depths.

The choice of the kernel size to be used in the local preprocessing of the images is not trivial because of the already mentioned different axial and lateral speckle sizes. Furthermore, because the speckle can be considered as the smallest, uncorrelated "grain of information" [Smith et al. 1983], then according to the Central Limit Theorem of Statistics, a minimum number of 10 speckles would be necessary to achieve a Gaussian pdf for the mean value of any chosen texture parameter for the kernel. This pdf is being considered as the ideal condition for further processing of the images. So the trade-off between preservation of spatial resolution and wanted statistical properties demands for a preliminary study to find the most suitable kernel size, expressed in the number of pixels in axial and lateral directions. The speckle size was estimated by computing the full-width-at-half-maximum of the 2D autocovariance function [Papoulis 1976; Wagner et al. 1983] of images obtained in a homogeneous phantom. The number of speckles within the kernel area was taken to be 10 following the Central Limit Theorem of Statistics. Adaptive filtering methods and the local entropy calculation were used to preprocess the images. Before the RF-data were filtered, they were amplitude demodulated by using the Hilbert transform. Two-dimensional filtering was applied to the axial-lateral planes of the datasets. Adaptive filters sense the properties of the environment they operate in and adjust their filter parameters accordingly. This paper discusses adaptive mean (AM) filtering and adaptive mean squares (AMS) filtering. The adaptivity of these filters lies in the fact that the degree of smoothing is determined by the homogeneity of the region the filtering is operating on. This results in the preservation of the sharpness of the edges of various structures, because regions containing an edge are not at all homogeneous and therefore will be less smoothed than homogeneous regions. Furthermore, these filters might optimize the discrimination between blood, myocardium and pericardium. We used the algorithm of Bamber and Daft [1986], see also Verhoeven and Thijssen [1993] for an assessment study.

The algorithm was based on the following formulas:

$$\tilde{g} = \mu + k(g - \mu) \tag{3.1}$$

$$k = a * p - p_s \tag{3.2}$$

$$p = \frac{\sigma^2}{\mu} \tag{3.3}$$

where g = original gray level, k = degree of filtering, μ and σ^2 = mean and variance of the gray levels of the kernel, respectively, $p = \sigma^2/\mu$ = degree of inhomogeneity of a region and a is an aggressiveness factor, which is set to one in this application (no changes in the range of the gray values as a result of the filtering procedure).

The parameter p_s is the reference speckle feature, which is the mean value of p in a region of the image where a high degree of smoothing is required. In practice, the value for p_s is determined once for a transducer by selecting a region in the image consisting of fully developed speckle [Wagner et al. 1983]. Regions for which p is smaller than p_s lead to a negative value for k. Because this is an undesirable effect, negative k values were set to 0. The AM filter works straight on the envelope data, whereas the AMS filter squares the data first before adaptive filtering is performed.

Apart from these adaptive methods, a 2D nonadaptive method was used as a preprocessing step. The latter method is based on another measure for the homogeneity, or amount of information, in a certain region, which is the local entropy. The local gray-level entropy is defined as follows:

$$H(G) = -\sum_{g \in G} P(g) \ln P(g) \qquad G = \{g_1, \ldots, g_n\} \tag{3.4}$$

where $P(g)$ is the probability that an arbitrary pixel has gray level g. This filtering may be applied without using the adaptive strategy because local entropy is lower for a homogeneous region than for a heterogeneous region. Therefore, the contours are to some extent preserved by this characteristic of entropy. Again the sliding kernel technique was used to compute local entropy values for all pixels.

3.2.3 Filter Quality

The goal of applying these filters was to nonlinearly adjust the echographic gray-level information in such a way that, after filtering, the gray levels of blood and tissue are more separated. One way to measure the quality of a filter is by comparing overlap percentages of the histograms of blood and myocardial regions. These regions were interactively segmented in the 2D axial-lateral image plane by an experienced pediatric cardiologist. The histograms were normalized and then analyzed in the log(gray-level) domain. The overlap percentages give an indication of the increase in distinction between blood and myocardium before and after filtering. For a set of images of four healthy subjects, blood and myocardial regions were segmented manually by an expert. Depending on the clinical problem, clinicians are interested in the size of the myocardium with papillary muscles (i.e., finding the cavity area of the left ventricle), or they are interested in the mass of the heart muscle exclusive of the papillary muscles. In the present study, the papillary muscles were fused with the muscle region. The quality of all filter results, obtained from 2D as well as from 3D datasets, was analyzed in the 2D axial-lateral plane. A Wilcoxon rank-sum test was performed over all datasets to test whether the filters significantly diminished the overlap percentages of blood and myocardium. This test was also used to compare overlap percentages produced by the different filters.

Receiver operating characteristic (ROC) curves were determined for the manually segmented blood regions to summarize the effect of the different filtering methods. The reason to primarily compare blood with other tissue (myocardium, papillary muscles and pericardium) is that this threshold is the basis of the automatic thresholding and segmentation procedure to find the endocardial contour. ROC curves depict the relation between sensitivity and specificity. In this case, sensitivity is defined as the probability that a pixel is classified as blood for a pixel that truly is blood. Specificity is defined as the probability that a pixel is classified as nonblood for a pixel that truly is nonblood.

The area under the ROC curve (AUC) is a well-known summary measure of accuracy. The AUC is preferable to other measures, such as the Youden's Index [Youden 1950], because the choice of the decision threshold does not affect this accuracy measure, and neither does the prevalence of the number of positives [Obuchowski 2005]. The AUC varies from 0.5 to 1, for chance and perfect discrimination, respectively. The ROC analysis software package [Metz 1998] was used to determine the AUC and the standard deviation of the AUC. These parameters were used to test whether the AUC of the filtered data were significantly larger than the AUC of the unprocessed data by computing p-values (z-test) for the difference in AUCs for each separate dataset. Also a t-test was performed to compare the mean AUCs over all datasets. The same tests were used to compare differences in AUCs in between filters.

3.2.4 Automatic thresholding

After the outlined speckle reduction approach, the next step was region finding. Various algorithms may be used for this purpose: K-means clustering (local; MacQueen [1967]), histogram thresholding (global; Otsu [1979]), either based on prior knowledge of histograms corresponding with various regions or on optimization of the between-class variance, and maximum a posteriori probability assessment (Bayesian) methods [Ashton and Parker 1995].

The Otsu method [Otsu 1979] of automatic histogram thresholding was applied to the filtered data to find automatically the optimal separation between blood and myocardium. This method was used recursively to find the optimal threshold. Because of the large spread of the data in the case of the AM and AMS filters, thresholding was performed on the log of the data. The local entropy-filtered data were thresholded without the logarithmic compression because the histograms of the linearly encoded images were rather symmetric already.

The estimated, optimal threshold was applied to generate a binary image in which blood was separated from the remainder of the tissue. This image was then used as the input for the deformable contour algorithm. To relate the threshold obtained from the automatic thresholding algorithm to the optimal threshold in terms of specificity and sensitivity, the threshold was compared with the point on the ROC curve where sensitivity equals specificity.

3.2.5 Deformable contour

A deformable contour algorithm, including an inflating force, was applied to each separate elevational plane of the 3D volume scan to find the endocardial contour. A deformable contour is represented parametrically as:

$$v(s) = \left(x(s), y(s)\right)^T \qquad \in [0,1] \tag{3.5}$$

Deformation of the contour is performed by minimizing the energy functional E_{total}:

$$E_{total} = E_{int}(v(s)) + E_{ext}(v(s)) \tag{3.6}$$

where

$$E_{int} = \int_0^1 \alpha(s)\left|\frac{\partial v}{\partial s}\right|^2 + \beta(s)\left|\frac{\partial^2 v}{\partial s^2}\right| ds \tag{3.7}$$

$$E_{ext} = \int_0^1 P(v(s))ds \tag{3.8}$$

E_{int} is the internal energy, with weighting parameters α and β that control the tension and rigidity, respectively, of the deformable contour. The external energy functional E_{ext} attracts the deformable contour to features in the image $I(x,y)$, for example by choosing $P(x,y) = -\left\|\nabla I(x,y)\right\|^2$.

Because the algorithm expects the resolution in axial and lateral direction to be identical, the data first needed to be resampled. Next, an opening operation [Serra 1982] with a square structuring element of 5 x 5 pixels was applied to remove spurious "tissue" areas within the blood region of the binary image. On the basis of the continuous movement of the heart, continuity of the endocardial contours was assumed in both spatial and temporal dimensions. Transforming this assumption to boundary conditions of the deformable contour algorithm, the contour in the current plane $C(r,t)$ was optimized by using contours of adjacent planes in time and place as a limiting condition. In terms of spatial continuity $C(r+1,t)$ was used as a limiting condition. Temporal continuity was imposed by using $C(r,t+1)$to limit $C(r,t)$. The algorithm was initialized by finding the endocardial contour of the foremost plane in the systolic phase of the heart beat, without any optimization in terms of continuity. As a final step, for each frame, the endocardial contours obtained by the optimized deformable contour algorithm were combined to form the endocardial surface.

3.3 Results

The quality of the three different filters was examined for 16 datasets of four healthy subjects. Figures 3.2 and 3.3 show representative examples of the effect of the filters on a single image of a 3D dataset of the X4 transducer. It can be seen from Fig. 3.2 that all three filtering techniques resulted in a reduction of speckle noise. The sharpness of the edges was preserved well by both adaptive methods. Although the sharpness of the edges was also preserved by the entropy method, the position of the edges slightly changed compared with the unprocessed and adaptive filtered data. Inhomogeneous regions, such as the pericardium, were almost unaffected by the adaptive filtering procedures, whereas the entropy method also smoothed these regions. When looking at the effect of filtering on the histograms of the data (Fig. 3.3), it can be seen that all three filters produced multimodal histograms.

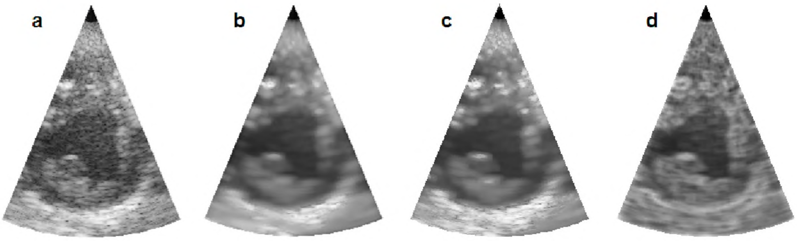

Figure 3.2: Example of the three filtering methods for a single plane of a 3-D dataset acquired with an X4 transducer. From left to right: (a) unprocessed data, (b) AM filter, (c) AMS filter and (d) local entropy.

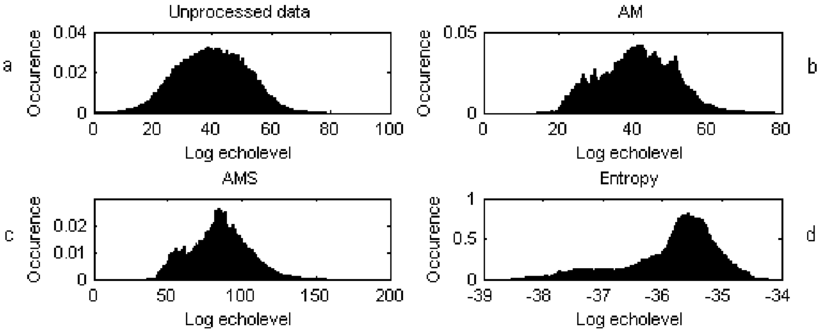

Figure 3.3: (a) Histogram of the unprocessed dataset, (b) dataset after AM filtering, (c) after AMS filtering and (d) entropy. Compare with Fig. 3.2.

To examine the effect of the proposed filters quantitatively, overlap percentages of the histograms of the manually segmented blood pool and the myocardial region before and after filtering were computed for all 16 datasets. An example of manually drawn contours of the blood pool and myocardial region for one dataset, together with the histograms of these regions before and after AMS filtering, is depicted in Fig. 3.4. For this particular dataset, the overlap percentage of blood and myocardial regions decreased from 35.4% for the unprocessed dataset to 19.5% after AMS filtering. All filters showed a decrease in overlap percentage for all individual cases. The mean and standard deviation of overlap percentages for all datasets are listed in Table 3.1. This table shows that standard deviations are large compared with the mean value, indicating that there is a large variability in overlap percentages over all datasets. P-values for the Wilcoxon rank-sum test on the difference in overlap before and after filtering revealed a significant decrease in overlap of histograms of blood and myocardium ($p < 0.01$; Table 3.2).

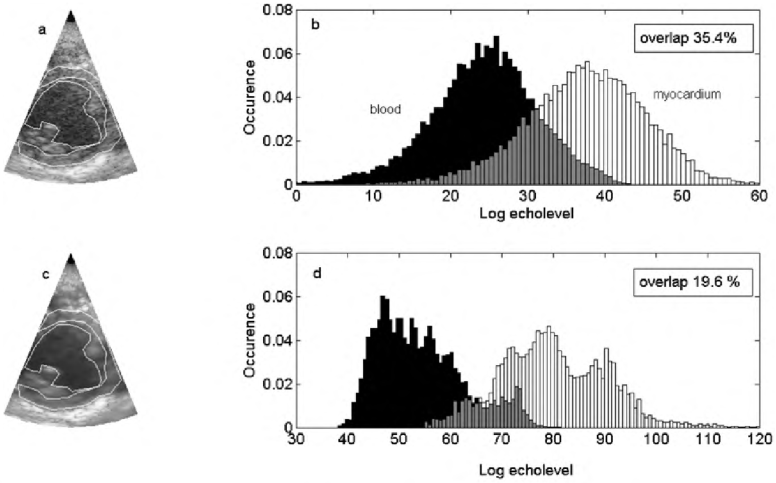

Figure 3.4: Left side: (a) manually segmented contours of blood and myocardium regions of unprocessed data and (c) data after AMS filtering for a single plane of a 3-D dataset acquired with an X4 transducer. Right side: (b) normalized histograms of blood and myocardium before and (d) after AMS filtering.

Table 3.1: Overview of mean and standard deviation of histogram overlap percentages for unprocessed data and different filtering methods.

Overlap gray level histograms blood/myocardium

Filter method	Mean overlap % (n = 16)	Standard deviation of overlap %
Unprocessed data	46.8	8.1
AM filter	30.1	11.9
AMS filter	29.9	11.4
Entropy	34.1	9.9

The distinctiveness of blood and myocardium has thus improved significantly. Although from Table 3.1 it seems that, on average, the adaptive filters gave slightly better results than local entropy for the analyzed datasets, it turned out that the difference in overlap percentage of the various filtering methods is not significant ($p >> 0.05$; Table 3.2).

To further investigate the effect of the filters on discrimination of blood vs. other tissue, the AUC was computed for the filtering methods for all cases. Average value and standard deviation for the AUCs are listed in Table 3.3, where a higher AUC indicates a higher accuracy. Figure 3.5 shows the ROC curves of

Table 3.2: P-values for histogram overlap percentages using Wilcoxon rank sum test.

Filter method	Data	AM	AMS	Entropy
Data		< 0.001	< 0.001	0.0011
AM			0.84	0.40
AMS				0.32
Entropy				

the unprocessed and AMS-filtered data for one dataset. The increase of the area under the ROC curve can be noted when comparing the AMS-filtered data with the unprocessed data. Both statistical tests on the difference in AUC revealed a significant increase in AUC when comparing adaptive filtering (AM and AMS) to the unprocessed data (Tables 3.4 and 3.5). The AUC of the local entropy is significantly larger than the AUC of the unprocessed data in 12 of the 16 cases (Table 3.4, z-test). Nevertheless, using the t-test, the AUC of the local entropy turned out to be significantly larger than the AUC of the unprocessed data (Table 3.5). However, mutual comparison of the three filters revealed no significant difference in AUCs (Tables 3.4 and 3.5). Therefore, the exact choice of the filter seems to be less important than the fact that some sort of dedicated filtering is applied. The AMS filter, in combination with automatic thresholding, was chosen as a preprocessing step for the deformable contour algorithm because this filter performed best on both overlap percentage and ROC curve tests. The threshold obtained from the automatic thresholding algorithm was compared with the point on the ROC curve where sensitivity equals specificity. For both AM and AMS filtering, these two thresholds were similar, indicating that the threshold obtained by the automatic thresholding is a reasonable compromise in terms of sensitivity and specificity.

The deformable contour algorithm was applied to a 3D dataset acquired over a full heart cycle to find the endocardial surface. Visually plausible contours were obtained for all elevational planes. Figure 3.6 shows a representative example of one particular elevational plane of the heart cycle. Using 4D information by imposing spatial and temporal continuity for contours of the separate planes, better

Table 3.3: Overview of mean and standard deviation of AUC of ROCs for unprocessed data and different filtering methods.

ROC analysis

Filter method	Mean AUC % (n = 16)	Standard deviation of the mean AUC %
Unprocessed data	86.2	4.2
AM filter	91.4	3.5
AMS filter	91.7	3.5
Entropy	90.2	4.5

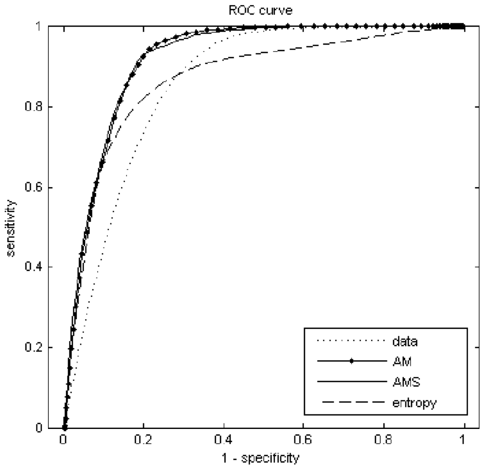

Figure 3.5: Example of ROC curves for one dataset (X4 transducer). The AUC increased from 0.86 (before processing) to 0.92 for AM and AMS, and to 0.87 for entropy.

Table 3.4: P-values for AUC of ROCs, z-test for each dataset.

Filter method	Data	AM	AMS	Entropy
Data		< 0.001 (n = 16)	< 0.01 (n= 16)	< 0.05 (n = 12) > 0.05 (n = 4)
AM			> 0.05 (n = 16)	< 0.05 (n = 5) > 0.05 (n = 11)
AMS				< 0.05 (n = 7) > 0.05 (n = 9)
Entropy				

Table 3.5: P-values for AUC of ROCs using 2-tailed t-test, DF = 15.

Filter method	Data	AM	AMS	Entropy
Data		< 0.001	< 0.001	< 0.001
AM			0.059	0.099
AMS				0.027
Entropy				

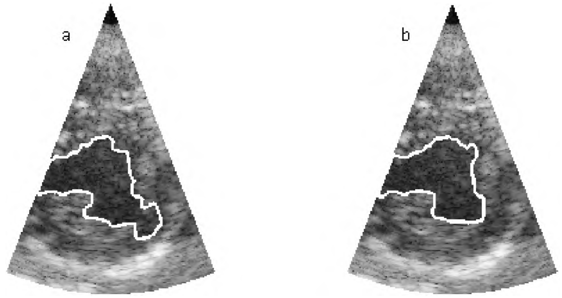

Figure 3.6: Deformable contour (a) without and (b) with spatio-temporal optimization for a single plane of a 3-D dataset acquired with an X4 transducer.

segmentation of the ventricle was obtained than when using information of each plane separately. A comparison of manually segmented contours with automatically detected contours throughout the heart cycle is illustrated in Fig. 3.7. In Fig. 3.8 all endocardial contours were combined for the subsequent elevational echo images to form a 3D endocardial surface. The endocardial surface shows coherency between the contours of consecutive planes. Because one may also have to deal with anatomical heart abnormalities in children, no smoothing of the endocardial surface was performed because this might have blurred anatomical details.

3.4 Discussion

In this paper, a 3D segmentation method of the endocardial surface is described. The principal findings of this study are that adaptive filtering improves the distinction between myocardium and blood, and that the combination of adaptive filtering using image statistics and deformable contours has the potential to improve the segmentation of the endocardial surface.

The degree of adaptive filtering is determined by the parameter $p = \sigma^2/\mu$. This parameter was chosen by Bamber and Daft [1986] because it was found to be constant for video data digitized by a frame grabber in their equipment. These data were therefore nonlinearly encoded by the compression amplifier before analog-to-digital (AD) conversion in the equipment. It should be kept in mind, however, that the present data are based on demodulated RF-data, i.e., linearly encoded gray level data, Theoretically, assuming a Rayleigh-pdf for fully developed speckle regions, σ/μ is a constant and for these regions the defined parameter p would reduce to σ. However, the pdf of the myocardium and blood is sub-Rayleigh and therefore σ/μ is not exactly constant. Using $p = \sigma/\mu$ to determine the degree of filtering gave similar results for the described quality of filter measures as when

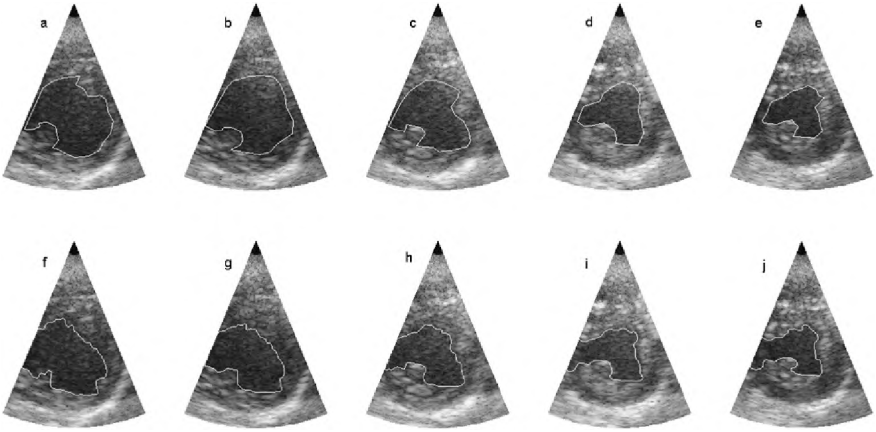

Figure 3.7: (a-e) Manually segmented endocardial contours vs. (f-j) automatically detected contours after spatio-temporal optimization in datasets acquired with an X4 transducer, starting from (a and f) end-diastolic phase to (e and j) systolic phase.

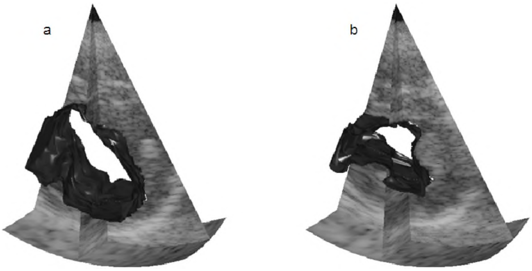

Figure 3.8: Endocardial surface after spatio-temporal optimization in datasets acquired with an X4 transducer: (a) end-diastolic phase and (b) systolic phase.

taking $p = \sigma^2/\mu$. The texture in nonhomogeneous parts is preserved better for $p = \sigma^2/\mu$, whereas, the contrasts are better when $p = \sigma/\mu$ is used. Figure 3.9 illustrates these effects. In the present study, it appeared that the Gamma pdf optimally fitted to the histograms obtained from heart muscle (Chapter 2). For this pdf, $\sigma^2/\mu = \theta$, where θ is a constant called the scale parameter of the Gamma pdf.

Improvements in overlap percentages of blood and myocardial region before and after filtering were highly significant. However, overlap percentages for the different acquisitions showed large variability. Besides interpatient variability, the

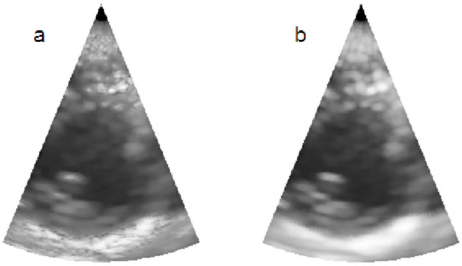

Figure 3.9: Comparison of homogeneity parameter: (a) AMS filter using $p = \sigma^2/\mu$ vs. (b) AMS filter using $\mathrm{p} = \sigma/\mu$

use of two transducers (S8 and X4) that differ in contrast and resolution might have contributed to this variability. Because regions are compared separately before and after filtering for each dataset, quality differences of the original images do not influence the observations and final conclusions.

The method of 3D segmentation is fully automated: no user interaction is required, except for the choice of the initial plane the deformable contour algorithm is started from. In clinical practice, this initial starting plane might be automatically chosen if 3D volumes are acquired in a standard way. The advantage of real-time 3D ultrasound is that all image planes can be acquired with one 3D acquisition and also be followed over time. Selection of the proper frame in time can be done in relation to the electrocardiogram (ECG). The ECG can also be used to improve the segmentation algorithm by integrating information related to the phase within the cardiac cycle. Although the method was designed to perform 3D segmentation, it still has to be optimized by using 3D deformable surfaces, rather than 2D contours, to incorporate the use of temporal and spatial information more profitably. It also has to be investigated whether proper 3D adaptive filtering might further improve the results.

The limited quality of the pediatric cardiac images may cause essential problems in the segmentation process as long as prior knowledge about the anatomy (shape) is not incorporated. Figure 3.7 shows that for the manually drawn contour, knowledge about the shape of the left ventricle was indeed used. This indicates that anatomical knowledge is necessary to improve the segmentation of the myocardium, although the influence of this knowledge should be handled carefully to prevent overlooking abnormalities in the anatomy. New transducers have appeared on the market, which are specifically designed for pediatric diagnosis and it may be expected that a better image quality will be available soon. This could eliminate some of the problems we are currently encountering in pediatric echocardiology.

Adaptive filtering may also improve the distinction between myocardium and pericardium and, therefore, might also be used as a preprocessing step for segmenting the pericardium. Segmentation of the pericardium will be necessary to obtain a complete segmentation of heart muscle.

Acknowledgements

This work was supported by Philips Medical Systems and the Dutch Technology Foundation (STW), project NKG 06466.

4

IN VIVO VALIDATION OF CARDIAC OUTPUT ASSESSMENT IN NON-STANDARD 3D ECHOCARDIOGRAPHIC IMAGES

Based on: M. M. Nillesen, R. G. Lopata, W. P. de Boode, I. H. Gerrits, H. J. Huisman, J. M. Thijssen, L. Kapusta, and C. L. de Korte. In Vivo Validation of Cardiac Output Assessment in Non-Standard 3D Echocardiographic Images. *Phys Med Biol* 54(7):1951-1962, 2009.

4

Abstract

Automatic segmentation of the endocardial surface in three-dimensional (3D) echocardiographic images is an important tool to assess left ventricular (LV) geometry and cardiac output (CO). The presence of speckle noise, as well as the nonisotropic characteristics of the myocardium impose strong demands on the segmentation algorithm. In the analysis of normal heart geometries of standardized (apical) views, it is advantageous to incorporate *a priori* knowledge about the shape and appearance of the heart. In contrast, when analyzing abnormal heart geometries, for example in children with congenital malformations, this *a priori* knowledge about the shape and anatomy of the LV might induce erroneous segmentation results.

This study describes a fully automated segmentation method for the analysis of non-standard echocardiographic images, without making strong assumptions on the shape and appearance of the heart. The method was validated *in vivo* in a piglet model.

Real-time 3D echocardiographic image sequences of five piglets were acquired in radiofrequency (RF) format. These ECG-gated full volume images were acquired intra-operatively in a non-standard view. Cardiac blood flow was measured simultaneously by an ultrasound transit time flow probe positioned around the common pulmonary artery. Three-dimensional adaptive filtering using the characteristics of speckle was performed on the demodulated RF-data to reduce the influence of speckle noise and to optimize the distinction between blood and myocardium. A gradient-based 3D deformable simplex mesh was then used to segment the endocardial surface. A gradient and a speed force were included as external forces of the model. To balance data fitting and mesh regularity, one fixed set of weighting parameters of internal, gradient and speed forces was used for all

datasets.

End-diastolic and end-systolic volumes were computed from the segmented endocardial surface. The cardiac output derived from this automatic segmentation was validated quantitatively by comparing it with the CO values measured from the volume flow in the pulmonary artery. Relative bias varied between 0 and -17%, where the nominal accuracy of the flow meter is in the order of 10%. Assuming the CO measurements from the flow probe as a gold standard, excellent correlation ($r = 0.99$) was observed with the CO estimates obtained from image segmentation.

4.1 Introduction

Real-time three-dimensional ultrasound is a non-invasive imaging modality that is capable of visualizing the complex 3D structure of the heart with high temporal resolution. Segmentation of the left ventricle might be a helpful tool for clinical analysis of 3D echocardiographic images. This technique can be used for automated assessment of congenital deformities and may serve as an important preprocessing step for cardiac tissue characterization. It may also be used for functional assessment, e.g., volumetric studies. Estimation of ventricular volumes and related, clinically relevant parameters such as cardiac output (CO) and ejection fraction (EF) has been boosted by the availability of real-time three-dimensional echocardiographic imaging techniques. In comparison to two-dimensional (2D) echocardiography, 3D echocardiography obviates the necessity for 2D geometrical assumptions. These geometrical assumptions comprise a simplified shape of the ventricle and may lead to inaccurate ventricular function estimation in diseased hearts and in foreshortened 2D images of the ventricle. 3D echocardiographic imaging enables a more accurate assessment of ventricular volume [Gopal et al. 1995].

Since manual segmentation of the left ventricle in 3D ultrasound image sequences is time-consuming and is subject to inter-expert variability, (semi-) automatic segmentation techniques are required. Due to the influence of speckle noise and the reduced echogenicity of the heart wall in regions where the muscle fibers are approximately parallel to the propagation direction of the ultrasound beam, automated segmentation in echocardiographic images is challenging.

Several approaches for semi-automated or automated segmentation of echographic data have been reported in recent literature (see Noble and Boukerroui [2006] for an overview). Among others, the approaches include (statistically based) region classifiers, deformable models and Active Appearance Models (AAMs). Almost all methods use the envelope signal, only few methods are based on the radio frequency (RF) signal [Dydenko et al. 2003; Yan et al. 2007; Gerrits et al. 2007].

Region classifiers assume that the image can be described in terms of homogeneous areas. The maximum *a posteriori* probability can be assessed by using

Bayesian statistics. Knowledge about speckle statistics can be incorporated into the method [Ashton and Parker 1995; Dias and Leitao 1996].

Deformable models are widely proposed for segmentation of the left ventricular cavity. In these models, a contour or surface is deformed by the influence of internal and external forces. The internal force contains geometric constraints, such as the smoothness of the surface. The external force is determined by features in the image such as gradients, texture and homogeneity. Gerard et al. [2002] and Böttger et al. [2007] successfully applied these models to echocardiographic data using edge-based features. Montagnat et al. [2003] proposed a deformable model using both edge-based and region-based information. A deformable model can also be implemented using a level set method, where the surface is represented by a higher-dimensional function. Sarti et al. [2005] incorporated statistical characteristics of ultrasound into a level set method by using a maximum likelihood approach. A combination of wavelets and level sets was proposed by Angelini et al. [2005]. Lin et al. [2003] combined region and edge based information in a level set based algorithm. A level set algorithm applied to real-time 3D echocardiographic images was presented by Corsi et al. [2002].

Because of the low contrast between the ventricular cavity and the myocardial wall in some regions, *a priori* knowledge about the average shape, appearance and motion is often incorporated in the segmentation method. So-called Active Appearance Models (AAMs) [Mitchell et al. 2002] use both object shape and appearance of cardiac structures to build a statistical model. Bosch et al. [2002] included knowledge about left ventricular motion using Active Appearance Motion Models (AAMMs). 4D motion patterns of the heart were also incorporated in a segmentation method that was primarily based on deformable models [Gerard et al. 2002]. van Stralen et al. [2005] used the shape and appearance of the heart muscle in a dynamic programming approach.

Incorporating knowledge about the left ventricle is advantageous and successful when analyzing echocardiographic images of standard heart geometries in standardized (apical) views. However, for the analysis of echocardiographic images in non-standard views, or, for example in children with congenital malformations of the heart, segmentation methods that strongly rely on *a priori* knowledge of shape or appearance may lead to segmentation errors. To obtain quantitative information about left ventricular function and composition of the heart muscle in these cases, a method that functions independently of assumptions about geometry and viewing angle should be used.

In this study, a combination of adaptive speckle denoising filtering and gradient-based deformable simplex meshes was used for the segmentation of the endocardial surface in non-standard heart geometries and views. Since the deformable model uses gradient information to steer the external forces to find edges of anatomical structures, it was essential to suppress the speckle noise in the ultrasound images. For this reason, 3D adaptive filtering was used to improve the distinction between blood and myocardium and to reduce the speckle noise. Except for constraints on the smoothness of the surface, no assumptions were made about the shape or orientation of the left ventricle. The independence of viewing angle enables segmentation of a broad range of cardiac ultrasound images in particular in children with abnormal cardiac anatomy.

The purpose of this study was to validate the developed cardiac output (CO) measurement technique by fully automated segmentation of the endocardial wall of the left ventricle in non-standard echocardiographic images. The validation was performed in a piglet model (*in vivo*) by computing the CO from segmented volumes in non-standard views and comparing it to the CO simultaneously obtained from the volume flow through the main pulmonary artery of the piglets.

4.2 Materials and Methods

4.2.1 Animal Model

Intra-operative echocardiographic image sequences of the left ventricle were obtained in five piglets. The study was approved by the Ethical Committee on Animal Research of the Radboud University Nijmegen (RU-DEC #2007-144).

The study was performed in 5 random-bred newborn piglets (3.5-6.9 kg) in accordance with the Dutch national legislation concerning the guidelines for the care and use of laboratory animals. The piglets were not fed in the 12 hours prior to the experiment. Ketamine (10 mg/kg), atropine (0.03 mg/kg) and midazolam (0.5 mg/kg) were administered intramuscularly as premedication. After intravenous injection of propofol (2-3 mg/kg), the piglets were orotracheally intubated with a cuffed endotracheal tube (Kruse, Marslev, Denmark). The animals were artificially ventilated in a pressure control mode. Anesthesia was maintained with inhalation of isoflurane (0.5-2.0 vol%), and the intravenous administration of fentanyl (5-20 μg/kg/hr) and midazolam (0.5 mg/kg/hr). During the thoracotomy, muscle paralysis was achieved with pancuronium (0.1 mg/kg intravenous). The settings of the ventilator were adjusted in order to maintain normoxaemia (Arterial oxygen saturation measured by pulse oximetry (SpO_2) 90-95%) and normocapnia (arterial CO_2 pressure ($paCO_2$) 30-45 mmHg; end-tidal CO_2 pressure ($etCO_2$) 30-45 mmHg). A servo-controlled heating mattress was used to maintain a rectal temperature between 38 and 39°C. Intravascular catheters were surgically inserted.

A left-sided thoracotomy was performed and, after preparation, an adequately sized perivascular dual beam ultrasonic flow probe (PAX series, Transonic® Systems Inc., Ithaca, USA) was placed around the main pulmonary artery. The signal from the flow probe was analyzed by a flow meter (T206, Transonic® Systems Inc., Ithaca, USA). The signal strength of the pulmonary flow probe was checked regularly. In case of a decreased signal strength additional coupling gel was applied. Pulmonary blood flow values, pulsatile as well as averaged, were stored using biomedical data acquisition software (Poly, Inspektor Research Systems BV, Amsterdam, The Netherlands) with a sampling rate of 200 Hz. The heart was exposed and the ultrasound imaging transducer was directly applied to the heart. Coupling gel was used to obtain better image quality. Mechanical ventilation was paused shortly during recording of the echocardiographic data to prevent breathing artefacts. The flow probe was switched off shortly during echographic acquisition to avoid interference. It was verified that flow values just before and after echographic acquisition were equal.

This study was the last part of a multidisciplinary cardiac output study in a piglet model. At the end of the experiment the piglet was sacrificed. The flow probe was checked for zero value directly post mortem.

4.2.2 Echocardiographic data

ECG-gated full volume image sequences were obtained in a non-standard view, i.e., different from the standard long and short axis views in transthoracic echocardiographic examinations. These RF-data were acquired directly after receive beamforming using a Philips SONOS 7500 live 3D ultrasound system (Bothell, WA, USA), equipped with an RF-interface and an X4 matrix array transducer (2-4 MHz). The RF-data were sampled at 19.5 MHz and transferred to a workstation using a USB 2.0 interface. The RF-data were band pass filtered (FIR least squares filter $[2-3.6\text{ MHz}]$) and amplitude demodulated using the Hilbert transform. Matlab software (The MathWorks Inc., Natick, MA, USA) was used to perform the RF-filtering, Hilbert transform and adaptive filtering. The simplex mesh approach was implemented using ITK (v. 2.8) and visualized using VTK (v. 5.0.0).

4.2.3 Adaptive Filtering

3D Adaptive Mean Squares Filtering (AMS) of the amplitude demodulated data was applied in the spatial domain. The AMS filter incorporates knowledge about speckle statistics of blood and myocardium in an adaptive manner. The homogeneity of the region the filter is operating on is used to automatically steer the degree of filtering. The inhomogeneity of the tissue region is represented by $s^2/\bar{x}$, the variance of the echo amplitude level divided by the mean echo amplitude level. This parameter corresponds to the scale parameter of the Gamma distribution, a distribution that optimally fits the image statistics of blood and myocardium (Chapter 2). It has been shown in previous work (Chapter 3) that the AMS filter reduces the influence of speckle noise, while at the same time it increases the contrast between blood and myocardium and preserves the sharpness of edges. Speckle characteristics are depth dependent due to beam diffraction and focusing, as well as due to tissue attenuation. The filter kernel size was related to image speckle size to yield statistically robust data. By processing the data along the

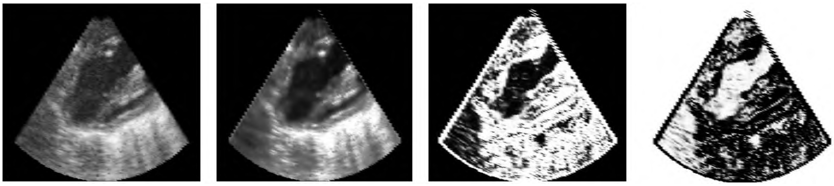

Figure 4.1: Computation of forces for a single axial-lateral plane from a full volume dataset of a piglet. From *left* to *right*: Original data, data after AMS filtering, gradient magnitude image after sigmoidal intensity mapping and speed image after sigmoidal intensity mapping.

scan lines, the lateral speckle size is homogenized [Valckx et al. 2000] and the filter kernel size could thus be set at a fixed value for all depths.The rectangular filter kernel used in this study contained 5 x 2 x 2 (axial x lateral x elevational) speckles. Figure 4.1 shows a single axial-lateral plane from a full volume dataset of a piglet heart (demodulated RF-data) before and after adaptive filtering. Data were visualized in scan-converted format, in order to obtain realistic anatomical views. Adaptive filtering was shown to improve segmentation significantly using gradient-based deformable models (Chapter 3). These models use gradient information to find edges of anatomical structures.

4.2.4 Deformable Simplex Mesh

Deformable simplex meshes were introduced by Delingette [1999] and are well defined, i.e., local geometry of the surface can be controlled well and computation of geometric parameters such as mean curvature is computationally efficient. A simplex mesh consists of a set of vertices that form a discrete non-parametric representation of a surface in $\mathbb{R}^3$. Each vertex of the mesh $p_i = (x_i, y_i, z_i)$ is displaced in an iterative manner according to the discrete approximation of the Newtonian law of motion:

$$p_{i+1} = p_i + (1-\gamma)(p_i - p_{i-1}) + \alpha F_{int} + \beta F_{grad} + \kappa F_{speed} \tag{4.1}$$

The internal force F_{int} is a regularization force that controls the smoothness of the surface [Delingette 1999]. The gradient force F_{grad} and the speed force F_{speed} are external forces that are derived from the image data and steer the simplex mesh onto boundary structures. The parameter γ was set to 1 in this study, hereby removing the contribution of the damping coefficient from the model and avoiding oscillatory behaviour of the deformable model. The parameters α, β and κ are weighting factors to balance the different forces. F_{grad} is defined as:

$$F_{grad}(p_i) = \nabla \frac{1}{1 + \exp - \frac{|\nabla G_\sigma * I_{AMS}(x_i, y_i, z_i)| - \delta_{grad}}{\gamma_{grad}}} \tag{4.2}$$

where I_{AMS} stands for image intensity (echo level) of the AMS-filtered data. Sigmoidal intensity mapping with parameters γ_{grad} and δ_{grad} is used to scale the gradient magnitude to the interval $[0, 1]$. The parameters γ_{grad} (width of the sigmoid), and δ_{grad} (center of the sigmoid), are based on the minimum and average gradient magnitude value [Ibanez et al. 2003]. Gaussian smoothing (G_σ) with a small σ(0.5 mm) is applied to increase the width of the attraction potential and to smooth undesired small gradients inside the left ventricle. The derivative of the AMS filtered data after Gaussian smoothing was obtained in an efficient way by convolving the AMS filtered data with the derivative of a Gaussian kernel [Deriche 1990]. The speed force F_{speed} is an inflating force into the vertex normal direction as described by Böttger et al. [2007]:

$$F_{speed}(p_i) = \frac{1}{1 + \exp - \frac{|\nabla G_\sigma * I_{AMS}(x_i, y_i, z_i)| - \delta_{speed}}{\gamma_{speed}}} \tag{4.3}$$

The parameters δ_{speed} and γ_{speed} are chosen such that the speed force is greatly complementary to the gradient force, i.e. in general F_{speed} has high values in regions with no gradient information and has low values at boundaries and lies between 0 and 1. The speed force therefore reduces the need for close-to-boundary initialization of the mesh. Figure 4.1 shows an example of gradient and speed images of a single axial-lateral plane from a full volume dataset of a piglet heart, in scan-converted format.

The mesh is initialized by interactively placing a small spherical simplex mesh (radius = 3 mm, 128 vertices) within the left ventricle. Since the center of the left ventricle will always be located approximately in the center of the ultrasound volume and at a certain distance below the transducer, automatic placement of this initial region is feasible. A fixed, heuristically assessed set of weighting parameters was used for all datasets ($\alpha = 0.15$, $\beta = 0.005$, $\kappa = 0.005$). The deformation algorithm was applied to the demodulated echographic image data in scan-converted format, thus positions of vertices of the mesh corresponded to coordinates in mm. In contrast to the standard DICOM formatted ultrasound data, radiofrequency data have a very high axial resolution compared to the lateral and elevational resolutions. Resampling of the data to obtain equal resolution in all directions was not feasible as it resulted either in huge datasets (without adding extra information) causing memory problems, or in a decreased resolution in the axial direction. To handle these resolution differences, the spacing between pixels was incorporated into the deformation algorithm by using spacing dependent gradient and speed force computations. Therefore, the evolving simplex mesh model is able to account for the lower lateral and elevational resolutions compared to the axial resolution.

To deal with the complex anatomical structure of the papillary muscles and to enable the mesh to grow into small cavities, a mesh refinement operation [Böttger et al. 2007] was included in the algorithm. Based on a criterion that accounts for both cell area and curvature, the mesh is refined in an iterative manner during the deformation process by subdividing the cells. A cell is subdivided if the cell area belongs to the largest 50% of the cell area range. A cell is also subdivided if the curvature is higher than the overall average curvature of the mesh, provided that the cell area lies within the largest 95% of the cell area range. Due to this refinement algorithm, the deformation process can be started with a coarse initial mesh, and gradually the number of points in the mesh is increased when the mesh reaches the endocardial border. This coarse-to-fine approach provides less sensitivity to disturbance by noise in the initial phase of the deformation process, when all mesh vertices are located in the blood pool and the attraction of the endocardial borders is not strong yet.

The algorithm was stopped automatically when (1) the overall displacement of all vertices was below a threshold, or (2) after 600 iterations.

4.2.5 Cardiac Output Measurement

According to recent literature, the use of a highly invasive transit-time flow probe as described in the animal model section, is the most gold standard for intra-operative measurement of cardiac output [Botero et al. 2004; Bajorat et al. 2006; Lemson et al. 2008]. It should be noted that in absence of a hemodynamic shunt, the pulmonary blood flow equals the left ventricular output. We preferred to measure pulmonary blood flow as the gold standard of cardiac output and not blood flow through the ascending aorta, because the latter lacks coronary blood circulation. In the piglet model, the average cardiac volume flow (ml/min) was continuously measured in the pulmonary artery by the ultrasonic flow probe and could serve as the gold standard to validate cardiac output as computed by the segmentation algorithm.

The deformable simplex mesh was used to segment the endocardial surface in the end-diastolic (ED) and end-systolic (ES) phases. Corresponding volumes (EDV and ESV) were calculated to compute the cardiac output (ml/min):

$$CO = (EDV - ESV)\,HR \qquad [ml/min] \tag{4.4}$$

where HR stands for heart rate (bpm). For each piglet, one single flow measurement was compared with the corresponding cardiac output derived from the ED and ES volume obtained by the segmentation method, i.e., five paired measurements were done.

4.2.6 Statistical Analysis

Linear regression and Bland-Altman analysis were used to illustrate the relation between flow-based and segmentation-based CO measurements. To investigate the dependency of the segmentation based CO measurement on different initializations of the algorithm, five different seed points were positioned by one operator in the left ventricle for each dataset. For each dataset, the CO value averaged over five initializations was used to estimate the linear regression line and corresponding correlation coefficient. The inter-image segmentation variability was tested by comparing flow-based vs. segmentation-based CO for three different datasets from one animal. A box-and-whisker plot was used to visualize the results.

4.3 Results

The method was tested on full volume image sequences of five piglets (one measurement per animal). Heart rates varied from 138 to 148 bpm. Figure 4.2 and Fig. 4.3 show the segmentation results in ED and ES phase, respectively, obtained intra-operatively in a non-standard ultrasound view. Three cross-sectional planes and a 3D view are overlaid with the endocardial contour and endocardial surface, respectively. As the algorithm searches for transitions between blood and muscle tissue, papillary muscles were excluded from the endocardial volume. As no *a priori* knowledge about the viewing angle was included and no shape constraints were used, the segmentation method did not encounter problems with this non-standard view. Satisfactory segmentation results were obtained in all animals, i.e., the algorithm stopped close to the endocardial wall.

To obtain an indication about the initialization dependency, for each dataset, five different initial seed points were chosen to run the segmentation algorithm. Table 4.1 summarizes estimated segmentation-based values of EDV and ESV, and segmentation versus flow-based CO measurements for all datasets and all initializations. It can be seen that the variability of the heart rate is small. Relative errors between flow-based CO and segmentation-based CO varied from 0 to -17% with a mean relative bias of -7.9%. It should be taken into account that the accuracy of the flow meter is 10% and the accuracy of the volume computation of the simplex

Table 4.1: Mean and standard deviation values for 5 animals of EDV (segmentation-based), ESV (segmentation-based), segmentation based CO, flow based CO, absolute errors and relative errors in quantification of CO.

	EDV_{seg} ml	ESV_{seg} ml	CO_{seg} ml/min	CO_{flow} ml/min	Abs. Error ml/min	Rel. Error %	HR bpm
Mean	6.7	2.5	596	642	54	-7.9	142
SD	2.3	1.5	180	178	29	6.2	5.9

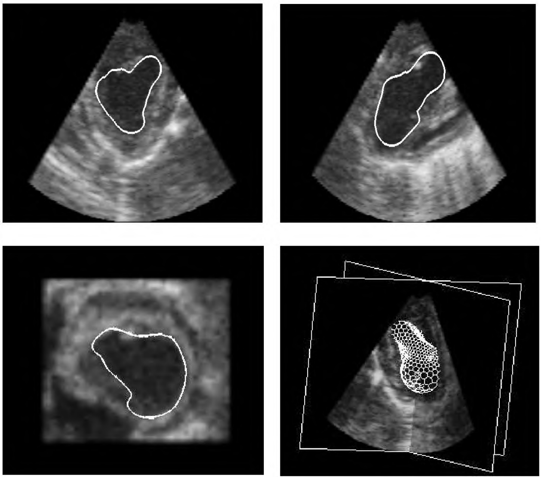

Figure 4.2: End-diastolic volume resulting after simplex mesh deformation in a full volume image of a piglet heart (intra-operative). Axial-elevational (*upper left*), axial-lateral (*upper right*) and lateral-elevational (*lower left*) planes overlaid with contour of the segmented endocardial surface and 3D view (*lower right*).

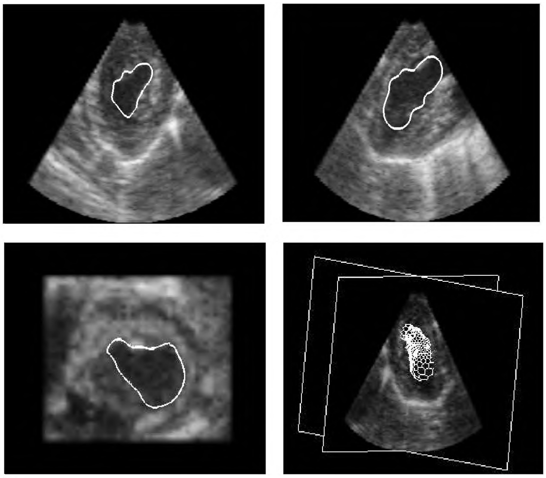

Figure 4.3: End-systolic volume resulting after simplex mesh deformation in a full volume image of a piglet heart (intra-operative). Axial-elevational (*upper left*), axial-lateral (*upper right*) and lateral-elevational (*lower left*) planes overlaid with contour of the segmented endocardial surface and 3D view (*lower right*).

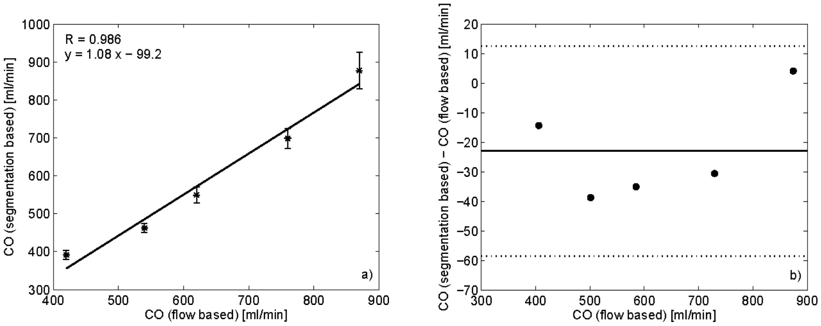

Figure 4.4: a) Cardiac output values (*ml*/*min*) for flow-based measurement (*horizontal axis*) and segmentation-based measurement (*vertical axis*) for five piglets with corresponding linear regression line (r = 0.99). Error bars depict mean and standard deviation for 5 different initialization seed points to illustrate initialization dependency. b) Corresponding Bland-Altman plot. For each animal, segmentation-based measurements were averaged over five different initializations.

mesh [Alyassin et al. 1994] is 4%.

Figure 4.4 presents the relation between flow-based and segmentation-based CO measurements. For each dataset, segmentation-based CO measurements were averaged over the five different initialization seed points, mean and standard deviation as a result of the initial position of the seed point are given by error bars. It can be derived from the linear regression line in Fig. 4.4a that segmentation-based CO estimates (y) are highly correlated to the gold standard flow-based measurements (x) (regression y = 1.08x -99.2, r = 0.99). From the Bland-Altman plot (Fig. 4.4b) it can be concluded that segmentation-based values underestimated flow-based measurements, except for the piglet with the largest CO. For this specific dataset, low echogenicity of the myocardium caused segmentation errors in the ED phase, leading to overestimation of the EDV.

For one animal three datasets were recorded successfully. The interval between the three measurements was about five minutes, and flow values varied between 840 and 950 ml. Figure 4.5 shows a box-and-whisker plot (illustrating initialization dependency) for each dataset together with the gold standard flow measurements. Good agreement between flow-based and segmentation-based CO was found for these three datasets, thereby giving an indication for the inter-image segmentation variability.

4.4 Discussion and Conclusion

According to the results of this cardiac output study, segmentation of the endocardial surface by a combination adaptive filtering and deformable simplex meshes has been proven to be feasible. The results show that the method yields excellent correlation values with respect to the gold standard intra operative cardiac flow

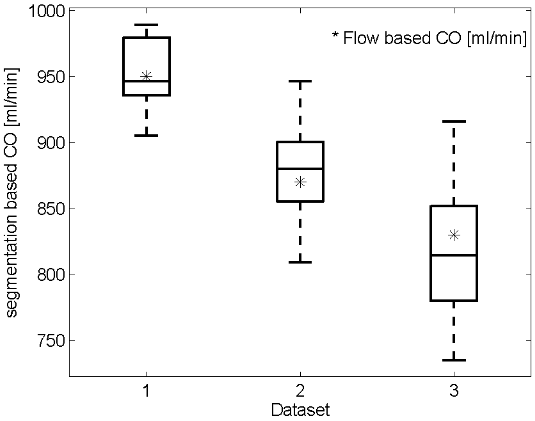

Figure 4.5: Segmentation variability for three different datasets of one animal. Box-and-whisker plots illustrate initialization dependency for five different initializations for each dataset. Corresponding flow probe measurements are depicted by an asterix.

measurements results. The data used in this study were evenly distributed over a broad spectrum of CO values and therefore are a representative set of data for validating the segmentation based CO measurements.

Underestimation of the flow based CO was reported for the segmentation based CO in all but one dataset. An explanation for the underestimation of the CO in all other datasets is the relatively low temporal resolution of the full volume data. In full volume mode, only 10 to 12 volumes were recorded each heartbeat at a frame rate of 25 Hz. The low temporal sampling leads to underestimation of the EDV and overestimation of the ESV. Hence, the CO measurement will result in an underestimation.

For visualization and segmentation of the entire left ventricle, full volume mode imaging is required. Although this imaging mode contains rich 3D information, the in-plane resolution is low and the gradients, in particular in the lateral-elevational plane, are unreliable. Furthermore, the presence of low contrast between blood and myocardium in some regions induces sometimes segmentation errors. In one of the datasets, this low contrast in a certain region of the myocardium caused inappropriate segmentation, leading to overestimation of the EDV. Addition of attractor forces in Eq. 4.1 might solve this problem and has been proven to be helpful [Böttger et al. 2007]. Adding such a force leads to interactive segmentation where the user can prevent the model from crossing weak boundaries and also may force it to evolve to an anatomical landmark like the apex or mitral annulus. Trabeculations of the endocardial wall may cause a systematic underestimation of the left ventricular volume in echographic images, as the space between these trabeculations is echographically not filled up with blood, like in

MRI techniques. However, for cardiac output estimation this might be of minor influence, since both in systole and in diastole this space is discarded. The method could cope well with the non-standard angle of view of the left ventricle as no specific geometric assumptions were included in the method. Segmentation of the full volume images was also performed with conventional ultrasound quantification software for segmentation of the LV (3DQ-QLAB 6.0, Philips Medical Systems, Best, the Netherlands). This software is appropriate for analyzing the left ventricle or left atrium in standard apical echocardiographic images in adults. As can be expected, this method did not yield satisfactory segmentation results due to the non-standard view and particular shape of the piglet heart, since in this method assumptions about the shape and orientation of the left ventricle are incorporated.

The method could also be applied to the right ventricle. In future we like to extend the method to a coupled model for segmenting the left and right ventricles, or for segmenting both endocardium and epicardium. Segmentation information from neighboring time frames could be used to incorporate the temporal information available from 3D + t echographic image sequences.

New-generation transducers will produce higher quality images, thereby facilitating more precise segmentation. The image quality of a first generation matrix array transducer, while using an intra-operative approach, might be similar to that of the latest generation transducers in a transthoracic approach. These transducers use both higher frequencies (especially suited for pediatric applications), and sophisticated transducer materials, for example 'Pure Crystal Technology'. Furthermore, underestimation of the CO due to the low temporal resolution will be reduced using the most recent systems, since they have the capability of acquiring data at 50 volumes/second.

In conclusion, the developed method is promising for non-standard ultrasound views and it might be a helpful tool for cardiac output measurement. These results warrant further investigations in newborn children with a congenital heart disease to automatically segment the geometry of the heart and identify the malformation.

Acknowledgements

This work is supported by Philips Medical Systems and the Dutch Technology Foundation (STW), project 06466. The assistance of Ronald Tanke by the echographic imaging of the piglets is gratefully acknowledged.

5

PERFORMANCE OF TWO DIMENSIONAL DISPLACEMENT AND STRAIN ESTIMATION TECHNIQUES USING A PHASED ARRAY TRANSDUCER

Based on: R. G. Lopata, M. M. Nillesen, H. H. Hansen, I. H. Gerrits, J. M. Thijssen, and C. L. de Korte. Performance of Two Dimensional Displacement and Strain Estimation Techniques using a Phased Array Transducer. *Ultrasound Med Biol* 35(12):2031-2041, 2009.

5

Abstract

The goal of this study was to investigate the applicability of conventional 2D displacement and strain imaging techniques to phased array radiofrequency (RF) data. Furthermore, the possible advantages of aligning and stretching techniques for the reduction of decorrelation artefacts was examined. Data from both realistic simulations and phantoms were used in this study. Recently, the used processing concepts were successfully applied to linear array data. However, their applicability to sector scan data is not trivial because of the polar grid. Homogeneous and inhomogeneous tissue phantoms were simulated at a range of strains (0 to 5%) using Field II©. The inhomogeneous phantom, a commonly used tumor/lesion model, was also constructed using gelatin/agar solutions. A coarse-to-fine displacement algorithm was applied, using aligning and stretching to enhance re-correlation. Vertical and horizontal strains were reconstructed from the axial and lateral displacements. Results revealed that the error on displacement estimates was lower when using 2D data windows rather than 1D windows. For regions at large depths and large insonification angles, the allowed lateral window size was limited. Still, 1D windows resulted in larger errors. The re-correlation techniques resulted in a significant increase in the elastographic signal-to-noise ratio (SNRe) and elastographic contrast-to-noise ratio (CNRe) of the vertical and horizontal strain components. An increase of the SNRe of 5-20 dB was observed over a range of strains (0.5 to 5.0%). In the inhomogeneous phantom, a vertical SNRe of 27.7 dB and a horizontal SNRe of 16.7 dB were measured in the background. The vertical and horizontal CNRe were 35 dB and 23.1 dB, respectively. For the experimental data, lower SNRe (vertical: 19.1 dB; horizontal: 11.4 dB) and CNRe (vertical: 33.3 dB; horizontal: 12.5 dB) were found. In conclusion, 2D window matching of sector scan data is feasible and outperforms 1D window matching.

Furthermore, the use of re-correlation techniques enhances both precision and contrast of strain images.

5.1 Introduction

Strain imaging, or elastography, is a technique to measure the deformation of tissue [Ophir et al. 1991, 1999]. The resulting strain images may be used to estimate the elastic and mechanical properties of tissue. The technique has been adapted for a large variety of applications, such as the detection of lesions and tumors [Céspedes et al. 1993], breast tumors [Garra et al. 1997], atherosclerotic plaques [de Korte et al. 2000] and blood clots [Emelianov et al. 2002]. Quasi-static and external compression of phantoms or tissues are often used [Céspedes et al. 1993; Varghese et al. 1996; Konofagou and Ophir 1998]. The technique can also be applied to assess functional properties of actively deforming tissue such as skeletal muscle [Kallel et al. 1998; Tanter et al. 2002] and the heart [D'hooge et al. 2000; Konofagou et al. 2002; D'hooge et al. 2002; Luo et al. 2007]. In most applications, linear array transducers are used. An advantage of linear array transducers is the equidistant, parallel spacing of the ultrasound beams.

In a clinical setting, phased array transducers are often used for cardiac applications. The pyramid shape of the image sector and the small footprint of the transducer are required to perform intracostal imaging of the entire adult heart. New real-time 3D techniques are becoming more and more available. The pyramid-shaped sector scan data of 2D and 3D matrix array systems are comprised in a polar coordinate system with nonequidistant line spacing. Matrix array transducers are not only used for cardiac strain imaging, but can be used for several applications where high frame rates are required, e.g., measuring 2D and 3D skeletal muscle deformation [Lopata et al. 2006].

Diverging ultrasound beams are also a property of data acquired with a curved array transducer. This type of transducer is especially designed to image large organs both at shallow and at larger imaging depths and it can also be used for strain imaging. Examples are strain imaging of the vessel wall in larger vessels such as the aorta [Hansen et al. 2008] and the detection of tumors in the liver or prostate [Khaled et al. 2006]. However, these data suffer from the same divergence of ultrasound beams, which results in axial and lateral strains that are not aligned with the directions of the strains of interest. The difference in coordinate system is certainly an issue for skeletal muscle, (prostate) tumors and long-axis acquisitions of the left ventricle. Moreover, it must be noted that the misalignment is always the case in vessels (besides the exception of intravascular strain imaging) and for the short-axis view of the heart's left ventricle, because these geometries require different corrections and/or projections [Ribbers et al. 2007; Lee et al. 2007].

It was previously shown that de-correlation reduces tracking precision [Alam and Ophir 1997]. The effects of de-correlation can partly be overcome by global stretching of the radiofrequency (RF) data [Varghese et al. 1996]. This method works fine for homogeneous tissue deformed by an external compression device, but not always *in vivo*, where the deformation might be distributed nonuniformly. Besides, the applied or present strain cannot be controlled in actively deforming tissue. Especially at limited frame rate, the deformation rate can become too high, which leads to high de-correlation of post-deformation signals, which may cause inaccuracies and biased strain estimates [Alam and Ophir 1997]. Besides, large translations of signal segments will cause problems for smaller search windows. Therefore, a relatively high frame rate is required, for instance in cardiac applications, to suppress these effects [Langeland et al. 2005; Luo et al. 2007].

In a previous paper on RF-based 2D strain imaging, the effects of local techniques such as window aligning and local stretching were evaluated using linear array data. A significant increase in the SNRe of strain estimates in both the axial and lateral directions was observed [Lopata et al. 2009], and the contrast of the lesion showed similar improvement. Besides lesion detection, the local aligning and stretching techniques might be especially beneficial for data obtained in uncontrolled, strongly deforming structures such as skeletal muscle and the heart. The study also revealed that the processing of 2D windows of RF-data is favorable and increases the precision of the measured displacements compared with the 1D condition. As mentioned before, the data of phased array and curved array transducers are collected in a non-Cartesian coordinate systems with nonequidistant line spacing. Hence, the use of 2D windows for displacement and strain estimation is not trivial, and despite expected robustness, the potential applicability was questioned [Langeland 2007].

In the present study, the applicability of 2D windows for estimation of strain in 2D using phased array RF-data is investigated. An iterative, correlation-based coarse-to-fine displacement estimation algorithm was implemented [Shi and Varghese 2007] using 2D data kernels and a fast 2D parabolic interpolation of the cross-correlation peak [Lopata et al. 2006, 2009] and its performance was analyzed. This method was previously evaluated using linear array ultrasound data and is now applied to phased array data. Secondly, the applicability and benefits of re-correlation techniques, i.e., aligning and local stretching, on phased array RF-data is examined.

A commonly used lesion/tumor model was chosen, because it enables the assessment of accuracy, precision (elastographic signal-to-noise ratio [SNRe]) and detectability (elastographic contrast-to-noise ratio [CNRe]) of a technique. In addition, the chosen setup allows a comparison with linear array-based strain estimation techniques and other studies. Another approach would be using simulated cardiac datasets. This approach has been extensively investigated by several groups in different studies [Lee et al. 2007; Gao et al. 2007; Jia et al. 2007]. However, the aim of this study is assessment of the performance of the method and not the ability to measure cardiac strain. SNRe can be measured using a homogeneous phantom and CNRe can only be adequately measured using an inclusion phantom. The technique was experimentally validated using simulations and data of gelatin/agar phantoms.

5.2 Materials and Methods

5.2.1 Simulations

Raw (RF) ultrasound phased array data of a homogeneous and an inhomogeneous tissue-mimicking phantom were simulated to evaluate the performance of the 2D strain algorithm. The inhomogeneous phantom was originally developed as a phantom-mimicking soft tissue with a hard lesion or tumor [Céspedes et al. 1993; Ponnekanti et al. 1995; Kallel et al. 1996].

A homogeneous and an inhomogeneous phantom were simulated as described previously by our group [Lopata et al. 2009]. The applied average vertical deformations of the homogeneous phantom were 0.5%, 1.0%, 2.0%, 3.0%, 4.0% and 5.0%, respectively. The range of the resulting vertical and horizontal displacements is listed in Table 5.1. The finite element method (FEM) model of the inhomogeneous phantom was solved for the case of 2.0% applied average vertical deformation. The displacements and strains of the inhomogeneous phantom are shown in Fig. 5.1a-d; the dashed lines indicate the image sector. Two-dimensional sector scan images were simulated using the Field II© ultrasound simulation software [Jensen 1996]. A phased array transducer was modeled for a center frequency of 3.5 MHz, corresponding with the center frequency of the X4 matrix array transducer of the SONOS 7500 real-time 3D system (Philips Medical Systems, Bothell, WA, USA) used for the experimental phantom study. The simulated transducer consisted of a phased array of 128 elements, using all elements in both transmit and receive mode, no apodization was implemented. The pitch was set to 50% of the wavelength, with an element width of 198 μm (45% of the wavelength) and an element height of 6 mm. The aperture had a fixed transmit focus, set in the center of the phantom (at 35 mm). To obtain a more homogeneous beamwidth, dynamic focusing was used by adding so-called receive focal zones every 4.0 mm. For each image, a total of 121 RF-lines was simulated, with an incremental angle of 0.75°, resulting in a total image sector of 90°. The digital

Table 5.1: Displacements and strains in the simulated homogeneous phantom

Applied axial strain (%)	Lateral strain (%)	Axial displacements (mm)	Lateral displacements (mm)
-0.5	0.25	-0.25 to 0	-0.06 to 0.06
-1.0	0.5	-0.50 to 0	-0.12 to 0.12
-2.0	0.99	-1.00 to 0	-0.25 to 0.25
-5.0	2.48	-2.50 to 0	-0.62 to 0.62

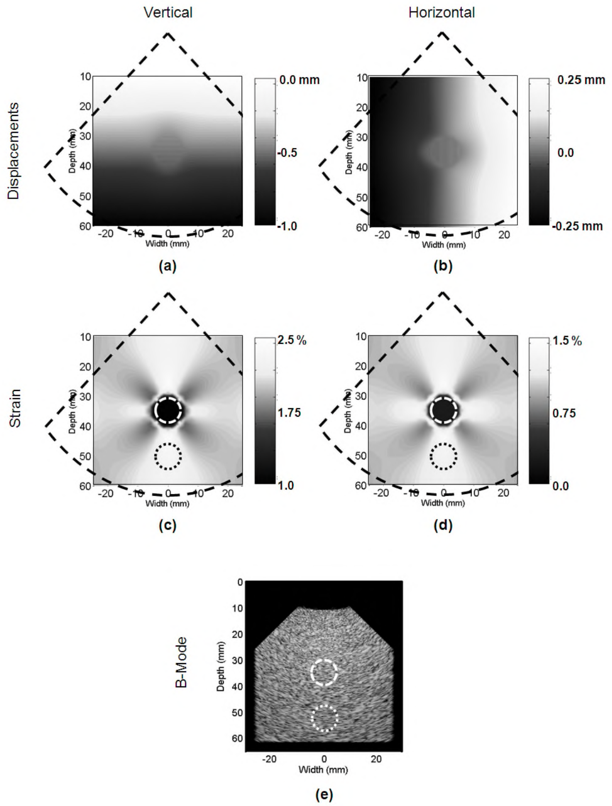

Figure 5.1: The solutions of the finite element model; the displacement in vertical direction (a) and horizontal direction (b) and the strain in vertical (c) and horizontal (d) direction. The dashed, rectangular region corresponds to the field-of-view of the simulated ultrasound images. An example of a simulated ultrasound image of the inhomogeneous phantom is shown (e). The white, dashed circle indicates the ROI within the inclusion and the white, dotted circle is the background ROI, both used for SNRe and CNRe analysis.

sampling frequency was set to 30 MHz.

The input of the Field II© software was a 3D matrix of randomly placed point-like scattering particles. Because the -20 dB elevational beamwidth was determined to be smaller than 1.0 cm for all echo depths, a "tissue" slice of 5 × 5 × 1 cm was used for 2D image simulation rather than using the entire block. The total amount of scatterers within the slice volume was $3.5 \cdot 10^6$, which is equal to 10 scatterers per smallest resolution cell. This number is sufficient to guarantee fully developed speckle in the US image [Oosterveld et al. 1985]. For the post-compression images, the scattering particles were translated using the solutions of the FEM of the tissue-mimicking phantoms. RF-data of both phantoms were simulated for the different levels of compression. An example of a 2D sector scan B-mode image is shown in Fig. 5.1e.

5.2.2 2D displacement estimation

For an extensive overview of the used approach, we refer to Lopata et al. [2009]. In the present paper, a coarse-to-fine displacement estimation algorithm was used to estimate the axial and lateral displacements. Two-dimensional windows of data were cross-correlated and the resulting peak was detected using a 2D parabolic interpolation for fast and accurate 2D subsample displacement estimation. The algorithm used the signal envelope at coarse scale (first step) and RF-data for all subsequent steps. The axial window size was set to 8.0, 4.0 and 2.0 mm, respectively, for the pre-compression window, and was two times bigger in the post-compression window (16.0, 8.0 and 4.0 mm, respectively).

To examine the influence of lateral window size, the displacements were estimated using 1, 3, 5, 7, 9, 11, 15 and 21 lines, respectively, in the pre-compression kernel. The post-compression kernel was extended with three lines on both sides (i.e., 6 lines more in total). It must be noted that the effective kernel size becomes larger for increasing depth. For this reason, the lateral kernel size is expressed in lines instead of millimeters. The root-mean-square error (RMSE) was calculated using the unfiltered displacements and the theoretical displacements of the FEM solutions. This error criterion was chosen because the direct influence on displacement precision can be measured without any influence of filtering or of the used strain estimator, whatsoever. The SNRe was also measured for a circular ROI centered in the phantom (see Fig. 5.1e).

5.2.3 Re-correlation by aligning and stretching

Next, the effect of aligning and stretching was examined. The coarse-to-fine procedure was repeated for precompression axial window sizes of 8.0, 4.0 and 2.0 mm and five lines in the lateral direction. As before, the post-compression windows were two times larger. After the final coarse-to-fine step, the pre- and post-compression data were aligned at subsample level using the measured displacements after median filtering and spline interpolation. The axial displacements were filtered with a median filter of 11 × 5 pixels. A filter of 11 × 11 pixels was used for the lateral displacements. In case of phased array data, the vertical and axial strains are not aligned. The measured axial strain is used to stretch the 2D kernel of RF- data in the axial direction to enhance correlation [Lopata et al. 2009].

The axial and lateral strains (and shear components) were calculated using a least-squares strain estimator (LSQSE) of 4.9 mm in the axial direction and 11 samples (i.e., 11 lines kernel width) in the lateral direction (Kallel and Ophir

1997). The vertical and horizontal displacements and strains were reconstructed from the axial and lateral displacements/strains using a transformation of the coordinate system (see the Appendix and Fig. 5.7). The RMSE, SNRe and CNRe (in the inhomogeneous phantom only) were calculated for all steps of the algorithm, i.e., coarse-to-fine, aligning and stretching, for all simulated datasets.

5.2.4 Phantom study

The inhomogeneous phantom was constructed using gelatin/agar solutions for assessment of the SNRe and CNRe of the method using a real phantom and experimental ultrasound signals. A block of soft tissue was made using a mixture that consisted of an 8%-by-weight gelatin (Dr. Oetker, Ede, The Netherlands) solution in water, with an addition of 1% by weight agar-agar (Boom, Meppel, The Netherlands). Furthermore, 2.0% by weight-scattering particles (40 to 63 μmSiC, E. Merck, Darmstadt, Germany) were added for mimicking tissue scattering. The cylindrical inclusion consisted of 8.0% by weight gelatin and 3.0% by weight agar-agar solution. The resulting inclusion was approximately four times stiffer than the inclusion [de Korte et al. 1997; Lopata et al. 2009], consistent with the used FEM.

The phantom was deformed using an automated compressor setup. The transducer of the ultrasound system (US) was anchored in the center of the top plate. The plate was moved to compress the phantom in steps of 0.5 mm up to a total of 5.0 mm (0.5% to 5.0% strain). After each applied deformation step, 2D phased array images were acquired. The raw BiPlane data were recorded with a Philips SONOS 7500 real-time 3D system (Philips Healthcare, Andover, MA, USA), equipped with a 4-MHz, 3D matrix array transducer (X4), and were sampled at 19.5 MHz. The displacements and strains were estimated using the optimal settings as found in the simulation study. Next, the simulated and experimental data were compared in terms of SNRe and CNRe.

5.3 Results

Figure 5.2 shows the RMSEs for the measured axial and lateral displacements as a function of lateral precompression window size. The analysis was performed for six different regions of the B-mode sector image. Each region-of-interest (ROI) contained an equal amount of pixels for fair comparison. As expected, the axial RMSE was found to be lower than the lateral RMSE, except for region "d". For the other regions, the RMSEs were found to be higher for larger image depths and larger angles. In general, the use of 2D windows yielded lower RMSEs compared with a lateral window size of a single line. It seems that a minimum in RMSE is present for lateral window sizes between three and 11 lines. There is an abrupt decrease in RMSE when comparing the use of 1D kernels to the most narrow 2D kernel of three lines. The SNRe of the vertical and horizontal strains is shown in

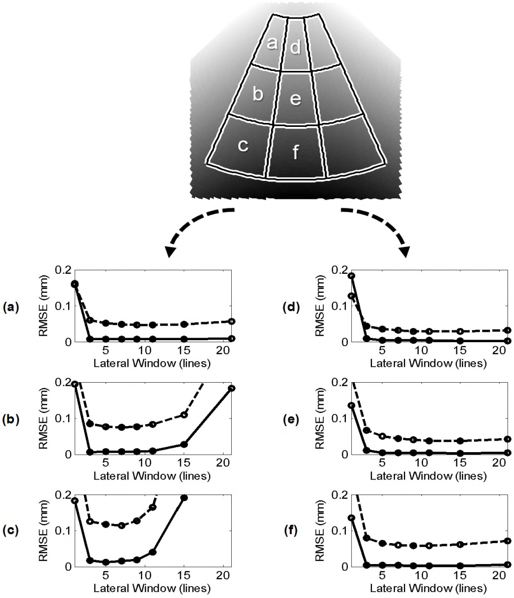

Figure 5.2: Axial (*solid*) and lateral (*dashed*) RMSE for increasing lateral kernel size for six different regions (a-f) within the homogeneous phantom at 2.0% applied load.

Fig. 5.3. SNRe was derived from the indicated regions (a and b) in the homogeneous phantom for strains ranging from 0.5-5.0%. The shape of the SNRe curves is similar to the strain filter [Varghese and Ophir 1997] for the first three steps of the strain estimation procedure (coarse to fine). After aligning and stretching, an increase in SNRe is observed in the vertical and horizontal directions. Although for smaller applied (vertical) strains ($\leq 1.0\%$), there is some benefit from using aligning and stretching (+6 to 8 dB), a much greater improvement was observed for 5.0% strain (+21 dB). The final range of vertical SNRe is 33-37 dB for the inner region (b) and only 23-33 dB for the outer region (a), because of the larger angle between ultrasound beam and axial deformation. For the horizontal strains, the final range for region (b) is 10-14 B. The increase in SNRe after aligning (5 to 19 dB) is significantly higher compared with stretching (2 to 3.5 dB). The vertical and horizontal SNRe are shown for the entire image in Fig. 5.4 for the cases of 2.0% and 5.0% applied load. The SNRe of the strains in both directions decreased significantly for increasing insonification angle, especially for 5% load. The modeled (FEM) and the measured displacement and strain images are shown in Fig. 5.5a-5.5h. In the inhomogeneous phantom variation of the strain occurs within

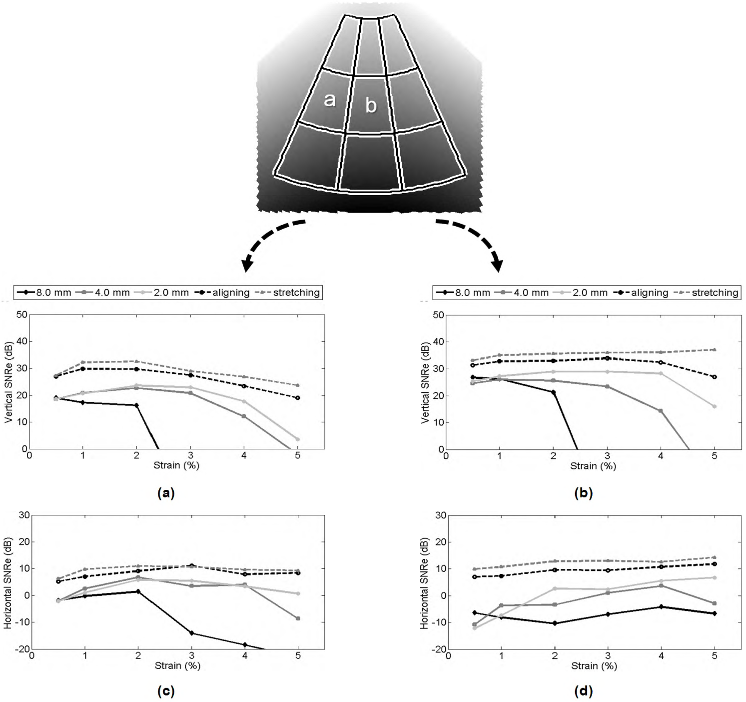

(a)

(b)

(c)

(d)

Figure 5.3: The calculated SNRe for the simulated homogeneous phantom as a function of applied strain (0.5 to 5.0%) for all steps of the algorithm. The vertical and horizontal SNRe are given for two regions in the homogeneous phantoms at the outer (a) and middle section (b).

the chosen ROIs (Fig. 5.1c-5.1e). The theoretical maximum SNRe and CNRe were calculated from the FEM solutions and compared with estimated values from the simulated images (see Fig. 5.5 and see Table 5.2). The theoretical and measured vertical SNRe were 28.2 and 27.7 dB, respectively (see Fig. 5.5i). The corresponding obtained vertical CNRe was 35.0 dB compared with a theoretical value of 40 dB. In the horizontal direction, the theoretical SNRe and CNRe were 23.2 and 36.1 dB, respectively. The obtained maximum values in the simulations were 16.7 and 23.1 dB (Fig. 5.5j-5.5l). The quality of the strain images of the phantom is illustrated in Fig. 5.6 and the SNRe and CNRe values are listed in Table 5.2. The mean and standard deviation of the SNRe and CNRe, based on 10 datasets, are given for the vertical and horizontal strain (Fig. 5.6). The used regions correspond with the used regions in the simulation study (Fig. 5.1e). The vertical SNRe of 19 dB was approximately 9 dB lower compared with the simulation study, but the CNRe was almost identical. The horizontal SNRe and CNRe were 11.4 dB and 12.5 dB, respectively, almost 5 and 10 dB lower than in the simulated data.

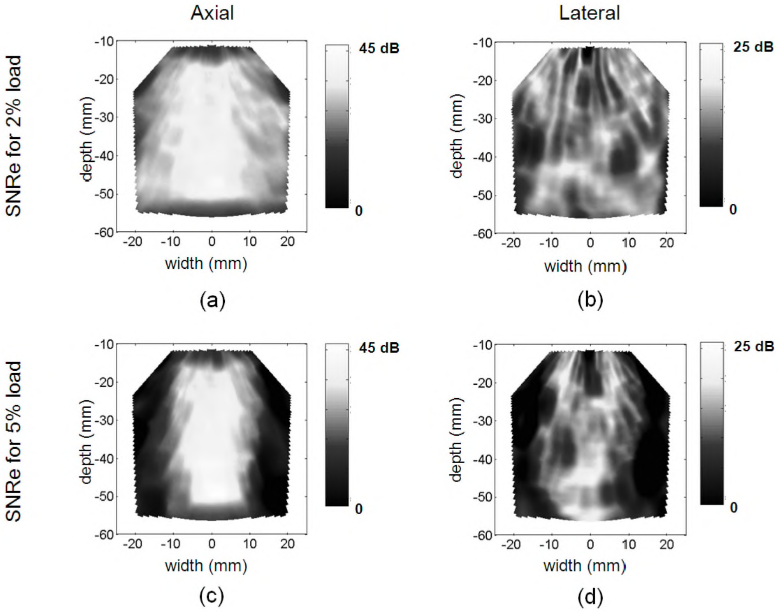

Figure 5.4: The calculated vertical and horizontal SNRe for the simulated homogeneous phantom images at 2.0% and 5.0% applied load. Each SNRe value was calculated for a region of 11 × 11 strain pixels.

Table 5.2: Comparison of the SNRe and CNRe Values (Final Step of the Algorithm)

	Vertical SNRe (dB)	Vertical CNRe (dB)	Horizontal SNRe (dB)	Horizontal CNRe (dB)
FE model	28.2	40.0	23.2	36.1
Simulation	27.7	35.0	16.7	23.1
Experiment	19.1	33.3	11.4	12.5

5.4 Discussion

The main finding of the first part of the study is that the use of 2D pre- and post-compression windows is to be preferred over 1D pre-compression windows, but that the lateral window size should be limited. The upper sector image region ('d' in Fig. 5.2) has the smallest distance between RF-lines and the lowest insonification angle. Therefore, the RF-lines may be considered similar to linear array data. The results also showed close resemblance to those obtained from linear data, in which the largest lateral window size yielded the lowest axial and lateral RMSEs [Lopata et al. 2009]. At greater depths, the RMSE values became higher

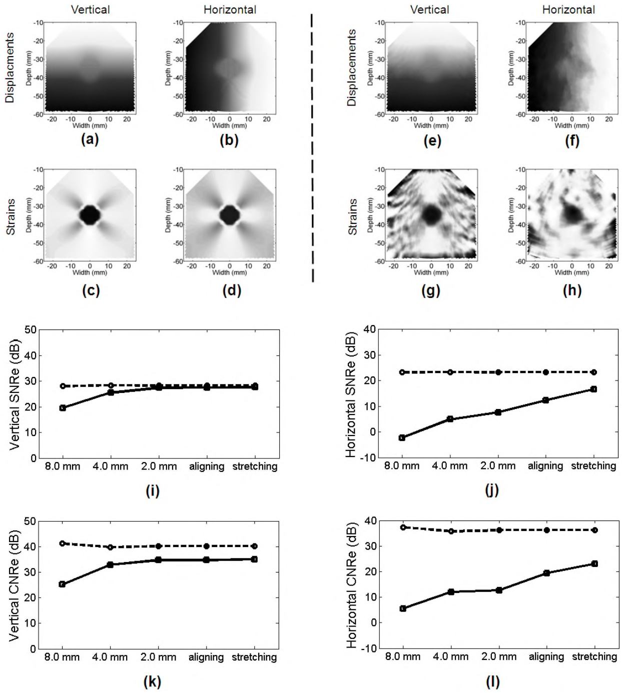

Figure 5.5: The FEM displacements and strain images (a-d) and the measured displacement and strain images (e-h). The SNRe and CNRe of the simulated data of an inhomogeneous phantom for all steps of the strain estimation algorithm (*solid lines*): (i) the SNRe of the vertical strain; (j) the SNRe of the horizontal strain; (k) CNRe of the vertical strain; (l) CNRe of the horizontal strains. The maximum theoretical SNRe and CNRe are calculated using the finite element model (*dashed lines*).

for increasing lateral window sizes. The upper limit on the used lateral window size was also clearly visible for all outer regions. This phenomenon is probably caused by the larger insonification angle and by scatterer movement (discussed in detail later). But for all depths and insonification angles, the use of 2D windows improved the performance of the algorithm. The transition from 1D to 2D in terms of RMSE seems quite abrupt. However, no explanation of this phenomenon could be given and intermediate kernel sizes are not available. The optimization of the lateral window length revealed a minimum for the error of the axial and lateral displacement estimates. The authors would like to point out that this "optimal window length" probably depends on experimental conditions, i.e., the frequency characteristics of the used transducer, incremental angles, applied strain, horizontal movement, etc.

Analysis of the SNRe and CNRe of the strain components revealed an improve-

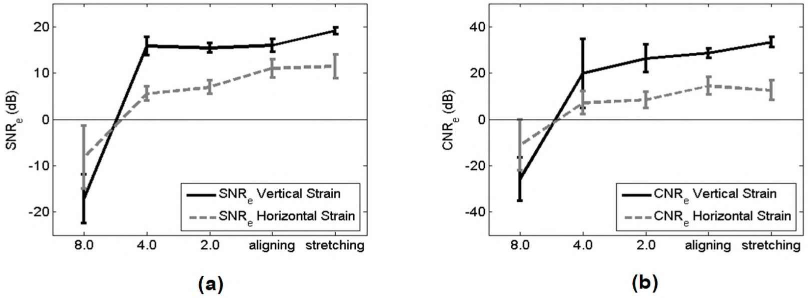

Figure 5.6: The mean and standard deviation of the measured SNRe and CNRe for experimental data of an inhomogeneous phantom (n = 10) for all steps of the strain estimation algorithm: (a) SNRe of the vertical (*black, solid*) and horizontal strain (*gray, dashed*); (b) CNRe of the vertical (*black, solid*) and horizontal strains (*gray, dashed*).

ment for each step of the coarse-to-fine algorithm. Realigning significantly improves horizontal strains by up to +19.0 dB. This is in accordance with previous work [Konofagou and Ophir 1998; Lopata et al. 2009] despite the nonequidistant line spacing. Stretching yields a large improvement of the accuracy of vertical strain, especially at higher applied strains (+10 dB at 5.0% applied strain). Hence, aligning is necessary for an improvement of horizontal SNRe and stretching for vertical strains, which is again in accordance with our findings in a study of linear array data and proves that aligning and stretching is also beneficial for sector scan data. A strain of 5.0% is not uncommon in cardiac data, depending on the frame rate. Therefore, local stretching will enhance the precision of strain estimates.

For the inhomogeneous simulation and phantom data, a similar increase in SNRe was observed for each step of the algorithm. The theoretical and measured SNRe values are lower compared with those obtained for the homogeneous simulation data at 2.0% applied strain. This can be explained by a different mean strain and corresponding variance in the chosen ROI caused by the inclusion (see Fig. 5.1c-5.1e). In general, the CNRe is lower in the simulation and phantom study compared with the theoretical upper limit (Figs. 5.5 and 5.6), probably caused by the use of median filtering and LSQSE. The horizontal SNRe and CNRe are considerably lower in simulations as well as the phantoms study, which is probably caused by the lower lateral sampling, the increasing spacing between RF-lines, the lack of phase information and the lower absolute horizontal strain, which is approximately 50% of the vertical strain (i.e., Poisson's ratio = 0.495).

In this study, we used a simulation and phantom model often used in performance assessment of elastographic techniques. In this way, a good comparison with previous work could be performed. It is clear that the geometry in cardiac application is different, but also in this application, radial and circumferential strain will be estimated from axial and lateral displacement estimates [Lee et al. 2007].

The RMSE and SNRe analysis reveal less precision of displacement and strain estimates for larger insonification angles. This is illustrated by the strain images, which reveal an increase of noise in all strains. This is observed in both the simulation study (Fig. 5.5) and the experimental data (not shown). The angle between the vertical and horizontal scatter movement increases with an increasing insonification angle. Hence, scatterers move through the RF-lines at an angle. This phenomenon is not present when using linear array data. Consequently, the re-correlation techniques are less beneficial, because the measured displacements and strains are less aligned with the present displacements and strains. Besides, vertical precision is lower because of the larger contribution of lateral displacement estimates to the vertical strain.

It is often questioned whether 2D kernels are applicable and beneficial for (cardiac) 2D strain estimation, since large shearing effects are present in the heart and diverging line data are used [Langeland 2007]. The combination of using 2D kernels and shearing can be problematic. The influence of shearing was not assessed, which is a limitation of the present study. The simulation and phantom studies do not indicate any problem for the strain estimation using 2D windows of diverging line data. Moreover, the use of 2D windows outperforms the 1D case in terms of precision, despite the lower precision at larger insonification angles. However, this issue is less problematic in cardiovascular data, where the strains of interest are more often the radial and circumferential strain, obeying a coordinate system that is better aligned with the phased array data. Besides, 2D windows enable the use of 2D parabolic interpolation. It should be noted that parabolic interpolation was chosen because this analytic interpolation scheme is fast and accurate [Lopata et al. 2009].

In conclusion, the use of 2D kernels of RF-data for 2D displacement and strain estimation is beneficial when the data are present in a polar grid as in sector scanning by phased array transducers. Furthermore, the precision and contrast of both strain components can be enhanced using re-correlation techniques, such as aligning and stretching. In general, the SNRe and CNRe is lower compared with linear array data, and the performance decreases with increasing depth and insonification angle. This approach can also be used for demodulated B-mode sector data.

Acknowledgements

This work was supported by Philips Medical Systems and the Dutch Technology Foundation (STW), project 06466.

Appendix

Sector scan data of a phased array transducer obey a polar grid (see Fig. 5.7). Initially, the displacements along and perpendicular to the ultrasound beam are measured, i.e., the axial (δ_{ax}) and lateral displacements (δ_{lat}), respectively (see

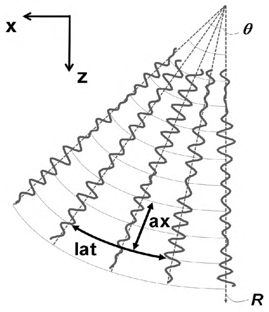

Figure 5.7: Schematic representation of phased array sector scan data and the two coordinate systems (polar and Cartesian).

Fig. 5.7). To reconstruct the displacements, in the actual vertical (z) and horizontal (x) directions, the rotation matrix is used to transform the measured displacement values in polar coordinates into Cartesian values of the displacements (x and z, respectively):

$$(z(r,\theta),x(r,\theta)) = (\delta_{ax}(r,\theta),\delta_{ax}(r,\theta))\cdot R \tag{5.1}$$

with r the radius (depth) and θ the angle of the received ultrasound beam, with respect to the z-axis. $z(r,\theta)$ is the vertical displacement vector and $x(r,\theta)$ is the horizontal displacement, both in polar coordinates. R is the rotation matrix:

$$R = \begin{bmatrix} \cos\theta & \sin\theta \\ -\sin\theta & \cos\theta \end{bmatrix} \tag{5.2}$$

After determining the spatial gradients of both displacement vectors z and x in the lateral ($\partial/\partial\theta$) and axial direction ($\partial/\partial r$), the vertical and horizontal strains are reconstructed using:

$$\begin{bmatrix} \epsilon_{zz} & \epsilon_{zx} \\ \epsilon_{xz} & \epsilon_{xx} \end{bmatrix} = \begin{bmatrix} \frac{\partial z}{\partial r} & \frac{\partial z}{\partial \theta} \\ \frac{\partial x}{\partial r} & \frac{\partial x}{\partial \theta} \end{bmatrix} \cdot R \tag{5.3}$$

with ϵ_{zz} the vertical strain, ϵ_{xx} the horizontal strain and ϵ_{zxz} and ϵ_{zx} the shear strains. This results in:

$$\begin{aligned} \epsilon_{zz} &= \frac{\partial z}{\partial r}\cos\theta - \frac{\partial z}{\partial \theta}\sin\theta \\ \epsilon_{zx} &= \frac{\partial z}{\partial r}\sin\theta + \frac{\partial z}{\partial \theta}\cos\theta \\ \epsilon_{xz} &= \frac{\partial x}{\partial r}\cos\theta - \frac{\partial x}{\partial \theta}\sin\theta \\ \epsilon_{zz} &= \frac{\partial x}{\partial r}\sin\theta + \frac{\partial x}{\partial \theta}\cos\theta \end{aligned} \tag{5.4}$$

6

TOWARDS 3D CARDIAC SEGMENTATION USING 2D TEMPORAL CORRELATION OF RADIO FREQUENCY ULTRASOUND DATA

Based on: M. M. Nillesen, R. G. P. Lopata, H. J. Huisman, J. M. Thijssen, L. Kapusta, and C. L. de Korte. 3D Cardiac Segmentation using Temporal Correlation of Radio Frequency Ultrasound Images. *Proc Med Image Comput Comput Assist Interv Lect Notes Comput Sc* 5762: 927-934; 2009.

6

Abstract

Semi-automatic segmentation of the myocardium in 3D echographic images may substantially support clinical diagnosis of heart disease. Particularly in children with congenital heart disease, segmentation should be based on the echo features solely since *a priori* knowledge on the shape of the heart cannot be used. Segmentation of echocardiographic images is challenging because of the poor echogenicity contrast between blood and the myocardium in some regions and the inherent speckle noise from randomly backscattered echoes. Phase information present in the radio frequency (RF) ultrasound data might yield useful, additional features in these regions.

A semi-3D technique was used to determine maximum temporal cross-correlation values locally from the RF-data. To segment the endocardial surface, maximum cross-correlation values were used as additional external force in a deformable model approach and were tested against and combined with adaptive filtered, demodulated RF-data. The method was tested on full volume images (Philips, iE33) of four healthy children and evaluated by comparison with contours obtained from manual segmentation.

6.1 Introduction

Three-dimensional (3D) segmentation of the endocardial surface could be a helpful tool for clinical assessment of 3D echocardiographic images. Segmentation may not only serve as an important tool for assessment of cardiac output and other functional parameters but also as a preprocessing step for tissue characterization, strain imaging and diagnosis of congenital deformities. Since manual segmentation of the left ventricle in 3D ultrasound image sequences is time-consuming and is subject to inter-expert variability, (semi-) automatic segmentation techniques are required (see [Noble and Boukerroui 2006] for an overview). The influence of speckle noise and the poor contrast in echogenicity between the blood and the heart wall in regions where the muscle fibers are mainly parallel to the propagation direction of the ultrasound beam, impose strong demands on the segmentation algorithm. Automatic segmentation purely based on differences in echogenicity will be problematic in these low echogenicity regions as the contrast between blood and myocardial tissue is absent. Therefore, a technique using temporal information might be beneficial.

Segmentation techniques using shape and appearance models of the left ventricle have been described [Bosch et al. 2002] to overcome these segmentation problems. However, in children with congenital deformities of the heart, inclusion of *a priori* knowledge about the average shape of the left ventricle will lead to erroneous segmentation results. The addition of temporal information by using cross-correlation techniques might facilitate segmentation in these problematic low contrast regions. Few segmentation methods use the rich phase information available in the radio frequency (RF) signal [Boukerroui et al. 2002; Davignon et al. 2005; Dydenko et al. 2003]. Yan et al. [2007] propose the use of maximum correlation coefficients obtained from a phase sensitive speckle tracking method for segmentation of the left ventricle.

This study builds on the work of Yan et al. [2007] and Chapter 3, using a combination of maximum cross-correlation values and adaptive mean squares (AMS) filter values as external forces of a gradient-based deformable simplex mesh model. The cross-correlation values were obtained from a semi-3D coarse-to-fine displacement algorithm (developed for strain estimation). This combined method was compared with segmentation results using correlation or AMS values as an external force separately. All results were evaluated by comparing them with manual segmentation.

6.2 Materials and Methods

Echocardiographic image sequences of the left ventricle were obtained in four healthy children. Echographic imaging was approved by the local ethics committee and parents gave their informed consent for using the data. Transthoracic full volume image sequences (ECG-gated, volume rate ≈50 Hz) were obtained in long/short axis views. RF-data were acquired directly after receive beam-forming using an iE33 ultrasound system (Philips Medical Systems, Bothell, WA, USA), equipped with an RF-interface and a pediatric X7-2 matrix array transducer (2-7 MHz). RF-data were sampled at 16 MHz and transmitted to an external hard disk. The data were band pass filtered (FIR least squares filter [2-5 MHz]) to prevent disturbance by clutter and noise from frequencies outside the frequency band of the transducer. For constructing echograms, the data were amplitude demodulated using the Hilbert transform method.

6.2.1 Temporal cross-correlation of the radio frequency signal

As velocity of the blood flow is expected to be higher than velocity of the surrounding myocardial tissue, RF-signals will correlate less for fast moving blood than for myocardial tissue. Temporal correlations might thus be used as a feature for distinguishing between blood and the heart muscle. For 3D strain imaging purposes, the cross-correlation function (CCF) of 2D windows of RF-data was calculated [Chen et al. 2005; Lopata et al. 2007] using two subsequent full volumes. The peak of the cross-correlation function reveals the displacement of a 2D segment of RF-data in the next time frame in 2D space. A 2D coarse-to-fine displacement estimation algorithm was expanded into an iterative semi-3D approach. 2D reference windows of 50 x 5 (axial x lateral) samples within the axial-azimuth plane were matched with a search area of 150 x 11 samples in the next frame. Both the CCF and the axial and lateral displacements were estimated. Next, the axial displacements were used as an offset to estimate axial and elevational displacements and the CCF in the axial-elevational plane. Hence, the displacements in three orthogonal directions in 3D space were assessed. This semi-3D approach was preferred over a full-3D approach since the iterative 2D cross-correlation calculation imposed a lower computational load and no significant difference in performance and precision was found between both methods [Lopata et al. 2007]. The maximum cross-correlation (MCC) values were found for each window. Window overlap in the axial direction was 75%, resulting in a cross-correlation image of 147 x 62 x 56 samples. This corresponds to a pixel resolution of $600\mu m$ in the axial direction.

6.2.2 3D Adaptive filtering

Besides the maximum cross-correlation values, adaptive filtering was used as a more conventional method to optimize the distinction between blood and myocardium. 3D Adaptive Mean Squares filtering of the amplitude demodulated data was applied in the spatial domain. The 3D filter kernel size was related to image speckle size and contained approximately 5 x 2 x 2 (axial x lateral x elevational) speckles. The AMS filter incorporates knowledge about speckle statistics of blood and myocardium in an adaptive manner: homogeneous regions are filtered strongly, i.e. speckle noise is reduced, whereas in inhomogeneous regions the degree of filtering is low, such that transitions between blood and myocardium are preserved. The AMS filter has been proven to be effective for segmentation of echocardiographic images when using gradient based deformable models (Chapter 3).

6.2.3 Deformable model

A deformable simplex mesh model [Delingette 1999] was used for segmentation of the left ventricle. In this model, each vertex of the mesh $p_i = (x_i, y_i, z_i)$ is

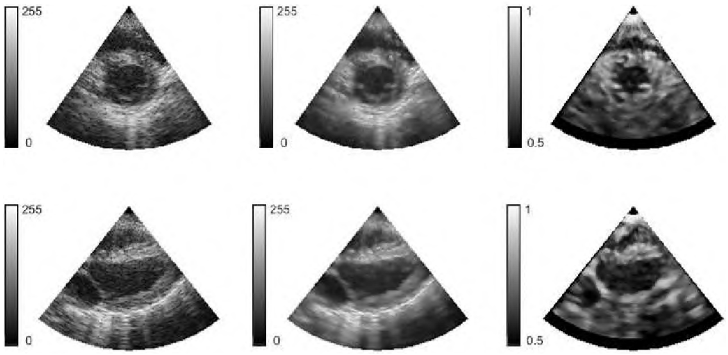

Figure 6.1: Short *(upper panel)* and long *(lower panel)* axis views from a full volume dataset for the two external force types of the deformable model. *Left:* demodulated RF-data. *Middle:* data after adaptive filtering. *Right:* maximum cross correlation values.

displaced in an iterative manner according to the discrete approximation of the Newtonian law of motion:

$$p_{i+1} = p_i + \alpha F_{int} + F_{ext} \tag{6.1}$$

F_{ext} is an external force derived from the image data that steers the simplex mesh onto boundary structures. In this study, F_{ext} consisted of an adaptive filtering based component and the newly defined maximum cross-correlation component:

$$F_{ext} = \beta F_{grad_{AMS}} + \delta F_{grad_{MCC}} + \kappa F_{speed_{AMS}} + \lambda F_{speed_{MCC}} \tag{6.2}$$

Both AMS and MCC images were used to compute gradient and speed forces (see [Böttger et al. 2007], Chapter 4) for a general description of gradient and speed forces). F_{int} is a regularization force and controls the smoothness of the surface [Delingette 1999]. Weighting factors $\alpha, \beta, \delta, \kappa$ and λ were used to balance the different forces. Whereas adaptive filtering and computation of the cross-correlation was performed by processing the data along the scan-lines, computation of the external and internal forces, as well as the deformation of the simplex mesh was performed on the data in scan-converted (i.e., sector) format. Initialization of the mesh was done by interactive placement of a small spherical mesh in the center of the left ventricle.

Figure 6.1 shows long and short axis views from a full volume dataset for the two external force types of the model. In this figure, the original demodulated RF-data, the data after adaptive filtering and the cross-correlation image are shown. Image data were visualized in scan-converted format, in order to obtain realistic anatomical views.

6.2.4 Evaluation

The method was evaluated by comparing left ventricular cavity contours as obtained from the segmentation method with contours obtained from manual segmentation. Papillary muscles were excluded from the left ventricular cavity. Contours were extracted from the 3D volume segmented by the deformable model and compared to manual segmentation for long axis (LAX) view and three short axis (SAX) cross sections (at base, mid and apical level). Three different force types were compared: using AMS force only (original model, $\beta \neq 0, \kappa \neq 0, \delta = \lambda = 0$), using cross-correlation force only ($\beta = \kappa = 0, \delta \neq 0, \lambda \neq 0$), and the combined model ($\beta = \kappa = \delta = \lambda \neq 0$). The mismatch ratio based on the Dice coefficient was computed for all three force types to the express dissimilarity between manual (Ref) and automatic segmentation (Seg):

$$Mismatch_{Dice} = 1 - \frac{2(Ref \cap Seg)}{(Ref + Seg)} \tag{6.3}$$

6.3 Results

3D segmentation of the left ventricle was performed in four full volume images obtained from four healthy children (6, 7, 8 and 9 years old) in the end systolic phase of the heart cycle. For each dataset, the three different force types (AMS, MCC and a combination of both AMS and MCC) were tested using the deformable model. For each dataset, the same initial position of the mesh in the center of the left ventricle was used for all three segmentation methods.

Figure 6.1 illustrates that the contrast between blood and the myocardium is higher for the cross-correlation values than for the adaptive filtered data. Also endocardial regions with low echogenicity seem to have better contrast between blood and myocardium in the correlation image. Figure 6.2 shows the effect of the maximum cross-correlation on the segmentation results. In this figure, segmentations of the endocardial surface in the long axis view (LAX) and three short axis views (SAX base, mid and apex) are given for an illustrative example. It can be clearly seen that for this dataset, segmentation exclusively based on the AMS data leads to overestimation of the dimension of the ventricular cavity at the apical side of the long axis view (compare mismatch ratios in Table 6.1, column 2, LAX). Segmentation solely based on maximum cross-correlation leads to incorrect segmentation and underestimation of the endocardial dimension, see middle panel. Combination of AMS and cross-correlation force (lower panel) improves the segmentation and results in correct dimensions of the left ventricle. Also in the short axis views, combination of AMS and cross-correlation results in better segmentation of the endocardial surface. Corresponding mismatch ratios for this dataset (see Table 6.1) revealed that the segmentation results improved (i.e., the mismatch ratio decreased) when the cross-correlation force was added to the AMS force. Using the cross-correlation force on its own resulted in underestimation of

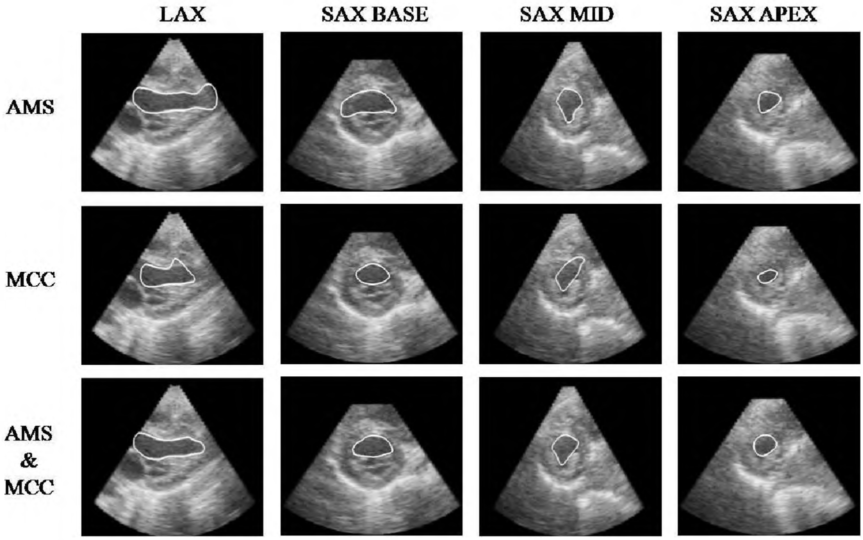

Figure 6.2: Segmentation results for three settings of the deformable model for one dataset. Long and short axis views overlaid with contours of the segmented endocardial surface using AMS *(upper)*, maximum cross correlation (MCC) *(middle)* and an equally weighed combination of AMS and MCC force *(lower)*.

Table 6.1: Mismatch ratios for segmentation by adaptive mean squares (AMS), maximum cross-correlation (MCC) and AMS/MCC combined methods. Long axis (LAX) view and short axis (SAX) view images for the data set of Fig. 6.2.

Mismatch ratios	LAX	SAX Base	SAX Mid	SAX Apex
AMS	0.23	0.25	0.23	0.13
MCC	0.22	0.14	0.16	0.27
AMS & MCC	0.12	0.14	0.15	0.12

the endocardial surface, whereas a segmentation that only used the AMS filtered data resulted in crossing boundaries in the low contrast regions. Table 6.2 summarizes the mismatch ratios for the four different views (LAX, SAX base, mid and apex), averaged over all four datasets. According to this table, the combination of AMS and MCC force yielded the most accurate segmentation results for all views.

To demonstrate the effect of the MCC force, the gray levels of manually drawn myocardial and blood pool regions were compared for AMS and MCC values. Figure 6.3 compares AMS against MCC values for myocardial regions with high and low echogenicity (apical), and a blood pool region, respectively. It can be seen

Table 6.2: Average mismatch ratios (n = 4) for segmentation by adaptive mean squares (AMS), maximum cross-correlation (MCC) and AMS/MCC combined methods for long axis (LAX) view and short axis (SAX) view images.

Average mismatch ratios	LAX	SAX Base	SAX Mid	SAX Apex
AMS	0.18	0.16	0.22	0.15
MCC	0.17	0.14	0.17	0.26
AMS & MCC	0.11	0.12	0.14	0.13

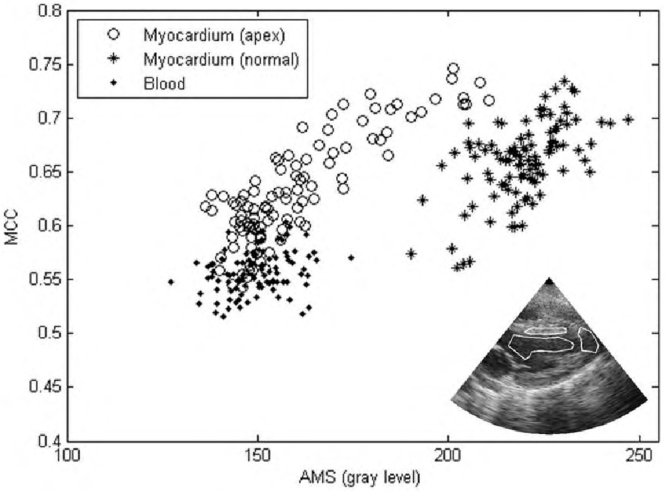

Figure 6.3: Comparison between AMS *(horizontal axis)*and MCC *(vertical axis)* values for high and low contrast myocardial regions vs. blood pool region. Manually drawn regions are shown in the echogram *(bottom right)*.

from this figure that the AMS force is highly distinctive in the case of blood vs. myocardial tissue with high echogenicity. However, for low contrast regions of the heart muscle, for example near the apex, blood and myocardium can no longer be classified by using the AMS values, whereas in this case, MCC still can be used to distinguish blood form myocardial tissue.

6.4 Discussion and Conclusion

In this study, we developed a method that enables segmentation of anatomical structures in the heart of children by incorporating temporal information in the model. According to these preliminary results, maximum temporal cross-correlation values, based on the RF-signal, have additional value for the segmentation of cardiac tissue. Since correlation can still be high in areas with low echogenicity, inclusion of this parameter in the deformable simplex model as an extra feature facilitates segmentation in regions where contrast between blood pool and endocardial border is too low to perform gray-level based segmentation. This is illustrated by the proper segmentation of the apical region in Fig. 6.2. The complimentary character of the MCC and AMS is demonstrated in Fig. 6.3. In high quality images (without low contrast regions), the AMS force already yielded adequate segmentation results and the cross-correlation force did have no additional value as indicated by the mismatch ratios for AMS and the combination of MCC and AMS in the apical short axis view (Table 6.1).

A deformable model that only uses the cross-correlation force underestimated the blood pool region. This is most likely caused by the larger windows used in the computation of correlation values and because of the blood close to the heart wall 'adhering' to the moving heart muscle, leading to a higher correlation value, i.e., lower MCC contrast, in blood regions close to the endocardial border.

Presently, the method has been tested in the end-systolic phase where deformation of the heart is small, because with the current echo systems, the frame rate of full volume imaging is still limited in terms of the accuracy of cross-correlation values throughout the entire cardiac cycle. For example, the cross-correlation based model could be used in the end-systolic and end-diastolic phase as a more robust initialization for segmentation of the other frames in the cardiac cycle. In future, the method will be extended to more frames during the cardiac cycle.

Acknowledgements.

This work is supported by the Dutch Technology Foundation (STW), project 06466 and Philips Medical Systems. The authors would like to thank Bob Rijk for his assistance with the echographic image acquisitions.

7

AUTOMATED 3D SEGMENTATION IN ECHOCARDIOGRAPHIC IMAGES USING 3D TEMPORAL CORRELATION

Based on: M. M. Nillesen, R. G. Lopata, H. J. Huisman, J. M. Thijssen, L. Kapusta, and C. L. de Korte. Correlation Based 3-D Segmentation of Echocardiographic Images using Radio Frequency Data. *submitted*.

7

Abstract

Clinical diagnosis of heart disease might be substantially supported by automated segmentation of the myocardium in 3D echographic images. Because of the poor echogenicity contrast between blood and myocardial tissue in some regions and the inherent speckle noise, automated analysis of these images is challenging. *A priori* knowledge on the shape of the heart cannot always be relied on, e.g., in children with congenital heart disease, segmentation should be based on the echo features solely. The objective of this study was to investigate the merit of using temporal cross-correlation of radio frequency (RF) data for automated segmentation of 3D echocardiographic images.

Maximum temporal cross-correlation (MCC) values were determined locally from the RF-data using an iterative 3D technique. MCC values as well as a combination of MCC values and adaptive filtered, demodulated RF-data were used as an additional, external force in a deformable model approach to segment the endocardial surface and were tested against manually segmented surfaces. Results on 3D full volume images (Philips, iE33) of 10 healthy children demonstrate that incorporation of MCC improves the segmentation results significantly.

7.1 Introduction

Ultrasound is a reliable and fast imaging modality that is pre-eminent in cardiac imaging of children because of its non-invasiveness and high temporal resolution. The introduction of real-time 3D echographic imaging techniques has been a major step forward for quantitative analysis of the heart as these techniques provide rich information about the whole structure and 3D motion of the heart. 3D echocardiography enables the estimation of clinically important parameters such as cardiac output and ejection fraction without the necessity of making 2D geometrical assumptions. These geometrical assumptions generally include a simplified shape of the left ventricle which may lead to inaccurate estimation of the ventricular function [Gopal et al. 1995; Jacobs et al. 2006]. 3D ultrasound imaging might also facilitate simultaneous estimation of strain in radial, circumferential and longitudinal direction in the heart muscle. Furthermore, inaccurate strain estimates due to out of plane motion [Kallel and Ophir 1997; Konofagou and Ophir 2000] can be prevented.

The availability of 3D echocardiography has also boosted the urge for automated segmentation methods since manual segmentation of 3D ultrasound image sequences is very time-consuming. Moreover, manual segmentation by an expert is subject to inter-and intra-expert variability. Many approaches for segmenting the endocardial wall in adult echocardiographic images have been proposed. An overview can be found in Noble and Boukerroui [2006].

The inherent speckle noise from randomly backscattered echoes and the poor echogenicity contrast between blood and myocardium in some regions impose strong demands on the segmentation algorithm. If the orientation of the muscle fibers is mainly parallel to the propagation direction of the ultrasound beam, myocardial echogenicity is reduced to within the range of blood echogenicity. Automatic segmentation purely based on differences in echogenicity will lead to erroneous segmentation in these low echogenicity regions as the contrast between blood and myocardial tissue is absent. To overcome segmentation errors in these regions, methods using shape and appearance models have been proposed [Bosch et al. 2002; Hansegard et al. 2007]. These models incorporate knowledge about the shape and appearance of, for example, the left ventricle by using an average shape and appearance model of the adult heart. These methods rely on implicit knowledge that is also used by expert cardiologists during manual segmentation and are successful in normal adult heart geometries in standardized (apical) views. However, echocardiography in children often aims at detection of congenital deformities of the heart. The use of a priori knowledge about the average shape of the ventricle may lead to incorrect segmentation in these images.

Segmentation in pediatric echocardiographic images faces some additional difficulties. Due to the relatively small intercostal spaces, image quality might be affected negatively by the ribs, causing shadowing and clutter artifacts. Compared to adults, the position of the heart within the thorax is different in such a way that in most 3D apical images in young children the lateral wall (compare the standard 2D two-chamber view) is difficult to visualize. Three-dimensional transthoracic short-axis/long axis views lead to much better image quality as the largest part of the muscle fibers is now perpendicular to the ultrasound beam. However, in this different view it is challenging to visualize the entire left ventricle and often the apex is missing or has a very low echogenicity. Furthermore, most commercial segmentation methods require a standardized apical view and no accurate segmentation is obtained in this different viewing angle with these methods.

In order to obtain more accurate segmentations in problematic low contrast regions without the necessity of making a priori assumptions on shape/appearance and viewing angle, the addition of temporal information using cross-correlation techniques might be helpful. These techniques build on the underlying principle that echographic data of two successive time frames will correlate less for fast moving blood than for the myocardial tissue. For the analysis of echocardiographic images, an expert cardiologist mentally incorporates the movement of the heart throughout the cardiac cycle to determine the exact geometry of the heart and uses the temporal coherence of structures to resolve ambiguities. In this study, we propose the use of temporal cross-correlation techniques that utilize the rich phase information available in the radio frequency (RF) signal.

In the field of ultrasound segmentation, most methods are based on using conventional B-mode images (amongst others, Angelini et al. [2001]; Corsi et al. [2002]; Gerard et al. [2002]; Lin et al. [2003]; van Stralen et al. [2005]), whereas only a few studies are dedicated to segmentation based on the radio RF-data. Davignon et al. [2005] used statistical parameters, derived from the envelope of the RF-data, representative of the scattering conditions in the tissue in a multi-parametric segmentation process and they evaluated these parameters in simulated ultrasound data. Boukerroui et al. [2002] computed the mean central frequency (MCF) and integrated backscatter (IBS) from the local frequency spectra of the RF-signal and used these parameters in a multi-parametric and multi-resolution segmentation algorithm. Dydenko et al. [2003] proposed the use of spectral autoregressive parameters and velocity-based parameters and tested these on 2D simulated and cardiac RF-data. Gerrits et al. [2007] used the temporal decorrelation of Doppler RF-signals for 3D region based-segmentation of the left ventricle. Yan et al. [2007] investigated several RF-derived parameters as the IBS, the MCF and the maximum cross-correlation coefficient (MCC). In the latter study, segmentation based on parametric images obtained from the MCC using phase sensitive speckle tracking was promising.

This study aims at three-dimensional (3D) automated segmentation of the endocardial surface in 3D pediatric echocardiographic images. We propose the use of temporal cross-correlation values of subsequently acquired 3D volumes. Cross-correlation values were derived from an iterative coarse-to-fine displacement algorithm that was originally developed for strain estimation. These values were included as external force in a deformable model. The effect of incorporating the cross-correlation values in the segmentation method has been investigated by evaluating the obtained results.

7.2 Materials and Methods

7.2.1 Echographic data

Echocardiographic image sequences of the left ventricle were obtained in ten healthy children (6-15 years old). The protocol was approved by the local ethics

Table 7.1: Settings and window dimensions used in the coarse-to-fine MCC estimation algorithm.

	Coarse (3D MCC)	Middle (3D MCC)	Fine (3D MCC)	Fine (1D MCC)
Envelope/RF-data	Envelope	Envelope	RF-data	RF-data
Window size CCF K_w, frame t (ax x lat x elev)	5 mm x 11 lines x 11 lines	2.5 mm x 5 lines x 5 lines	2.5 mm x 5 lines x 5 lines	2.5 mm
τ $(\tau_{ax} x \tau_{lat} x \tau_{elev})$	7 mm x 5 lines x 5 lines	0.6 mm x 3 lines x 3 lines	0.6 mm x 3 lines x 3 lines	0.25 mm
Search window size CCF, frame t+1	19 mm x 21 lines x 21 lines	3.7 mm x 11 lines x 11 lines	3.7 mm x 11 lines x 11 lines	3 mm
Median filter displacement estimates	11 mm x 7 lines x 7 lines	8 mm x 7 lines x 7 lines	8 mm x 7 lines x 7 lines	None
Median filter MCC estimates	None	None	None	4.5 mm x 3 lines x 3 lines

committee and both parents and children gave their informed consent. ECG-gated, transthoracic full volume image sequences (3D + t) were obtained in long/short axis views. All children where in sinus rhythm (79 ± 12.6 (mean ±SD) beats per minute) and the volume rate varied between 41 and 56 Hz, depending on the image depth. RF-data were acquired directly after receive beam forming using an iE33 ultrasound system (Philips Medical Systems, Bothell, WA, USA), equipped with an RF-interface and a pediatric X7-2 matrix array transducer (2-7 MHz). RF-data were sampled at 16 MHz and transmitted to an external hard disk. The data were band-pass filtered to prevent disturbance by clutter and noise from frequencies outside the frequency band of the transducer. The data were amplitude demodulated using the Hilbert transform method and log-compressed for visualizing the echograms. Since the frame rate of the used echo system for full volume imaging is still limited, a cardiac phase (end-systole) with low deformation rate of the heart muscle was chosen for evaluation and validation of the segmentation method (see paragraph on cross-correlation techniques below).

7.2.2 Maximum cross-correlation computation

Since the blood flow velocity in the ventricles is predominantly higher than the velocity of the surrounding myocardial tissue, temporal correlations between successive ultrasound volumes might be used as a feature to distinguish between blood and myocardial tissue. For 3D strain imaging purposes, the cross-correlation function (CCF) of 3D windows of RF-data was calculated [Lopata et al. 2007; Chen et al. 2005]. We used a 3D coarse-to-fine displacement estimation algorithm [Lopata et al. 2007] that was based on an earlier developed 2D algorithm [Lopata

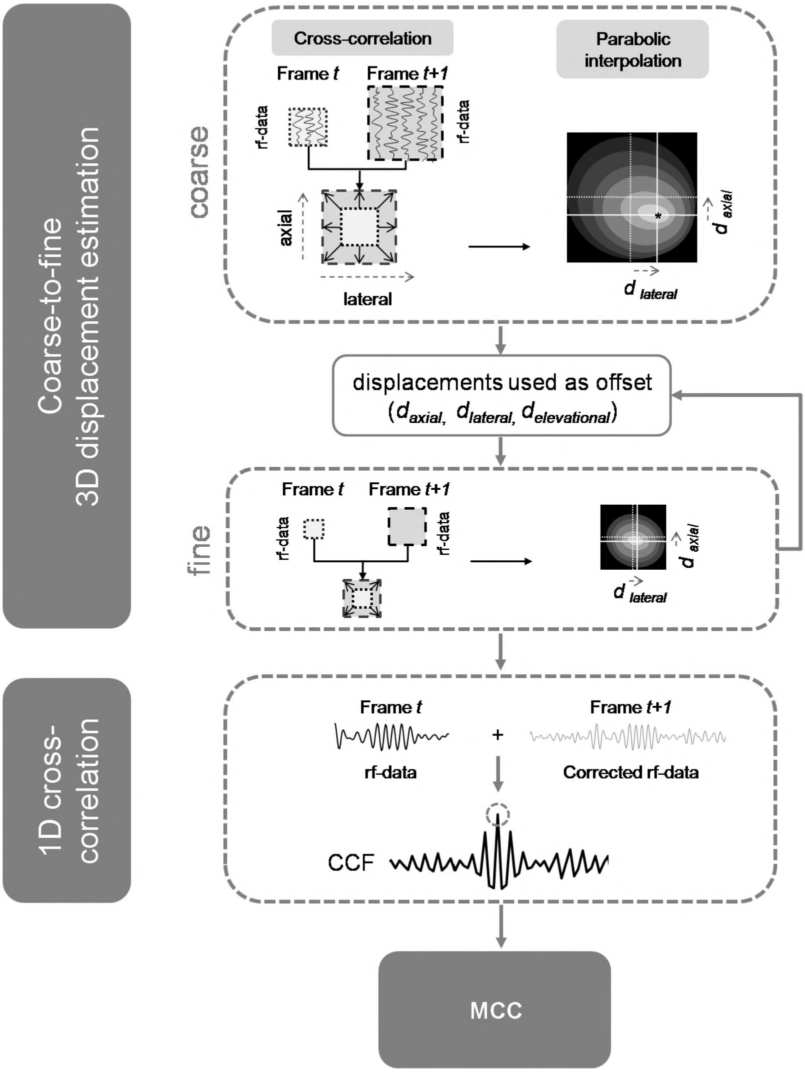

Figure 7.1: Schematic overview of the maximum cross-correlation computation method using a coarse-to-fine displacement algorithm. Three dimensional windows of data are cross-correlated between two consecutive echo volumes. Starting with a coarse window the maximum of the cross-correlation function yields global displacement estimates. These (coarse) displacement estimates are used iteratively as an offset to compute cross-correlations and displacement estimates at a finer scale. In the final step, the maximum of the cross-correlation in 1D is computed to obtain more accurate maximum cross-correlation values. It should be noted that in this schematic overview all 3D computations are depicted in 2D for clearness' sake.

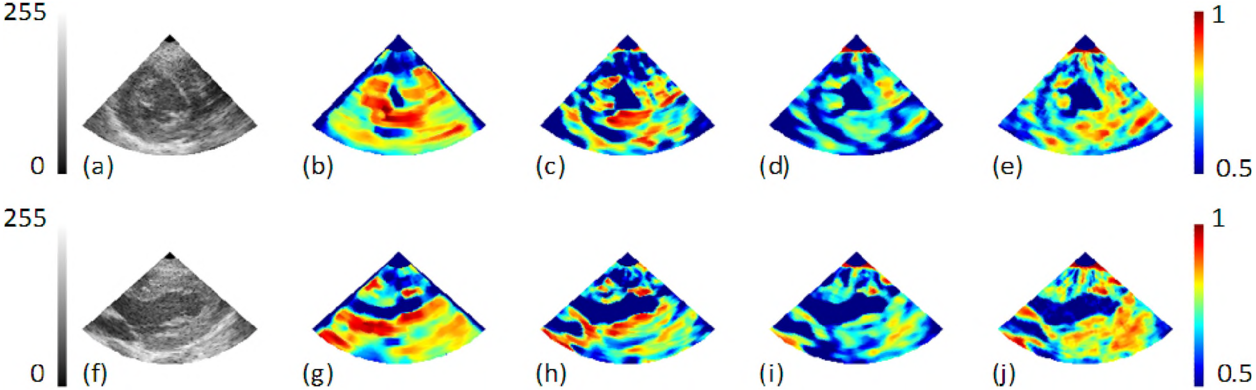

Figure 7.2: Maximum cross-correlation (MCC) images for the four iteration steps as described by the iterative 3D cross-correlation refinement algorithm. *From left to right:* Envelope data (log-compressed demodulated RF data, (a), (f)) and MCC values (median filtered) for iteration step 1 to 4: (b)-(e) (short axis view) and (g)-(j) (long axis view). The 2D planes shown are selected from a 3D full volume data set.

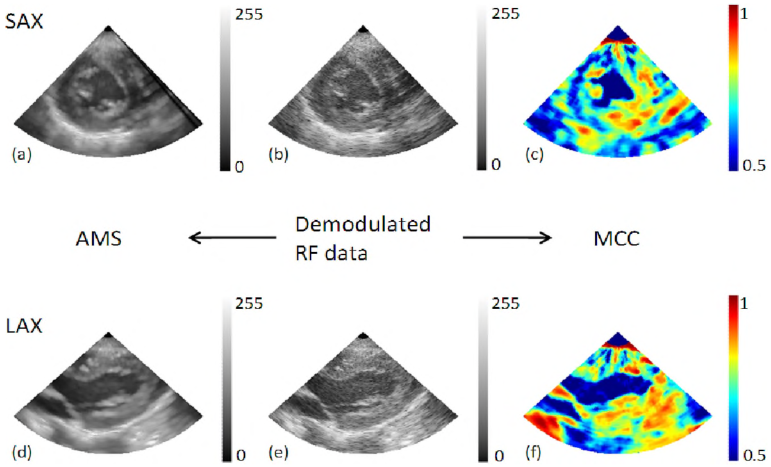

Figure 7.3: Short *(upper panel, a-c)* and long *(lower panel, d-f)* axis views from a full volume dataset. The demodulated RF-data *(b,e)* is used to compute the adaptive filtered data *(a,d)* and the maximum cross-correlation values *(c,f)*. Both AMS and MCC values are used as external force in the deformable model.

et al. 2009] to estimate axial, lateral and elevational displacements iteratively. For strain estimation, the position of the peak of the cross-correlation function is used since this position corresponds to the displacement of the tissue. In this study, we used the magnitude of the peak, i.e., the maximum of the cross-correlation function (MCC) as driving force for the segmentation model.

Three-dimensional windows were cross-correlated for two subsequent time frames and the MCC was determined. The 3D normalized CCF for the two successive RF-data frames I_t and I_{t+1} was defined as:

$$CCF(w,t,\tau) = \frac{\sum_{w \in K_w} \left[I_t(w) - \bar{I}_t\right] \left[I_{t+1}(w+\tau) - \bar{I}_{t+1}\right]}{\sqrt{\sum_{w \in K_w} \left[I_t(w) - \bar{I}_t\right]^2 \left[I_{t+1}(w+\tau) - \bar{I}_{t+1}\right]^2}} \tag{7.1}$$

where $w = (w_{ax}, w_{lat}, w_{elev})$ denotes the axial, lateral and elevational index and $\tau = (\tau_{ax}, \tau_{lat}, \tau_{elev})$ denote the spatial shift between frames I_t and I_{t+1}. The maximum absolute shift τ was limited, hereby limiting the maximum axial and lateral and elevational displacements that could be measured. K_w defines a symmetrical window centered around w and $\bar{I}_t$ and $\bar{I}_{t+1}$ indicate the mean values for the specified windows for I_t and I_{t+1} used in the CCF computation. Table 7.1 provides a detailed overview of all window dimensions used in the CCF computations. The peak of the cross-correlation function within the search window revealed the displacement estimate $\hat{d}_{iter} = (\hat{d}_{ax}, \hat{d}_{lat}, \hat{d}_{elev})$ of a 3D segment of RF-data in the next time frame in 3D space:

$$\hat{d}_{iter}(w,t) = \arg\max_{\tau} CCF(w,t,\tau) \tag{7.2}$$

The displacement estimation $\hat{d}_{iter}$ was further improved by parabolic interpolation of the cross-correlation function around the peak (Fig. 7.1).

Iterative cross-correlation refinement

Now we have obtained an initial displacement estimate, this displacement can be compensated for in the CCF computation in an iterative manner. By doing this, the cross-correlation values can be optimized and further refined. The displacement field $\hat{d}$ estimated in the previous iteration was used as an offset for the CCF computation:

$$CCF_{iter}(w,t,\tau,\hat{d}_{iter-1}) = \frac{\sum_{w\in K_w} \left[I_t(w) - \bar{I}_t\right] \left[I_{t+1}(w+\tau+\hat{d}_{iter-1}) - \bar{I}_{t+1}\right]}{\sqrt{\sum_{w\in K_w} \left[I_t(w) - \bar{I}_t\right]^2 \left[I_{t+1}(w+\tau+\hat{d}_{iter-1}) - \bar{I}_{t+1}\right]^2}} \tag{7.3}$$

$$\hat{d}_{iter}(w,t) = \arg\max_{\tau} CCF_{iter}(w,t,\tau,\hat{d}_{iter-1}) \tag{7.4}$$

The iterative displacement estimation method was applied using a coarse-to-fine algorithm, as illustrated by Fig. 7.1 and 7.2. In the first iteration, the envelope data (i.e., demodulated RF-data using the Hilbert transform) were cross-correlated using large windows (coarse) to obtain a coarse displacement field. In the second iteration, the window size was decreased (fine), enabling more precise displacement estimates at a higher resolution. The third iteration used the RF-data at a fine scale enabling even more accurate displacement estimations because of the use of high-resolution phase information [Lopata et al. 2009]. Window sizes for the successive iterations are partly based on the optimal settings for strain estimation [Varghese and Ophir 1997] and detailed information on window sizes is given in Table 7.1. All displacement estimates were smoothed using a median filter. As a final step (iteration 4), the peak of the one-dimensional CCF in the axial direction (based on RF-data) was estimated. After compensation for the 3D local displacement field using 3D cross-correlations in the first three iterations, we used the 1D cross-correlation in the fourth iteration since this is a better representation of the actual correlation between the two consecutive volumes. Therefore, more precise and higher cross-correlation values are achieved using the 1D CCF:

$$CCF_{1D}(w,t,\tau_{ax},\hat{d}) = \frac{\sum_{w_{ax}\in K_{w_{ax}}} \left[I_t(w) - \bar{I}_t\right] \left[I_{t+1}(w_{ax}+\tau_{ax}+\hat{d}_{ax}, w_{lat}+\hat{d}_{lat}, w_{elev}+\hat{d}_{elev}) - \bar{I}_{t+1}\right]}{\sqrt{\sum_{w_{ax}\in K_{w_{ax}}} \left[I_t(w) - \bar{I}_t\right]^2 \left[I_{t+1}(w_{ax}+\tau_{ax}+\hat{d}_{ax}, w_{lat}+\hat{d}_{lat}, w_{elev}+\hat{d}_{elev}) - \bar{I}_{t+1}\right]^2}} \tag{7.5}$$

where $K_{w_{ax}}$ defines a symmetrical axial window centered around w_{ax}. The maximal absolute axial shift τ_{ax} was limited between -5 and +5 samples. The maximum of this 1D CCF was defined as the MCC parameter that was used as a novel feature in the segmentation process:

$$MCC(w,t) = \max_{\tau_{ax}} CCF_{1D}(w,t,\tau_{ax},\hat{d}) \tag{7.6}$$

Finally, the MCC values were median filtered. Figure 7.2 illustrates the iterative cross-correlation refinement algorithm by showing MCC values for the four iteration steps in short and long axis views of the left ventricle.

7.2.3 3D Adaptive filtering

Besides from estimation of the MCC values, 3D adaptive filtering was used as a more conventional method to optimize the distinction between blood and heart muscle. 3D Adaptive Mean Squares (AMS) filtering of the amplitude demodulated RF-data was applied in the spatial domain (Chapter 3). The window size of the 3D filter was related to image speckle size and contained approximately 5 x 2 x 2 (axial x lateral x elevational) speckles. Knowledge about speckle statistics (Chapter 2) of blood and myocardium are incorporated in an adaptive manner: homogeneous regions are filtered strongly, i.e., speckle noise is reduced, whereas in inhomogeneous regions the degree of filtering is low, such that transitions between blood and myocardial tissue are preserved. The AMS filter has been proven to enhance the difference between echo-levels originating from blood and myocardial wall (Chapter 3), and to be effective for segmentation of 3D echocardiographic images when using gradient based deformable models (Chapter 4).

7.2.4 Deformable model

A gradient-based deformable simplex mesh model [Delingette 1999] was used for segmentation of the left ventricle. A simplex mesh consists of a set of vertices that forms a discrete non-parametric representation of a surface in $\mathbb{R}^3$. In this model, each vertex of the mesh $p_i = (x_i, y_i, z_i)$ is displaced in an iterative manner according to the discrete approximation of the Newtonian law of motion:

$$p_{i+1} = p_i + \alpha F_{int} + F_{ext} \tag{7.7}$$

F_{int} is a regularization force and controls the smoothness of the surface [Delingette 1999]. F_{ext} is an external force derived from the image data that steers the simplex mesh onto boundary structures. In this study, F_{ext} consists of an adaptive filtering based component (AMS) and the newly defined maximum cross-correlation component (MCC):

$$F_{ext} = \beta F_{grad_{AMS}} + \delta F_{grad_{MCC}} + \kappa F_{speed_{AMS}} + \lambda F_{speed_{MCC}} \tag{7.8}$$

Both AMS and MCC values were used to compute gradient and speed forces. The gradient force F_{grad} is defined as:

$$F_{grad_{force}}(p_i) = \nabla \frac{1}{1 + \exp - \frac{|\nabla G_\sigma * I_{force}(x_i, y_i, z_i)| - \zeta_{grad}}{\eta_{grad}}} \tag{7.9}$$

where I_{force} stands for image intensity (echo level) of either the AMS image (force = AMS) or the MCC image (force = MCC). The parameters ζ_{grad} and η_{grad} are used to scale the gradient magnitude to the interval [0, 1] by sigmoidal intensity mapping and are based on the minimum and average gradient magnitude value [Ibanez et al. 2003]. Gaussian smoothing (G_σ) with a relatively small σ (0.5 mm) is applied to increase the width of the attraction potential and to smooth undesired small gradients inside the left ventricular cavity.

F_{speed} is a complimentary, inflating force, into the vertex normal direction and is defined as [Böttger et al. 2007]:

$$F_{speed_{force}}(p_i) = \frac{1}{1 + \exp - \frac{|\nabla G_\sigma * I_{force}(x_i, y_i, z_i)| - \zeta_{speed}}{\eta_{speed}}} \tag{7.10}$$

The parameters ζ_{speed} and η_{speed} are chosen such that F_{speed} has high values in regions with no gradient information and has low values at boundaries and lies between 0 and 1, in order to reduce the need for close-to-boundary initialization of the mesh.

Weighting factors α, β, δ, κ and λ were used to balance the different forces. Whereas adaptive filtering and computation of the cross-correlation was performed by processing the data along the scan-lines, computation of the external and internal forces, as well as the deformation of the simplex mesh was performed on the data in scan-converted (i.e., sector) format. Initialization of the mesh was done by interactive placement of a small spherical mesh in the center of the left ventricle. Figure 7.3 shows long and short axis views from a full volume dataset for the two external force types of the model. In this figure, the original demodulated RF-data, the data after adaptive filtering and the maximum cross-correlation image are shown. Image data were visualized in scan-converted format, in order to obtain realistic anatomical views.

7.2.5 Evaluation

The method was evaluated by comparing left ventricular cavity contours as obtained from the segmentation method with contours obtained from manual segmentation. Segmentation results of three different force types were compared: using AMS force only (original model, β and $\kappa \neq 0$, $\delta = \lambda = 0$), using cross-correlation force only ($\beta = \kappa = 0$, δ and $\lambda \neq 0$), and the combined model (β and

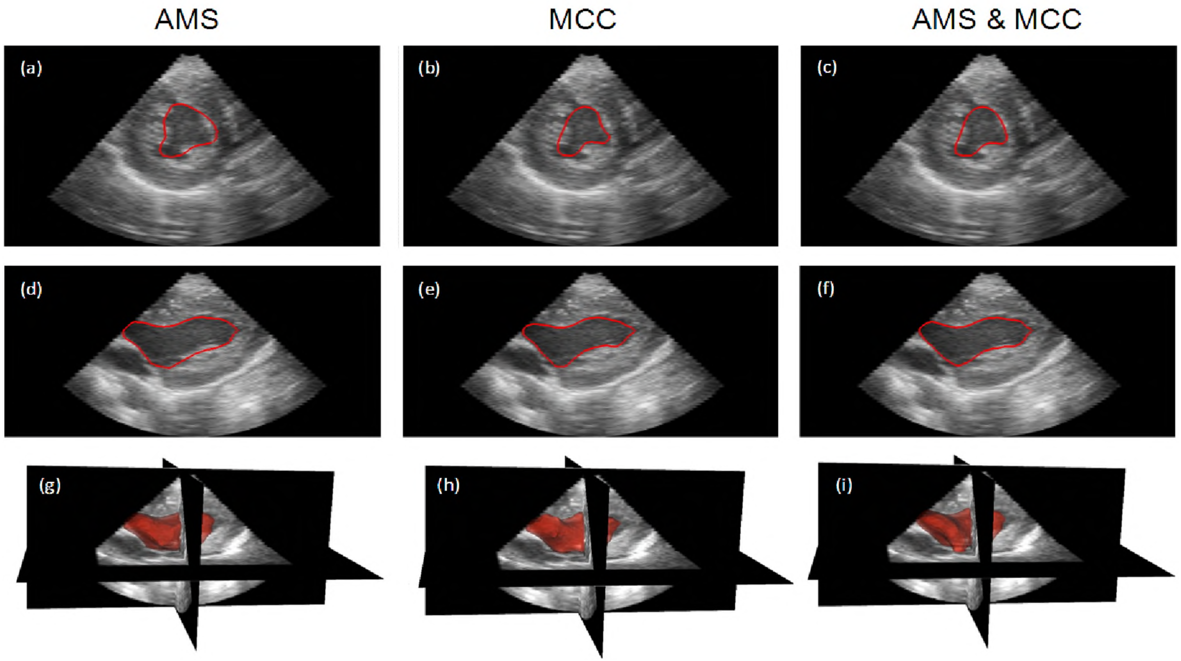

Figure 7.4: Segmentation results for a full volume dataset. Short axis *(upper panel, a-c)*, long axis *(middle panel, d-f)* and 3D views *(lower panel, g-i)* are shown for the three different settings of the deformable model. From left to right: echographic data overlaid with contours of the segmented endocardial surface using 1) AMS, 2) maximum cross-correlation (MCC) and 3) an equally weighed combination of AMS and MCC force.

κ and δ and $\lambda \neq 0$). In the combined model, AMS and MCC are equally weighed forces. For each dataset, the same initial position of the mesh in the center of the left ventricle was used for all three segmentation methods. Contours were extracted from the 3D volume segmented by the deformable model and compared to manual segmentation for long axis (LAX) views and short axis (SAX) cross sections. The endocardial surface was segmented manually by a trained observer for all data sets by drawing 2D contours for each axial-elevational plane (short-axis view). The observer was unaware of the automatically segmented contours. Papillary muscles were excluded from the left ventricular cavity. For each data set, a set of relevant short axis and long axis planes was defined. A plane was considered 'relevant' if it contained (part of) the left ventricle. Planes on the periphery of the left ventricle, where it was not possible to draw reliable contours, were left out. 2D similarity indices were computed for all relevant planes in the axial-lateral (long axis) and axial elevational (short axis) planes. The Dice coefficient [Dice 1945] was computed between manual (Ref) and automatic segmentation (Seg) to express the similarity:

$$SI_{Dice} = \frac{2(\mathrm{Ref} \cap \mathrm{Seg})}{\mathrm{Ref} + \mathrm{Seg}} \tag{7.11}$$

It should be mentioned that this similarity index was applied to 2D contours as well as to 3D volumes. Statistical analysis (Wilcoxon signed rank test) was performed to test whether the 2D SI's for all relevant planes of all data sets were significantly different for the three force types.

7.3 Results

3D segmentation of the left ventricle was performed in full volume images obtained from ten healthy children in the end systolic phase of the heart cycle. Three different force types were tested using the deformable model for each dataset: AMS, MCC and an equally weighed combination of both AMS and MCC.

Figure 7.3 shows characteristic short and long axis views from a full volume dataset for the two external forces of the deformable model. In general the contrast between blood and the myocardium is higher for the maximum cross-correlation values than for the adaptive filtered data. MCC values also seem to yield better contrast between blood and myocardium in low echogenicity regions of the heart muscle, for example in the region where the muscle fibers are parallel to the ultrasound beam (cf. short axis view, compare Fig. 7.3a and 7.3c).

Figure 7.4 shows segmentation results for the three force types, AMS, MCC, and AMS combined with MCC. This figure depicts the scan-converted demodulated RF-data overlaid with contours of the segmented endocardial surface in short axis, long axis views as well as a 3D volume representation.

In order to perform a more thorough evaluation of the influence of the MCC on the segmentation results, 2D and 3D Dice similarity indices (SI's) between automatic and manual segmentation were computed. 2D SI's for one data set

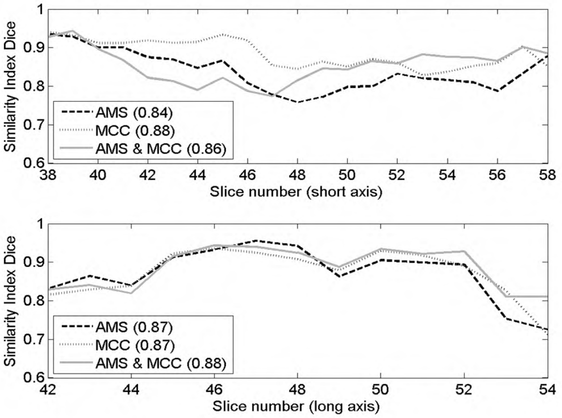

Figure 7.5: Similarity indices (SI) between automated and manual segmentation for the three different force types (AMS *(solid)*, MCC *(dotted)*, AMS & MCC *(dashed)*). 2D SI's for the relevant short axis planes (Fig. 7.4a) and long axis planes (Fig. 7.4b) are shown for a single dataset, cf. Fig. 7.3. Average SI's over all relevant planes are denoted within the brackets.

(cf., Fig. 7.4) are given in Fig. 7.5. Average 2D SI's over all relevant planes are denoted in brackets for all three force types. Table 7.2 summarizes the average 2D similarity indices over all relevant planes of long and short axis views for AMS, MCC and the combination of AMS and MCC. As can be appreciated from this table, the most accurate segmentation was obtained by the combination of AMS and MCC. Especially in the short axis views, in 80% of the cases the combination of AMS and MCC outperforms segmentation based on AMS or MCC alone. In the long axis view, in 60% of the cases the segmentation outcome of the combination is equally or more accurate than segmentation based on AMS alone.

A Wilcoxon signed rank test on the 2D SI's over all relevant planes of all datasets reveals significant improvement for the combination of AMS and MCC compared to segmentation based on AMS alone, as well for short axis views ($n = 269$, $p < 0.001$) as for long axis views ($n = 131$, $p < 0.05$). The combined force also significantly ($p < 0.001$) outperforms segmentation based on the MCC force alone for both short and long axis views.

Furthermore, we compared the entire manually segmented 3D surface with the automatically segmented surface by calculating the 3D similarity index. Results are shown in Table 7.3. The 3D SI shows that compared to the use of the AMS force solely, the use of MCC values is advantageous, either as a force on its own or in combination with the AMS force. It should be noted that also planes that are very difficult to analyze are included within the 3D similarity measure and reference contours might be less reliable for these planes.

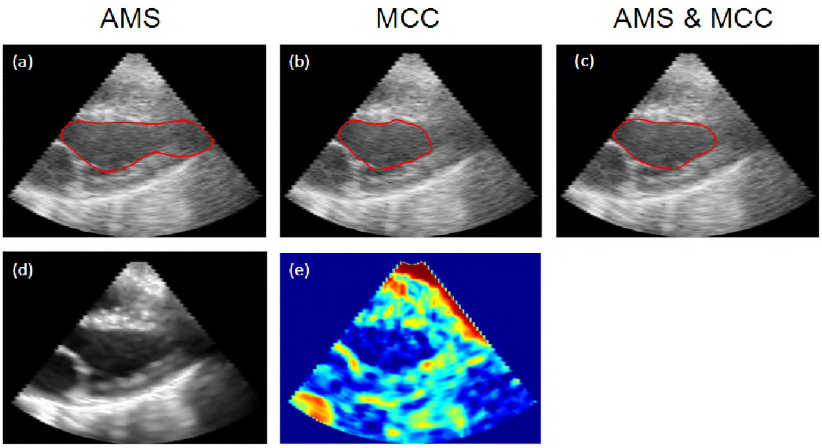

Figure 7.6: Typical example of oversegmentation of the left ventricle when only AMS values are used for segmentation *(a)*. Addition of temporal information by using the MCC leads to improved segmentation in the apical region *(b,c)*. The lower panel shows the AMS *(d)* and MCC *(e)* force to explain the differences in segmentation.

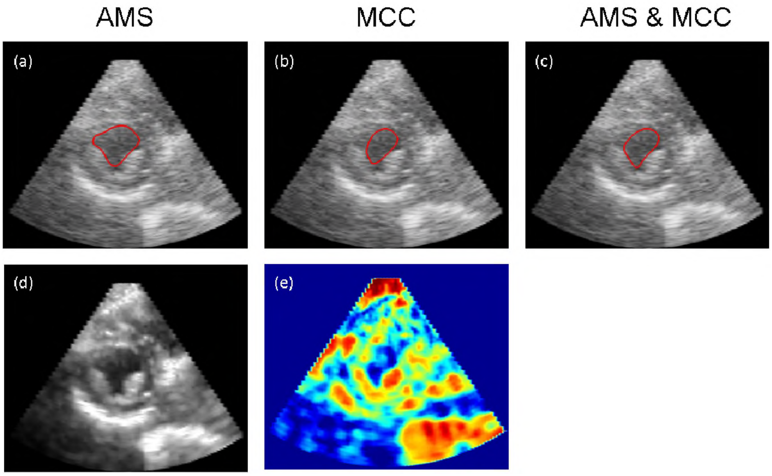

Figure 7.7: Typical example of inaccurate segmentation of the left ventricle when only MCC values are used for segmentation *(a)*. In this case, addition of temporal information by using the MCC *(b)* does not improve the segmentation of the endocardium. The lower panel shows the AMS *(d)* and MCC *(e)* force to explain the differences in segmentation.

Table 7.2: Average 2D similarity indices (Dice) over relevant planes of the long axis and short axis views for the three different force types. For each data set the method with the highest average SI is denoted in bold.

	Average Similarity Index relevant short axis views (SAX) 2D Dice			Average Similarity Index relevant long axis views (LAX) 2D Dice		
Volunteer #	AMS	MCC	AMS & MCC	AMS	MCC	AMS & MCC
1	0.80	0.78	**0.82**	0.71	0.83	**0.85**
2	0.84	**0.88**	0.86	0.87	0.87	**0.88**
3	0.72	0.83	**0.88**	0.75	0.78	**0.83**
4	**0.83**	0.82	0.80	0.77	**0.81**	0.74
5	0.72	0.67	**0.82**	***0.81***	0.67	***0.81***
6	0.82	0.81	**0.83**	**0.83**	0.78	0.82
7	0.83	0.78	**0.86**	0.83	0.78	**0.84**
8	0.80	0.81	**0.83**	**0.79**	0.78	0.78
9	0.88	0.86	**0.89**	**0.86**	0.85	0.84
10	0.78	0.73	**0.79**	0.76	0.77	**0.79**

Table 7.3: Average 3D similarity indices (Dice) for the three different force types. For each data set the method with the highest SI is denoted in bold.

	3D Similarity Index Dice		
Volunteer #	AMS	MCC	AMS & MCC
1	0.65	**0.82**	0.80
2	0.84	**0.88**	0.84
3	0.76	0.79	**0.83**
4	0.73	**0.79**	0.83
5	0.71	0.67	**0.81**
6	***0.80***	0.77	***0.80***
7	0.80	0.76	**0.85**
8	0.75	**0.76**	0.73
9	***0.87***	***0.87***	***0.87***
10	0.72	**0.79**	0.76

In Fig. 7.6 an illustrative example for segmentation of the long axis view is given that shows the additional value of the MCC in low echogenicity regions. It can be clearly seen that for this dataset, segmentation exclusively based on the AMS data resulted in crossing boundaries at the apical side of the long axis view and thus led to overestimation of the left ventricular cavity. Addition of the MCC feature improved the segmentation results and yielded correct dimensions of the left ventricle. It can be concluded from this figure that the MCC (Fig. 7.6e) is still distinctive in the case of blood vs. myocardium in the apical region whereas the AMS filtered data is not (Fig. 7.6d). Similarity indices also reflect improved segmentation when using MCC values (SI AMS: 0.73, SI MCC: 0.87, SI AMS & MCC: 0.88).

Segmentation based on maximum cross-correlation can in some cases lead to incorrect results and underestimation of the endocardial dimension. This is illustrated by the MCC segmentation in Fig. 7.7 and reflected by the corresponding SI values (AMS: 0.91, MCC: 0.75, AMS & MCC: 0.81). Also in the combined force setting (AMS and MCC) the endocardial cavity is still underestimated.

7.4 Discussion and Conclusions

In this study, we investigated a method that enables segmentation of anatomical structures in pediatric hearts by incorporating temporal information. Temporal cross-correlation using the phase information present in the RF-signal was used as an additional feature to distinguish between blood and myocardium. The method was tested on 3D echocardiographic image sequences of ten healthy children and compared to a more conventional method that only uses echo-amplitude information.

Using the 3D iterative displacement estimation algorithm, the maximum temporal cross-correlation values were optimized and refined by each iteration step as illustrated by Fig. 7.2. This optimization procedure was necessary to obtain the deformation of the heart muscle in 3D and, after compensation for this 3D deformation field, to obtain accurate MCC values.

According to the preliminary results, maximum temporal cross-correlation values based on the RF-signal have additional value for the segmentation of cardiac tissue. Since correlation can still be high in (myocardial) regions with low echogenicity (and thus low contrast with blood), inclusion of this parameter in the deformable simplex model as an extra feature in general improves segmentation. Quantitative analysis using 2D image planes reveals that in the majority of cases the combination of the MCC and AMS outperforms segmentation using MCC or AMS only. Especially in the short axis view, the combination is beneficial. This is probably related to the fact that in short axis views the ultrasound beams and the muscle fiber orientation are parallel in a significant part of the myocardium, resulting in low echogenicity. On the contrary, in the long axis view only the apical region suffers from this artifact. As a result, only in 50% of the cases the combination improves the segmentation results in the long axis view.

A deformable model that only uses the cross-correlation force underestimated the blood pool region in some cases (Fig. 7.6). This is most likely caused by the larger windows used in the calculation of correlation values and because of the blood close to the heart wall 'adhering' to the moving cardiac tissue, leading to a higher maximum correlation value, i.e., lower MCC contrast, in blood regions close to the endocardial border.

In high quality images (without low contrast regions), segmentation exclusively based on the AMS force already yielded accurate results. In these images, the MCC force did not have additional value or even led to slightly lower similarity indices in some planes, see for example the SI's for data set 9 in Tables 7.2 and 7.3. However, from the 2D and 3D similarity indices as shown already in Tables 7.2 and 7.3, we might conclude that on average, the MCC force does improve the segmentation results. It should be noted that these tables show only average SI's, while improvement of the SI for individual planes demonstrates greater differences between the three force types (e.g. see Fig. 7.5a, short axis views).

Presently, the MCC parameter has been tested in the end-systolic phase because of the limited frame rate of the used echomachine while imaging the entire left ventricle. The limited frame rate results in a limited accuracy of cross-correlation in phases of the heart cycle with fast deformation of the heart muscle. Consequently, we firstly evaluated the performance in cardiac phases with small deformation of the heart muscle, i.e., in the end-systolic or end-diastolic phase. However, with the introduction of the latest real-time 3D echocardiographic scanners increased frame rates seem to be a matter of time. For now, the cross-correlation based model could be used in the end-diastolic and end-systolic phases as a more robust initialization for segmentation of the other frames in the cardiac cycle. In future, the method will be extended to more frames during the cardiac cycle. Since the temporal behavior of blood is also not constant over the heart cycle, incorporation of this knowledge might be beneficial to improve the proposed approach.

The ECG gated full volume data sets used in this study comprise four to seven cardiac cycles to build up a complete volume. So-called stitching artifacts may occur due to inaccurate synchronization between two consecutive heart beats, because of heart rate variation or motion of the patient due to respiration. It is clear that this inaccurate synchronization between cardiac cycles will have a severe influence on the temporal cross-correlation values since these are calculated using 3D volumes. For this reason, full volume datasets that contain severe stitching artifacts are less suitable for MCC based segmentation. It should be mentioned that these stitching artifacts often cause disturbance of the geometry as well and these data cannot be used for quantitative analysis anyway.

Further research is required to investigate the optimal combination of echolevel and temporal information. In the combined force model that is currently used, AMS and MCC forces are equally weighed. A more sophisticated balance between these two forces might improve the segmentation results. This could be done by implementing a quality measure for transitions between blood and myocardium. For example, in high quality images with high contrast borders, the AMS force should dominate over the MCC force. In contrast, MCC values close to one should be relied on stronger than lower MCC values. Additionally, location specific weighting might be applied. For example in the apical region, the AMS based segmentation is generally worse than the MCC based one, in contrast to the septal wall that is normally better segmented using AMS values as external force. This information might be beneficial for improving the overall performance of a segmentation method using both MCC and AMS.

In conclusion, temporal information present in the RF signal yields a useful parameter to distinguish between blood and endocardial border in regions with low contrast in echogenicity. The MCC value improves segmentation in these regions but further investigation of this parameter is required to exploit the full benefit of it for automated segmentation.

Acknowledgements

This work is supported by the Dutch Technology Foundation (STW), project 06466 and Philips Medical Systems. The authors would like to thank Bob Rijk and Imke Janssen for their assistance with the echographic image acquisitions and Janneke Kammeraad for her assistance in the manual segmentation of the echographic datasets.

8

DISCUSSION AND CONCLUSIONS

8

8.1 Research objective

Investigation of the cardiac function is of great clinical relevance. In particular, in children with a congenital heart disease, monitoring the cardiac function is important for clinical decision making and treatment planning. Knowledge about the exact geometry of the heart is essential for a correct assessment of cardiac function. The use of conventional two-dimensional (2D) echocardiography for functional assessment, e.g., assessment of the left ventricular volume, is inherently limited as geometrical assumptions about the (simplified) shape of the ventricle have to be made. These assumptions may lead to inaccurate ventricular function estimation in diseased hearts and in foreshortened 2D images of the ventricle. Three-dimensional (3D) echocardiography significantly reduces these limitations and, therefore, has better opportunities for accurate functional analysis [Gopal et al. 1995].

Manual processing of 3D echocardiographic images to perform quantitative analysis is time-consuming and subject to intra- and inter-observer variability. Automatic analysis of these images can be a helpful tool to overcome these limitations. In this thesis, we aimed at automatic segmentation of the left ventricle in pediatric echocardiographic images. These images often do not satisfy the standard geometry assumptions made in methods applied to echographic images of standard adult heart geometry. Our aim was to develop an accurate segmentation method without using a-priori information on geometry and the shape of the cardiac structures and, in addition, utilizes the rich phase information available in the radio frequency (RF) signal.

8.2 Contributions

For automatic segmentation, it is important that the information about the edges between various anatomical structures can be extracted from the image. Segmentation in 3D echocardiography is a challenging task because of the influence of the inherent "speckle" noise and the reduced echogenicity contrast between blood and the heart muscle in some regions. As a result, the endocardial border is not always clearly visible. We chose to analyze the speckle characteristics of the demodulated RF-data of blood and heart muscle in order to develop an adaptive filtering method that profits from knowledge about the statistics of ultrasound speckle (Chapter 2). Analysis of the filtering results shows that the speckle noise is reduced and the distinction between echo-levels originating from blood and endocardial wall has improved. As the filter uses knowledge about speckle statistics, it might also be applied to non-cardiac ultrasound images (c.f., van Hees et al. [2007]), optimizing the differentiation of tissues with different speckle characteristics.

We proposed a semi-3D method for segmentation of the endocardial surface that uses adaptive filtering to segment the endocardial border. Our adaptive filtering method has proven to be effective for segmentation of echocardiographic images (Chapter 3). No a priori knowledge about the shape of the left ventricle was incorporated. Inspired by the continuous (in space and time) deformation of the heart we incorporated spatio-temporal information in the segmentation protocol to further improve the results.

Assessment of the left ventricular volume yields one of the most important clinical parameters for monitoring (congenital) heart disease: cardiac output. Accurate, non-invasive assessment of this parameter is still a challenge. We developed a method for 3D segmentation of the left ventricle that can also deal with non-standard echographic images (Chapter 4). It should be noted that commercially available techniques for segmentation of the left ventricle are driven by internal models of average adult geometry and are based on standard viewing angles. These methods are in general not suitable for analysis of pediatric images. Evaluation of our method in non-standard images in an in vivo cardiac output animal study revealed good agreement between gold standard cardiac output measurements and cardiac output as estimated by the automatic segmentation method (Chapter 4). Compared to manual segmentation, this method is less labor-intensive and also removes the inevitable inter-observer variability. A systematic underestimation of the gold standard cardiac output was reported for the cardiac output as estimated by the segmentation algorithm. An explanation for the underestimation of the gold standard cardiac output is the relatively low temporal resolution (11 volumes per heart beat) of the acquired 3D echographic image sequences. This underestimation of the cardiac output will be reduced using the latest generation ultrasound systems that are capable of acquiring 3D data at higher temporal resolution.

In order to obtain more accurate segmentation in regions with low contrast between blood and myocardial tissue without the necessity of making assumptions on the shape of the ventricle or viewing angle, we investigated the use of temporal cross-correlation techniques (Chapter 6). These techniques are based on the principle that echographic data of two successive time frames will correlate more for myocardial tissue than for fast moving blood. Cross-correlation techniques are widely used for "strain" (relative deformation) imaging to assess the displacement and elasticity of the tissue (Chapter 5). The rich phase information present in the RF-signal was used to assess accurate cross-correlation values. We have shown that temporal cross-correlation can be a valuable feature to differentiate blood from myocardium. Evaluation of the segmentation method in 3D echocardiographic images of ten healthy children showed the feasibility of using temporal cross-correlations for segmentation of the left ventricular border in problematic low contrast regions (Chapter 7).

8.3 Discussion

We have proposed several methods for automatic segmentation of echocardiographic images with a focus on the analysis of pediatric images. These methods might contribute to the broad applicability of 3D echocardiography to diagnose and to monitor cardiac disease by making it less observer-dependent and more reliable. The automatic methods are also less time-consuming and labor intensive than manual analysis.

Since no a priori knowledge about the average shape of the ventricles was incorporated, our techniques are also applicable to non-standard images, for example in non-standard geometries or non-standard ultrasound viewing angles. Pediatric images often do not satisfy the geometrical assumptions on the shape of the ventricle that are generally made in commercially available automated analysis methods. Even more, in children with congenital malformations, geometrical assumptions may lead to inaccurate assessment of cardiac geometry and function. Also, for optimal imaging of the pediatric heart, different positions on the thorax and different viewing angles are often needed due to the different position of the heart within the thorax and small intercostal spaces resulting in shadowing artifacts. We have shown that our technique is capable to analyze images with non-standard viewing angle and yields accurate results in pediatric images (Chapter 4). Since the segmentation method is not based on prior knowledge about the anatomy (shape) of the left ventricle, the method might also be suitable for segmentation of other anatomical structures, such as the cerebral ventricles in neonates or the right ventricle of the heart, for example in patients with pulmonary hypertension.

The nature of cardiac ultrasound images imposes strong demands on the segmentation algorithm, in particular in regions where the orientation of the ultrasound beam is parallel to the orientation of the muscle fibers. Segmentation purely based on differences in echogenicity is problematic in these low contrast regions.

In images of the adult heart with normal anatomy, a model based approach that uses a priori knowledge about the shape or appearance of the ventricle [Bosch et al. 2002; Hansegard et al. 2007; van Stralen et al. 2007] might be advantageous in these low contrast regions. It is known that, in particular in these problematic low contrast regions, expert cardiologists also rely on implicit knowledge about the shape, position and appearance of the cardiac structures when analyzing echocardiographic images. However, in order to obtain more accurate assessment in non-standard images in these low contrast regions, a priori knowledge about the average shape of the ventricle cannot be relied on and additional echo features should be searched for. In this study we showed that temporal information can be used to obtain a cross-correlation based feature that can improve the accuracy of the segmentation in low contrast regions (Chapters 6 and 7). It has been shown (Chapter 6) that cross-correlation values may enhance the contrast between blood and myocardial tissue in regions where myocardial echogenicity is within the range of blood echogenicity.

A limitation of the cross-correlation based segmentation is that presently it has been evaluated only in cardiac phases with small deformation of the heart muscle, i.e., in the end-systolic and end-diastolic phases. The limited frame rate of the currently used echo machine results in a too much decreased cross-correlation value for blood as well as tissue in phases of the heart cycle with fast deformation of the heart muscle. With the introduction of the latest real-time echocardiographic transducers higher frame rates are introduced and further developments will increase these frame rates even more. Although the quality of ultrasound imaging has improved significantly over the past decades, image quality still limits the possibilities of automated image analysis. The well-known trade-off between spatial and temporal resolution in particular affects the quality of 3D images. Currently, for imaging of the entire left ventricle, four to seven consecutive cardiac cycles are needed to build up a complete 3D volume. As ECG-gating is used to synchronize the (real-time) acquired subvolumes, heart rate variation or motion due to respiration or patient's movement may cause severe "stitching" artifacts due to inaccurate synchronization. Stitching artifacts hamper quantitative analysis as the geometry might be disturbed and endocardial borders show incorrect irregularities.

However, compared to other imaging modalities such as CT and MRI, 3D echocardiography is a very competitive imaging modality because it is a real-time, non-invasive and low-cost imaging modality with short acquisition time and no use of ionizing radiation. Furthermore, it is expected that in near future ultrasound imaging techniques will improve further by using better transducer materials and increasing the number of parallel receive beams, allowing higher spatial resolution and higher frame rates. Real-time imaging of large 3D volumes with good image quality then comes within reach.

8.4 Recommendations for future research

Since the quality of automated image analysis strongly depends on the quality of the images, improvement of image quality is obviously one of the major issues that can improve automated analysis of 3D echocardiography and thus promote a widespread use of 3D echocardiography.

A promising recent technique to improve image quality is based on fusion of ultrasound images obtained from different positions on the thorax [Grau et al. 2007, 2008]. A larger field of view is obtained with better image quality, as the angle of incidence of the ultrasound beam is now varied and cardiac structures that are almost parallel to the ultrasound beam for one angle (and thus have low echogenicity), will yield higher echogenicity contrast when scanned from another angle. Images obtained from multiple viewing angles were combined using image registration techniques and it has been shown that segmentation results improved [Rajpoot et al. 2009]. Since the representation of cardiac structures in echocardiographic images is strongly dependent on the angle of incidence, further investigation of fusion techniques might contribute to more reliable analysis of echocardiographic images.

Since expert cardiologists also use temporal information as an important source to identify functional information and static image artifacts, further research should be directed towards temporal analysis of the data. For example, as an extension of adaptive filtering in the spatial domain (Chapter 3), spatio-temporal adaptive filtering might be applied to further improve the image quality for segmentation purposes.

As shown in this thesis, temporal cross-correlation between two subsequently acquired echographic volumes has additional value for segmentation in regions with poor contrast between blood and myocardium. Optimal settings of window sizes and dimensions for computation of the cross-correlation should be investigated more extensively. The balance between the use of more conventional gray-level based features and the newly developed cross-correlation feature should be further refined and improved. Location specific weighting of both features could be applied to favor the cross-correlation information in low contrast regions (very often located at the sides of the images) above gray-level based information.

Since the motion of the tissue can be derived from the temporal correlation between consecutive echographic volumes using strain imaging techniques, integration of strain and segmentation techniques seems obvious: the motion estimates could be used to translate the segmentation results from one time frame to the next time frame. On the other hand, the geometrical information as obtained from the segmentation method can serve as a pre-processing step for strain imaging. Further research is required to define a quality measure for transitions between blood and myocardium. This measure could be used to obtain a more sophisticated balance between image features such that low contrast regions, or for example near-field clutter and noisy edges, can be handled in a more reliable way.

Finally, an integrated approach using simultaneous segmentation of the left ventricular endocardial and epicardial border, as well as the right ventricular border, could support reliable assessment of overall cardiac geometry. One could then use constraints based on the minimal myocardial thickness and the incompressibility of the heart muscle. Segmentation of the epicardial border [Walimbe et al. 2006; Zhu et al. 2007; Orderud et al. 2008] is even more challenging than segmentation of the endocardial border because of the limited visibility.

8.5 Conclusion

In conclusion, we have shown that advancement has been made to allow automated segmentation in (non-standard) pediatric echocardiographic images.

Knowledge on speckle statistics led to an adaptive filtering method that optimizes the distinction between blood and heart muscle and thus facilitates segmentation. Segmentation based on adaptive filtered data yielded good results in the left ventricle of healthy children. In non-standard echographic data, cardiac output values as derived from volumes determined with the segmentation method showed excellent correlation with the gold standard. The combination of temporal cross-correlation as used in strain imaging techniques with segmentation has been proven to be an effective one and has paved the way for a more intensive interweaving of strain and segmentation techniques.

One can think of many opportunities to improve automated analysis of 3D echocardiographic images. More effective use of temporal and phase information and integration of segmentation of surrounding cardiac structures can increase the reliability of automated analysis. Image quality is still a limiting aspect of echography but it might be improved by fusion techniques or, as is expected in future, by improvements in 3D ultrasound techniques that increase both spatial and temporal resolution.

9

SUMMARY

9

Although the incidence of congenital heart disease in newborns has remained stable in the last decades, the overall number of patients with a congenital heart disease has increased. This can be explained by the fact that due to successful (surgical) treatment more and more young patients survive and reach adulthood. The demand for reliable, non-invasive, methods for diagnosis and regular monitoring of patients with a heart disease is therefore of great interest. In particular, in children with cardiac malformations regular monitoring of the cardiac function is of great importance to decide on timely intervention thus preventing heart failure: because of a cardiac malformation, the heart often has to compensate for the increased workload and the heart muscle will thicken (hypertrophy). This may lead to the formation of scar tissue (fibrosis), an irreversible process, and often leading to heart failure.

During the past decades, echocardiography has become an increasingly important imaging technique because of the high temporal resolution and because of the fact that this technique is not invasive and causes minimal discomfort for the patient. The recent introduction of three dimensional (3D) ultrasound techniques facilitates accurate assessment of the exact geometry and deformation of the heart in three dimensions. The addition of this third dimension is very important for the diagnosis of children with a (congenital) heart disease since the precise determination of the geometry in 3D can be of eminent importance when abnormal cardiac anatomy is present.

Since "manual" computer analysis of 3D ultrasound images is time-consuming and is sensitive to judgment differences between human experts, automated analysis of these images is desired. This thesis contributes to automating the analysis of 3D (pediatric) echographic images of the heart.

Chapter 1 provides an overview of the development and characteristics of ultrasound imaging or echography. More specifically, explanation is given on echographic imaging of the heart and analysis of the acquired images. In addition, an overview of automated segmentation methods for echocardiography is given. Finally, the objective of the research in this thesis is presented: Automated segmentation (to distinguish regions with different types of tissue) of three-dimensional echocardiographic images without using a priori knowledge about the average shape of the heart. In this thesis also a new parameter for automated segmentation is introduced: the temporal correlation of the raw, unprocessed ultrasound data.

Chapter 2 focuses on statistical analysis of speckle, the granular pattern typical of ultrasound images. The speckle pattern originates from the interference of the reflected ultrasound beams and indirectly provides information about the tissue properties. Analysis of the statistical characteristics of speckle (also called speckle statistics) can be used to distinguish between different tissues. In this chapter, speckle statistics of manually segmented blood and myocardial (heart muscle) regions were investigated. The statistical distribution of the speckle pattern of blood and heart muscle could be optimally modeled by a K-probability distribution or by a Gamma-probability distribution. One of the conclusions of this study was that the Gamma-distribution is preferable to the K-distribution, for both its simplicity and its more robust estimate of the characteristic parameters of this probability distribution.

These parameters of the Gamma-distribution can therefore be used to distinguish between blood and myocardium in ultrasound images. However, if the parameters were used in a parametric imaging approach, accurate estimation of the parameters required a large window size, leading to unacceptable blurring of the interface (edges) between two tissues. Thus, successful segmentation based on these parametric images was not feasible. Nevertheless, based on the scaling parameter of the Gamma-distribution an adaptive filter was developed that successfully combines the knowledge about the underlying speckle statistics with the advantage of adaptivity. This adaptive filter adapts to the characteristics of the image in the, moving, picture window and preserves the edges between anatomical structures.

Chapter 3 builds on the knowledge of speckle statistics obtained in Chapter 2. Segmentation in ultrasound images is difficult because of the presence of speckle noise. The effect of different (adaptive) filtering methods on the discrimination between blood and myocardium was extensively studied in this chapter. Because the filters were applied to the amplitude-demodulated raw ultrasound data and the images were thus processed along the scan lines of the transducer, the speckle size in the transverse direction was practically depth independent and a fixed filter window size could be used for all echo depths.

Overlap of the speckle statistics of blood and myocardium was compared before and after filtering and quality analysis (Receiver Operating Characteristic, ROC) of the manually segmented regions was performed to evaluate the impact of the different filtering methods. From the results it can be concluded that adaptive filtering based on the knowledge about speckle statistics optimizes the distinction between blood and myocardium and therefore automated segmentation can benefit from adaptive filtering.

The adaptive filter was then successfully combined with a so-called deformable contour for semi-3D automated segmentation of the heart wall in 3D ultrasound images: segmented contours of the inner border of the heart muscle (endocardial contours) of the individual planes were combined into a 3D endocardial surface. The method was evaluated on 3D ultrasound images of children. By imposing spatial and temporal continuity (3D + t) for contours of the separate planes, based on the continuous movement of the heart, better segmentation of the endocardial surface was obtained than when using information of each plane separately.

Chapter 4 describes a 3D technique for segmentation of the left ventricle that can handle non-standard echocardiographic images. It should be noted that commercially available techniques for segmentation of the left ventricle are driven by an internal model of the left ventricle based on the geometry of an average adult heart and also assume a fixed, default position of the transducer on the thorax. In general, these techniques are not suitable for the analysis of pediatric echocardiographic images because the shape of the heart is different from the normal heart and often a different application position of the transducer on the thorax is used. The method described in Chapter 4 does not assume a priori knowledge about the shape of the left ventricle or a default position of the transducer. A technique for 3D segmentation of the endocardial surface was developed through a combination of 3D adaptive filtering and a 3D deformable model. For each iteration step, this model deforms and evolves from an initial position in the left ventricle until a transition to another type of tissue is detected.

The method was successfully evaluated in an *in vivo* animal model to study the cardiac output: the volume of blood (ml/min) being pumped by the heart into the pulmonary or aortic artery. Accurate, non-invasive assessment of cardiac output would be a major step forward in cardiology. In this study, cardiac output was computed after segmentation of the left ventricle in ultrasound images captured in the end-diastolic and end-systolic phases of the cardiac cycle. The cardiac output derived from the automated segmentation was compared with cardiac output values measured from the volume flow invasively determined with a flow probe around the pulmonary artery. This latter measurement provides the reference value or gold standard of the measurement. The results show that the segmentation method yields excellent correlation with respect to the gold standard cardiac flow measurements results. Systematic underestimation of the flow-based cardiac output was obtained. This could be explained by the relatively low temporal resolution of echographic volumes. The underestimation might be reduced by using the latest generation ultrasound systems since they have the capability of acquiring 3D data at higher temporal resolution.

The echogenicity contrast between blood and myocardial regions can be very low if the propagation direction of the ultrasound beam is mainly parallel to the orientation of the muscle fibers. This low contrast complicates the segmentation in these areas and leads to incorrect results since the endocardial wall is hardly visible in the ultrasound image. Prior knowledge about the shape of the ventricle would facilitate the segmentation process in these regions. However, in this thesis no specific knowledge about the shape of the heart is incorporated in the method such that the technique might be applied even in non standard ultrasound images, for example in children with an abnormal heart anatomy. Therefore, additional features should be explored to differentiate between blood and myocardium in these problematic low contrast regions. In the second part of this thesis (chapters 5 to 7), the use of new, temporal information to determine the 3D geometry of the heart is investigated.

The temporal cross correlation between two consecutive ultrasound volumes is a commonly used parameter for estimating the relative deformation of the heart muscle in strain imaging: assessment of contraction and relaxation of tissue. These cross-correlation techniques could also be used to optimize the distinction between blood and heart muscle. The relatively slow moving heart muscle will yield a high cross-correlation between subsequent 3D echo volumes while subsequent echo signals from fast-flowing blood in the ventricles will have a lower cross-correlation. The temporal cross correlation will therefore be distinctive for blood and myocardium and can be used as an additional feature in the segmentation process.

Chapter 5 describes techniques for the estimation of temporal cross-correlation and corresponding displacement of the tissue using a phased array transducer. This study shows that the use of two-dimensional windows for displacement and strain estimation outperforms the use of one-dimensional windows. Furthermore, it is shown that the use of so-called re-correlation techniques improves the results.

In chapter 6, the use of 2D temporal cross-correlation as an additional parameter for segmentation of the endocardial wall was studied. The temporal cross-correlation is determined in an iterative process where displacement estimates at a coarse scale are used to optimize cross-correlations and displacement estimates in the next, finer iteration step. Typical differences between parameters solely based on gray-level information and the new cross-correlation parameter are discussed using illustrative examples. Using these examples and the segmentation of the left ventricle in 3D pediatric ultrasound images, it is demonstrated that the temporal cross-correlation parameter has additional value in particular in regions with low contrast between blood and heart muscle.

The extension to a 3D segmentation method based on full 3D cross correlation is described in Chapter 7. Since the heart moves and deforms in three dimensions, it seems obvious to use a 3D cross-temporal correlation, such that displacements and corresponding cross-correlations can be estimated in three dimensions. Again an iterative algorithm was used. For each iteration, a finer and more accurate estimate of the 3D displacement is made, hereby using the rich phase information that is present in the raw echo signal, in addition to amplitude signal. Using this algorithm, the temporal cross-correlation between two successive volumes could be optimized. This cross-correlation is then used as an additional deformation force in a 3D deformable model. This new force was tested and combined with the previously defined force based on grayscale information: adaptive filtering (Chapters 3 and 4).

Evaluation of the method in 3D echographic images of 10 healthy children showed that the addition of temporal information in the form of cross-correlation leads to improvement of the segmentation results, especially in areas with low contrast between blood and myocardium. The use of temporal cross-correlation information therefore is a promising step to improve segmentation in 3D echocardiographic images and future research in this direction is recommended.

Finally, Chapter 8 summarizes the conclusions of the individual chapters and discusses the results of the research as described in this thesis. Recommendations for future research include fusion of multiple ultrasound images recorded from different angles to improve the image quality and thus leading to a possible improvement of the segmentation results. As expert cardiologists use temporal features as an important source of information in their analysis of ultrasound images of the heart, future research should also be more focused on these temporal parameters. Cross-correlation techniques, as described in the second part of this thesis, are already contributing to research on this temporal information and these techniques can be further refined and optimized.

The techniques developed in this study contribute to an objective, automated analysis of pediatric echocardiographic images. Because no explicit knowledge about the geometry of the left ventricle is assumed, the techniques might also be applied to different anatomical structures, for example to the right ventricle, or in children with an abnormal cardiac anatomy.

10

SAMENVATTING

10

Alhoewel het aantal hartafwijkingen bij pasgeborenen de afgelopen decennia gelijk is gebleven, is het aantal patiënten met een hartafwijking juist gegroeid. Dit kan worden verklaard uit het feit dat door succesvolle (chirurgische) behandeling steeds meer jonge patiënten in leven blijven en de volwassen leeftijd bereiken. De vraag naar betrouwbare, niet-invasieve, methoden voor het diagnosticeren en regelmatig controleren van patiënten met een hartaandoening is daardoor zeer actueel. In het bijzonder bij kinderen met een hartafwijking is regelmatige controle van de hartfunctie van groot belang om tijdig te kunnen ingrijpen ter voorkoming van hartfalen. Ten gevolge van een hartafwijking zal het hart vaak harder moeten pompen en daardoor zal, ter compensatie, net als bij een atleet die veel traint, de hartspier dikker worden (hypertrofie). Dit kan leiden tot de vorming van littekenweefsel (fibrose) en aangezien dit een onomkeerbaar proces is, zal dit uiteindelijk leiden tot hartfalen.

Gedurende de afgelopen decennia is echocardiografie een steeds belangrijkere beeldvormende techniek geworden vanwege de snelle beeldvorming (hoge temporele resolutie) en het feit dat deze techniek niet invasief is en dus niet belastend is voor de patiënt. De opkomst van driedimensionale (3D) echografie maakt het mogelijk de exacte geometrie en vervorming van het hart in drie dimensies zichtbaar te maken. De toevoeging van deze derde dimensie is zeer belangrijk voor de diagnose van kinderen met een hartafwijking omdat het exact bepalen van de geometrie in 3D juist bij afwijkingen van de anatomie van het hart een grote meerwaarde kan hebben.

Aangezien "handmatige" computer analyse van 3D echobeelden arbeidsintensief en dus kostbaar is en bovendien gevoelig is voor verschillen in beoordeling tussen de verschillende beoordelaars, is automatische analyse van deze beelden gewenst. Dit proefschrift draagt bij aan het automatiseren van de analyse van 3D (pediatrische) echobeelden van het hart.

Hoofdstuk 1 geeft een overzicht van de ontwikkeling en eigenschappen van ultrageluidstechnieken, van de echografie dus. Meer specifiek wordt uitleg gegeven over echografie van het hart en de analyse van verkregen echobeelden. Daarnaast wordt een overzicht gegeven van automatische segmentatie methoden voor echocardiografie. Vervolgens wordt het doel van het onderzoek in dit proefschrift besproken: automatische segmentatie (onderscheiden van gebieden met verschillende soorten weefsel) van driedimensionale echocardiografische beelden zonder daarbij voorkennis te gebruiken over de gemiddelde vorm van het hart. Tevens wordt in dit proefschrift de temporele correlatie van de ruwe, onbewerkte ultrageluidsdata als nieuwe parameter voor automatische segmentatie geïntroduceerd.

Hoofdstuk 2 richt zich op statistische analyse van speckle, het ruizige patroon dat typisch is voor ultrageluidsbeelden. Het korrelige speckle-patroon ontstaat door interferentie van de teruggekaatste ultrageluidsbundels en geeft indirect informatie over de eigenschappen van het onderliggende weefsel. Analyse van de speckle statistiek kan gebruikt worden om verschillende weefsels van elkaar te onderscheiden. In dit hoofdstuk is de speckle statistiek van het bloed en de hartspier (myocard) onderzocht op basis van handmatig ingetekende gebieden. De statistische verdeling van het speckle patroon, kortweg "speckle statistiek", van bloed en hartspier bleek het beste gemodelleerd te kunnen worden door een K- of een Gamma kansverdeling. Eén van de conclusies van dit onderzoek was dat de Gamma-verdeling vanwege zijn eenvoud en meer robuuste schatting van de parameters van deze kansverdeling, de voorkeur heeft boven de K-verdeling.

De parameters van de Gamma-verdeling kunnen dus gebruikt worden om in echobeelden bloed te onderscheiden van hartspier. Echter wanneer de parameters gebruikt worden voor het berekenen van parametrische beelden, blijkt dat voor een accurate schatting van de parameters een (te) groot "beeldvenster" nodig is en ook dat de randen van de anatomische structuren te veel vervagen. Succesvolle segmentatie op basis van deze parametrische beelden is dus niet uitvoerbaar. Op basis van de schalingsparameter van de Gamma-verdeling is vervolgens een "adaptief filter" ontwikkeld dat de verworven kennis over de onderliggende speckle statistiek succesvol combineert met het voordeel van adaptiviteit en behoud van randen tussen anatomische structuren. Dit adaptieve filter past zich aan aan de kenmerken van het beeld in het beeldvenster.

Hoofdstuk 3 borduurt voort op de kennis over speckle statistiek verkregen in hoofdstuk 2. Segmentatie in ultrageluidsbeelden is niet eenvoudig vanwege de aanwezigheid van speckle ruis. Het effect van verschillende (adaptieve) filters op de mate van onderscheid tussen bloed en hartspier wordt uitgebreid bestudeerd in dit hoofdstuk. Doordat de filters worden toegepast op beelden verkregen door amplitude-demodulatie van het ruwe ultrageluidssignaal en dus de scan-lijnen van de transducent als input gebruiken, is de speckle grootte in dwarsrichting onafhankelijk van de diepte en kan dus voor alle echodieptes een beeldvenster met vaste grootte worden gebruikt.

Overlap van de grijswaarden statistiek van bloed en hartspier vóór en na filtering werd vergeleken en kwaliteitsanalyse (Receiver Operating Characteristic, ROC) van de handmatig gesegmenteerde gebieden werd uitgevoerd om het effect van de verschillende filtermethoden te bepalen. Uit de resultaten kan geconcludeerd worden dat adaptieve filtering op basis van de verworven kennis over speckle statistiek het onderscheid tussen bloed en hartspier optimaliseert en dat daarom automatische segmentatie kan profiteren van adaptieve filtering.

Het adaptieve filter werd vervolgens succesvol gecombineerd met een zogenaamde deformable contour voor semi-3D segmentatie van de hartwand in 3D echobeelden: gesegmenteerde binnenwand (endocardiale) contouren van de afzonderlijke vlakken werden gecombineerd tot een 3D endocardiaal oppervlak. De methode werd geëvalueerd op 3D echobeelden van kinderen. Het opleggen van spatio-temporele randvoorwaarden (3D + t) gebaseerd op de continue beweging van het hart leidde tot een verbetering van de resultaten ten opzichte van segmentatie enkel gebaseerd op de informatie van het desbetreffende 2D vlak.

In hoofdstuk 4 wordt de overstap gemaakt naar volledige 3D segmentatie. Er werd een 3D segmentatietechniek voor de linker hartkamer (-ventrikel) ontwikkeld die om kan gaan met niet-standaard echocardiografische beelden. Hierbij moet worden opgemerkt dat de segmentatie technieken voor het linker ventrikel, die commercieel verkrijgbaar zijn, gebruikmaken van een intern model van het linker ventrikel op basis van de gemiddelde geometrie van een volwassen hart en uitgaan van een standaard positie van de transducent op de borstkas. Over het algemeen zijn deze technieken niet toepasbaar op echobeelden van het hart van kinderen vanwege de afwijkende vorm en vaak ook andere optimale positie van de transducent op de borstkas. De methode zoals beschreven in hoofdstuk 4 gaat niet uit van voorkennis over de vorm van het linker ventrikel of van een standaard positie van de transducent. Een 3D techniek voor segmentatie van de endocardiale wand werd ontwikkeld door middel van een combinatie van 3D adaptieve filtering en een 3D "deformable" model. Dit model vervormt en groeit in stapjes vanuit een beginpositie in het linker ventrikel totdat een overgang naar een ander soort weefsel wordt gevonden.

Deze methode werd succesvol geëvalueerd in een *in vivo* diermodel studie naar het hartminuutvolume, de hoeveelheid bloed die per minuut door het hart in de hoofdslagader wordt gepompt. Een accurate, niet-invasieve bepaling van het hartminuutvolume zou een grote stap vooruit zijn in de cardiologie. In deze studie werd het hartminuutvolume berekend op basis van de segmentatie van het linker ventrikel in echobeelden opgenomen in eind-diastolische en eind-systolische fase van de hartcyclus. Dit berekende volume werd vergeleken met het hartminuutvolume (invasief) bepaald met een stromingssnelheid meter (flow probe) rondom de longslagader. Deze laatste meting levert de referentie waarde, de "gouden standaard", van de meting. Het hartminuutvolume, zoals berekend na automatische segmentatie, bleek zeer goed overeen te stemmen met de gouden standaard metingen. Wel trad een systematische onderschatting op van het flow-gebaseerde hartminuutvolume. De relatief lage temporele resolutie van de echo volumes kan hiervan de oorzaak zijn en naar verwachting zal dit probleem bij nieuwere echo machines met hogere temporele resolutie minder groot zijn.

Het contrast tussen bloed en hartspier kan in de gebieden waar de ultrageluidsbundel parallel loopt met de hartspier zeer laag zijn. Dit lage contrast bemoeilijkt de segmentatie in deze gebieden en leidt tot incorrecte resultaten aangezien de endocardiale wand niet of nauwelijks zichtbaar is in het echobeeld. Voorkennis over de vorm van het ventrikel zou in deze situaties uitkomst kunnen bieden. Echter één van de uitgangspunten van dit proefschrift is om niet uit te gaan van specifieke voorkennis over de vorm van het hart zodat de techniek ook toepasbaar blijft in niet standaard echobeelden, bijvoorbeeld bij kinderen met een hartafwijking. Er moet dan dus naar aanvullende informatie gezocht worden die in de gebieden met weinig contrast tussen bloed en hartspier wel onderscheidend is. Het tweede gedeelte van dit proefschrift (hoofdstuk 5 tot en met 7) behandelt het gebruik van nieuwe, temporele informatie voor het bepalen van de 3D geometrie van het hart.

De temporele "kruiscorrelatie" tussen twee opeenvolgende echovolumes is een veel gebruikte parameter voor het schatten van de relatieve vervorming van de hartspier, de zgn. strain ofwel relaxatie en contractie bepaling. Deze kruiscorrelatie technieken kunnen ook worden toegepast om het onderscheid tussen bloed en hartspier te optimaliseren. De relatief langzaam bewegende hartspier zal namelijk een hoge kruiscorrelatie opleveren tussen opeenvolgende 3D echosignalen terwijl opeenvolgende echosignalen van snelstromende bloed in de ventrikels een lagere kruiscorrelatie zullen hebben. De temporele kruiscorrelatie zal dus onderscheidend zijn voor bloed en hartspier en deze extra informatie kan worden toegevoegd aan het segmentatie proces.

Hoofdstuk 5 beschrijft technieken voor het bepalen van de temporele kruiscorrelatie en bijbehorende verplaatsingen van het weefsel bij gebruik van een phased array transducent. Uit deze studie blijkt dat het gebruik van tweedimensionale vensters voor het bepalen van de verplaatsing en deformatie betere resultaten oplevert dan het gebruik van eendimensionale vensters. Bovendien wordt aangetoond dat het gebruik van zogenaamde re-correlatie technieken de resultaten verbetert.

In hoofdstuk 6 wordt het gebruik van 2D temporele kruiscorrelatie als extra parameter voor segmentatie van de endocardiale wand bestudeerd. De methode voor het bepalen van deze correlatie bestaat uit een iteratief proces waarbij geschatte verplaatsingen op grove schaal gebruikt worden voor het optimaliseren van kruiscorrelaties en geschatte verplaatsingen in de volgende, fijnere iteratie stap. Typische verschillen tussen een puur op grijswaarden gebaseerde parameter en de nieuwe temporele kruiscorrelatie parameter worden besproken aan de hand van illustratieve voorbeelden. Aan de hand van deze voorbeelden en van segmentatie van het linker ventrikel in 3D echobeelden van kinderen wordt aangetoond dat, juist in de probleemgebieden waar het contrast tussen bloed en hartspier laag is, de temporele kruiscorrelatie toegevoegde waarde heeft.

De uitbreiding naar een 3D segmentatiemethode gebaseerd op volledige 3D kruiscorrelatie wordt beschreven in hoofdstuk 7. Aangezien het hart beweegt en vervormt in drie dimensies, ligt het voor de hand ook gebruik te maken van een driedimensionale temporele kruiscorrelatie, zodat verplaatsingen en bijbehorende kruiscorrelaties daadwerkelijk in drie dimensies geschat kunnen worden. Hierbij wordt wederom gebruik gemaakt van een iteratief algoritme waarbij steeds een fijnere schatting van de 3D verplaatsing gemaakt wordt, hierbij gebruikmakend van de informatierijke fase informatie die naast het amplitudesignaal aanwezig is in het ruwe echosignaal. Op deze manier wordt een zo optimaal mogelijke temporele kruiscorrelatie tussen twee opeenvolgende volumes bepaald. Deze temporele kruiscorrelatie wordt vervolgens gebruikt als extra vervormingskracht in een 3D deformable model. Deze nieuwe kracht werd getest ten opzichte van en in combinatie met de eerder gedefinieerde kracht op basis van grijswaarden: adaptieve filtering (hoofdstuk 3 en 4).

Uitgebreide evaluatie van de methode in 3D echobeelden van 10 gezonde kinderen heeft aangetoond dat het toevoegen van temporele informatie in de vorm van kruiscorrelatie een duidelijke verbetering van de segmentatieresultaten oplevert, met name in gebieden met weinig contrast tussen bloed en hartspier. Het gebruik van temporele kruiscorrelatie informatie is dan ook een veelbelovende stap voor het verbeteren van segmentatie in 3D echocardiografische beelden en toekomstig onderzoek in deze richting wordt geadviseerd.

Ten slotte geeft hoofdstuk 8 een overzicht van de conclusies van de afzonderlijke hoofdstukken en worden de resultaten van het onderzoek zoals beschreven in dit proefschrift bediscussieerd. Aanbevelingen voor toekomstig onderzoek omvatten onder andere fusie van meerdere ultrageluidsbeelden opgenomen vanuit verschillende hoeken voor het verbeteren van de beeldkwaliteit en dus leidend tot een mogelijke verbetering van de segmentatie resultaten. Aangezien cardiologen bij hun analyse van echobeelden van het hart temporele informatie gebruiken als belangrijke informatiebron, zou toekomstig onderzoek ook nog meer gericht moeten zijn op deze temporele parameters. Kruiscorrelatie technieken, zoals beschreven in het tweede gedeelte van dit proefschrift, dragen hier al aan bij en onderzoek naar deze technieken kan nog verder verfijnd en geoptimaliseerd worden.

De technieken die ontwikkeld zijn binnen dit onderzoek dragen bij aan een objectieve, automatische analyse van pediatrische echocardiografische beelden. Omdat geen expliciete voorkennis over de geometrie van het linker ventrikel wordt verondersteld, zijn de technieken in principe ook toe te passen op afwijkende structuren bijvoorbeeld in het rechter ventrikel of bij kinderen met een afwijkende geometrie van het hart.

Bibliography

K. Alam and J. Ophir. Reduction of signal decorrelation from mechanical compression of tissues by temporal stretching: applications to elastography. *Ultrasound Med Biol*, 23(1):95–105, 1997.

A. M. Alyassin, J. L. Lancaster, J. H. Downs, and P. T. Fox. Evaluation of new algorithms for the interactive measurement of surface area and volume. *Med Phys*, 21(6):741–752, 1994.

E. D. Angelini, A. F. Laine, S. Takuma, J. W. Holmes, and S. Homma. LV volume quantification via spatiotemporal analysis of real-time 3-D echocardiography. *IEEE Trans Med Imaging*, 20(6):457–469, 2001.

E. D. Angelini, S. Homma, G. Pearson, J. W. Holmes, and A. F. Laine. Segmentation of real-time three-dimensional ultrasound for quantification of ventricular function: a clinical study on right and left ventricles. *Ultrasound Med Biol*, 31 (9):1143–1158, 2005.

E. A. Ashton and K. Parker. Multiple resolution bayesian segmentation of ultrasound images. *Ultrason Imaging*, 17(4):291–304, 1995.

J. Bajorat, R. Hofmockel, D. A. Vagts, M. Janda, B. Pohl, C. Beck, and G. Noeldge-Schomburg. Comparison of invasive and less-invasive techniques of cardiac output measurement under different haemodynamic conditions in a pig model. *Eur J Anaesthesiol*, 23:23–30, 2006.

J. C. Bamber and C. Daft. Adaptive filtering for reduction of speckle in ultrasonic pulse-echo images. *Ultrasonics*, 24:41–44, 1986.

L. N. Bohs and G. E. Trahey. A novel method for angle independent ultrasonic imaging of blood flow and tissue motion. *IEEE Trans Biomed Eng*, 38(3):280–286, 1991.

J. G. Bosch, S. C. Mitchell, B. P. Lelieveldt, F. Nijland, O. Kamp, M. Sonka, and J. H. Reiber. Automatic segmentation of echocardiographic sequences by active appearance motion models. *IEEE Trans Med Imaging*, 21(11):1384–1383, 2002.

M. Botero, D. Kirby, E. B. Lobato, E. D. Staples, and N. Gravenstein. Measurement of cardiac output before and after cardiopulmonary bypass: Comparison among aortic transit-time ultrasound, thermodilution, and noninvasive partial CO2 rebreathing. *J Cardiothorac Vasc Anesth*, 18(5):563–572, 2004.

T. Böttger, T. Kunert, H. P. Meinzer, and I. Wolf. Application of a new segmentation tool based on interactive simplex meshes to cardiac images and pulmonary MRI data. *Acad Radiol*, 14(3):319–329, 2007.

D. Boukerroui, O. Basset, A. Baskurt, and G. Giminez. A multiparametric and multiresolution segmentation algorithm of 3-D ultrasonic data. *IEEE Trans Ultrason Ferroelectr Freq Control*, 48(1):64–77, 2002.

D. Boukerroui, A. Baskurt, J. A. Noble, and O. Basset. Segmentation of ultrasound images - multiresolution 2D and 3D algorithm based on global and local statistics. *Pattern Recognition Letters*, 24:779–790, 2003.

N. Bruining, C. Lancée, J. R. T. C. Roelandt, and N. Bom. Three-dimensional echocardiography paves the way toward virtual reality. *Ultrasound Med Biol*, 26 (7):1065–1074, 2000.

C. B. Burckhardt. Speckle in ultrasound B-mode scans. *IEEE Trans Sonics Ultrason*, 25:1–6, 1978.

E. I. Céspedes, J. Ophir, H. Ponnekanti, and N. Maklad. Elastography: elasticity imaging using ultrasound with application to muscle and breast in vivo. *Ultrason Imaging*, 17:73–88, 1993.

P. Chaturvedi, M. F. Insana, and T. J. Hall. 2-D companding for noise reduction in strain imaging. *IEEE Trans Ultrason Ferroelectr Freq Control*, 45(1):179–191, 1998.

X. Chen, H. Xie, R. Erkamp, K. Kim, C. Jia, J. M. Rubin, and M. O'Donnell. 3-D correlation-based speckle tracking. *Ultrason Imaging*, 27(1):21–36, 2005.

L. Clifford, P. Fitzgerald, and D. James. Non-Rayleigh first-order statistics of ultrasonic backscatter from normal myocardium. *Ultrasound Med Biol*, 19:487–495, 1993.

L. D. Cohen. On active contour models and balloons. *CVGIP: Image Understanding*, 53:211–218, 1991.

W. J. Conover. *Practical nonparametric statistics*. Wiley, New York, 1980.

T. F. Cootes, G. J. Edwards, and C. J. Taylor. Active appearance models. *IEEE Trans Pattern Anal Mach Intell*, 23(6):681–685, 2001.

C. Corsi, G. Saracino, A. Sarti, and C. Lamberti. Left ventricular volume estimation for real-time three-dimensional echocardiography. *IEEE Trans Med Imaging*, 21 (9):1202–1208, 2002.

J. Curie and P. Curie. Sur l'électricité polaire dans les cristaux hémièdres à faces inclinées. *C R Acad Sci Gen*, 91:383–386, 1880a.

J. Curie and P. Curie. Contractions et dilatations produites par des tensions dans les cristaux hémièdres à faces inclinées. *C R Acad Sci Gen*, 93:1137–1140, 1880b.

F. Davignon, J .F. Deprez, and O. Basset. A parametric imaging approach for the segmentation of ultrasound data. *Ultrasonics*, 43(10):789–801, 2005.

C. L. de Korte, E. I. Céspedes, A. F. W. van der Steen, B. Norder, and K. te Nijenhuis. Elastic and acoustic properties of vessel mimicking material for elasticity imaging. *Ultrason Imaging*, 19(2):112–126, 1997.

C. L de Korte, A. F. W. van der Steen, E. I. Céspedes, G. Pasterkamp, S. G. Carlier, F. Mastik, A. H. Schooneveld, P. W. Serruys, and N. Bom. Characterization of plaque components and vulnerability with intravascular ultrasound elastography. *Phys Med Biol*, 45(6):2000, 2000.

H. Delingette. General object reconstruction based on simplex meshes. *Int J Comput Vis*, 32(2):111–146, 1999.

R. Deriche. Fast algorithms for low level vision. *IEEE Trans Pattern Anal Mach Intell*, 12(1):78–87, 1990.

J. D'hooge, A. Heimdal, F. Jamal, T. Kukulski, B. Bijnens, F. Rademakers, L. Hatle, P. Suetens, and G. R. Sutherland. Regional strain and strain rate measurements by cardiac ultrasound: principles, implementation and limitations. *Eur J Echocardiogr*, 1(3):154–170, 2000.

J. D'hooge, B. Bijnens, J. Thoen, F. Van de Werf, G. R. Sutherland, and P. Suetens. Echocardiographic strain and strain-rate imaging: a new tool to study regional myocardial function. *Eur J Echocardiogr*, 21(9):1022–1030, 2002.

J. Dias and J. Leitao. Wall position and thickness estimation from sequences of echocardiograms images. *IEEE Trans Med Imaging*, 15(1):25–38, 1996.

L .R. Dice. Measures of the amount of ecologic association between species. *Ecology*, 26(3):297–302, 1945.

I. Dydenko, D. Friboulet, J. M. Gorce, J. D'hooge, B. Bijnens, and I. E. Magnin. Towards ultrasound cardiac image segmentation based on the radiofrequency signal. *Med Image Anal*, 7(3):353–367, 2003.

I. Edler and C. H. Hertz. The use of ultrasonic reflectoscope for the continuous recording of the movement of heart walls. *Kungl Fysiograf Sällskapets Lund Förh*, 24:40–58, 1954.

T. Eltoft. Modeling the amplitude statistics of ultrasonic images. *IEEE Trans Med Imaging*, 25:229–240, 2006.

S. Y. Emelianov, X. Chen, M. O'Donnell, B. Knipp, D. Myers, T. W. Wakefield, and J. M. Rubin. Triplex ultrasound: elasticity imaging to age deep venous thrombosis. *Ultrasound Med Biol*, 28(6):757–767, 2002.

H. Gao, H.F. Choi, P. Claus, S. Boonen, G. van der Perre, W. Lauriks, and J. D'hooge. A new convolution-based methodology to simulate ultrasound images in a 2D/3D sector format. In *Proc IEEE Int Ultrason Symp*, pages 2243–2246, New York, U.S.A., 2007.

B. S. Garra, E. I. Céspedes, J. Ophir, S. R. Spratt, R. A. Zuurbier, C. M. Magnant, and M. F. Pennanen. Elastography of breast lesions: Initial clinical results. *Radiology*, 202(1):79–86, 1997.

O. Gerard, A. C. Billon, Rouet J. M., M. Jacob, M. Fradkin, and C. Allouche. Left ventricular volume estimation for real-time three-dimensional echocardiography. *IEEE Trans Med Imaging*, 21(9):1059–1068, 2002.

I. H. Gerrits, M. M. Nillesen, R. G. P. Lopata, J. P. T. Rijk, J. M. Thijssen, and C. L. de Korte. A robust deformable simplex mesh model with temporal signal decorrelation contraints in echocardiography. In *Proc IEEE Int Ultrason Symp*, pages 1484–1487, New York, U.S.A., 2007.

A. S. Gopal, Z. Shen, P. M. Sapin, A. M. Keller, M. J. Schnellbaecher, and D. W. Leibowitz. Assessment of cardiac function by three-dimensional echocardiography compared with conventional noninvasive methods. *Circulation*, 92(4):842–853, 1995.

V. Grau, H. Becher, and J. A. Noble. Registration of multiview real-time 3-D echocardiographic sequences. *IEEE Trans Med Imaging*, 26(9):1154–1165, 2007.

V. Grau, C. Szmigielski, H. Becher, and J. A. Noble. Combining apical and parasternal views to improve motion estimation in RT3D echocardiographic sequences. In *Proc IEEE Int Symp Biomed imaging*, pages 516–519, Paris, France, 2008.

J. Hansegard, S. Urheim, K. Lunde, and S. I. Rabben. Constrained active appearance models for segmentation of triplane echocardiograms. *IEEE Trans Med Imaging*, 26(10):1391–1400, 2007.

H. H. G. Hansen, R. G. P. Lopata, S. Holewijn, M. Truijers, and C. L de Korte. Non-invasive vascular ultrasound strain imaging: different arteries, different approaches. In *Proc Eur Congr Med and Biomed Eng*, Antwerpen, Belgium, 2008.

L. Ibanez, W. Schroeder, L. Ng, and J. Cates. The ITK software guide. 2003.

D. R. Iskander, A.M. Zoubir, and B. Boashash. Method for estimating the parameters of the K distribution. *IEEE Trans Signal Process*, 47(4):1147–1151, 1999.

L. D. Jacobs, I. S. Salgo, S. Goonewardena, L. Weinert, P. Coon, D. Bardo, O. Gerard, P. Allain, J. L. Zamorano, L. P. de Isla, V. Mor-Avi, and R. M. Lang. Rapid online quantification of left ventricular volume from real-time three-dimensional echocardiographic data. *Eur Heart J*, 27(4):460–468, 2006.

E. Jakeman and P. N. Pussey. A model for non-Rayleigh sea echo. *Trans Antennas Propagation*, 24:806–814, 1976.

E. Jakeman and R. J. A. Tough. Generalized K distribution: a statistical model for weak scattering. *J Opt Soc Am A Opt Image Sci Vis*, 4:1764–1772, 1987.

J. A. Jensen. A program for simulating ultrasound systems. paper presented at the 10th Nordic-Baltic conference on biomedical imaging. pages 351–353, 1996.

C. Jia, K. Kim, T. J. Kolias, J. M. Rubins, W. F. Witzel, P. Yan, D. Dione, A. J. Sinusas, K. Duncan, and M. O'Donnell. 4D elasticity imaging of PVA LV phantom integrated with pulsatile circulation system using 2D phased array. In *Proc IEEE Int Ultrason Symp*, pages 876–879, New York, U.S.A., 2007.

F. Kallel and J. Ophir. Three dimensional tissue motion and its effect on image noise in elastography. *IEEE Trans Ultrason Ferroelectr Freq Control*, 44(6):1286–1296, 1997.

F. Kallel, M. Bertrand, and J. Ophir. Fundamental limitations on the contrast-transfer efficiency in elastography: an analytic study. *Ultrasound Med Biol*, 22 (4):463–470, 1996.

F. Kallel, J. Ophir, K. Magee, and T. Krouskop. Elastographic imaging of low-contrast elastic modulus distributions in tissue. *Ultrasound Med Biol*, 24(3): 409–425, 1998.

J. N. Kapur, P. K. Sahoo, and A. K. C. Wong. A new method for gray-level picture thresholding using the entropy of the histogram. *Comput Vision Graphics Image Proc*, 29(3):273–285, 1985.

M. Kass, A. Witkin, and D. Terzopoulos. Snakes: Active contour models. *Int J Comput Vision*, 1:321–331, 1987.

W. Khaled, S. Reichling, O. T. Bruhns, and H. Ermert. Ultrasonic strain imaging and reconstructive elastography for biological tissue. *Ultrasonics*, 44(Suppl I): 199–202, 2006.

R. Kolar, R. Jirik, and J. Jan. Estimator comparison of the Nakagami-m parameter and its application in echocardiography. *Radioengineering*, 13(1):8–12, 2004.

E. E. Konofagou and J. Ophir. A new elastographic method for estimation and imaging of lateral displacements, lateral strains, corrected axial strains and Poisson's ratios in tissues. *Ultrasound Med Biol*, 24(8):1183–1199, 1998.

E. E. Konofagou and J. Ophir. Precision estimation and imaging of normal and shear components of the 3D strain tensor in elastography. *Phys Med Biol*, 45(6): 1553–1563, 2000.

E. E. Konofagou, J. D'hooge, and J. Ophir. Myocardial elastography - a feasibility study in vivo. *Ultrasound Med Biol*, 28(4):475–482, 2002.

C. Kotropoulos and I. Pitas. Optimum nonlinear signal detection and estimation in the presence of ultrasonic speckle. *Ultrason Imaging*, 14:249–275, 1992.

S. Langeland. *Multi-Dimensional Quantification of Myocardial Deformation using Echocardiographic Imaging: Development, Implementation and Validation*. PhD thesis, Catholic University of Leuven, 2007.

S. Langeland, J. D'hooge, P. F. Wouters, H. A. Leather, P. Claus, B. Bijnens, and G. R. Sutherland. Experimental validation of a new ultrasound method for the simultaneous assessment of radial and longitudinal myocardial deformation independent of insonation angle. *Circulation*, 112(14):2157–2162, 2005.

W. N. Lee, C. M. Ingrassia, S. D. Fung-Kee-Fung, K. D. Costa, J. W. Holmes, and E. E. Konofagou. Theoretical quality assessment of myocardial elastography with in vivo validation. *IEEE Trans Ultrason Ferroelectr Freq Control*, 54(11): 2233–2245, 2007.

J. Lemson, W. P. de Boode, J. C. W. Hopman, S. K. Singh, and J. G. van der Hoeven. Validation of transpulmonary thermodilution cardiac output measurement in a pediatric animal model. *Pediatr Crit Care Med*, 9:313–319, 2008.

K. Y. E. Leung, M. van Stralen, M. M. Voormolen, N. de Jong, A. F. W. van der Steen, J. H. C. Reiber, and J. G. Bosch. Improving 3D active appearance model segmentation of the left ventricle with Jacobian tuning. In *Proc SPIE Med Imaging*, volume 6914, page 69143B, San Diego, U.S.A., 2008.

N. Lin, W. C. Yu, and J. S. Duncan. Combinative multi-scale level set framework for echocardiographic image segmentation. *Med Image Anal*, 7(4):529–537, 2003.

R. G. Lopata, M. M. Nillesen, J. P. Van Dijk, I. H. Gerrits, J. M. Thijssen, and C. L de Korte. In vivo 3D elastography of induced skeletal muscle contraction. In *Proc IEEE Int Ultrason Symp*, pages 744–747, Vancouver, Canada, 2006.

R. G. P. Lopata, M. M. Nillesen, I. H. Gerrits, J. M. Thijssen, L. Kapusta, and C. L. de Korte. 4D cardiac strain imaging: methods and initial results. In *Proc IEEE Int Ultrason Symp*, pages 872–875, New York, U.S.A., 2007.

R. G. P. Lopata, M. M. Nillesen, H. H. G. Hansen, I. H. Gerrits, J. M. Thijssen, and C. L de Korte. Performance of two-dimensional displacement and strain estimation techniques using a phased array transducer. *Ultrasound Med Biol*, 35 (5):796–812, 2009.

T. Loupas, W. N. McDicken, and P. L. Allan. An adaptive weighted median filter for speckle suppression in medical ultrasonic images. *IEEE Trans Circuits Syst*, 36 (1):129–135, 1989.

J. Luo, K. Fujikura, S. Homma, and E. E. Konofagou. Myocardial elastography at both high temporal and spatial resolution for the detection of infarcts. *Ultrasound Med Biol*, 33(8):1206–1223, 2007.

J.B. MacQueen. *Some methods for classification and analysis of multivariate observation*. University of California Press, Berkeley, CA, 1967.

F. Mao, J. Gill, D. Downey, and A. Fenster. Segmentation of carotid artery in ultrasound images: Method development and evaluation technique. *Med Phys*, 27:1961–1970, 2000.

C. E. Metz. ROCKIT (computer program), version 0.9.1b, available at: http://www-radiology.uchicago.edu/krl/roc_soft.htm. 1998.

S. C. Mitchell, J. G. Bosch, B. P. F. Lelieveldt, R. J. van der Geest, J. H. C. Reiber, and M. Sonka. 3-D active appearance models: segmentation of cardiac MR and ultrasound images. *IEEE Trans Med Imaging*, 21(9):1167–1178, 2002.

R. C. Molthen, P. M. Shankar, J. M. Reid, F. Forsberg, E. J. Halpern, C. W. Piccoli, and B. B. Goldberg. Comparisons of the Rayleigh and K distribution models using in vivo breast and liver tissue. *Ultrasound Med Biol*, 24:93–100, 1998.

J. Montagnat, M. Sermesant, H. Delingette, G. Malandain, and N. Ayache. Anisotropic filtering for model-based segmentation of 4-D cylindrical echocardiographic images. *Pattern Recognit Lett*, 24(4-5):815–828, 2003.

M. Nakagami. *Statistical methods on radio wave propagation*. Pergamon, Oxford, 1960.

J. A. Noble and D. Boukerroui. Ultrasound image segmentation: A survey. *IEEE Trans Med Imaging*, 25(8):987–1010, 2006.

N.A. Obuchowski. ROC analysis. *AJR Am J Roentgenol*, 184:364–372, 2005.

B.J. Oosterveld, J.M. Thijssen, and W.A. Verhoef. Texture of B-mode echograms: 3-D simulations and experiments of the effects of diffraction and scatterer density. *Ultrason Imaging*, 7:142–160, 1985.

J. Ophir, I. Céspedes, H. Ponnekanti, Y. Yazdi, and X. Li. Elastography: a quantitative method for imaging the elasticity of biological tissues. *Ultrason Imaging*, 13(2):111–134, 1991.

J. Ophir, S. K. Alam, B. Garra, F. Kallel, E. Konofagou, T. Krouskop, and T. Varghese. Elastography: ultrasonic estimation and imaging of the elastic properties of tissues. *Proc.Inst.Mech.Eng [H.]*, 213(3):203–233, 1999.

F. Orderud, G. Kiss, and H. Torp. Automatic coupled segmentation of endo- and epicardial borders in 3D echocardiography. In *Proc IEEE Int Ultrason Symp*, pages 1749–1752, Beijing, China, 2008.

N. Otsu. Threshold selection method from gray-level histograms. *IEEE Trans Syst Man Cybern*, 9:62–66, 1979.

A. Papoulis. *random variables and stochastic processes*. McGraw-Hill, New York, 2 edition, 1976.

H. Ponnekanti, J. Ophir, Y. Huang, and I. Céspedes. Fundamental mechanical limitations on the visualization of elasticity contrast in elastography. *Ultrasound Med Biol*, 21(4):533–543, 1995.

K. Rajpoot, J. A. Noble, V. Grau, C. Szmigielski, and H. Becher. Image-driven cardiac left ventricle segmentation for the evaluation of multiview fused real-time 3-dimensional echocardiography images. In *Proc Med Image Comput Comput Assist Interv Lect Notes Comput Sc*, volume 5762, pages 893–900, London, UK, 2009.

B. I. Raju and M. A. Srinivasan. Statistics of envelope of high-frequency ultrasonic backscatter from human skin in vivo. *IEEE Trans Ultrason Ferroelectr Freq Control*, 49:871–882, 2002.

B. S. Ramamurthy and G. E. Trahey. Potential and limitations of angle-independent flow detection algorithms using radio-frequency and detected echo signals. *Ultrason Imaging*, 13(3):252–268, 1991.

H. Ribbers, R. G. Lopata, S. Holewijn, G. Pasterkamp, J. D. Blankensteijn, and C. L. de Korte. Noninvasive two-dimensional strain imaging of arteries: validation in phantoms and preliminary experience in carotid arteries in vivo. *Ultrasound Med Biol*, 33(4):530–540, 2007.

S.O. Rice. Statistical properties of a sine wave plus random noise. *Bell Syst Tech J*, 27:109–157, 1948.

A. Sarti, C. Corsi, E. Mazzini, and C. Lamberti. Maximum likelihood segmentation of ultrasound images with Rayleigh distribution. *IEEE Trans Ultrason Ferroelectr Freq Control*, 52(6):947–960, 2005.

J. Serra. *Image Analysis and Mathematical Morphology*. Academic Press, New York, 1982.

P. M. Shankar. A model for ultrasonic scattering from tissues based on the K distribution. *Phys Med Biol*, 40:1633–1649, 1995.

P. M. Shankar. A general statistical model for ultrasonic backscattering from tissues. *IEEE Trans Ultrason Ferroelectr Freq Control*, 47:727–736, 2000.

H. Shi and T. Varghese. Two-dimensional multi-level strain estimation for discontinuous tissue. *Phys Med Biol*, 52(2):389–401, 2007.

S. W. Smith, R. F. Wagner, J. M. Sandrik, and H. Lopez. Low contrast detectability and contrast detail analysis in medical ultrasound. *IEEE Trans Sonics Ultrason*, 30:164–173, 1983.

S. W. Smith, H. G. Pavy Jr, and O. T. von Ramm. High-speed ultrasound volumetric imaging system. Part I: transducer design and beam steering. *IEEE Trans Ultrason Ferroelectr Freq Control*, 38(2):100–108, 1991.

E. W. Stacy. Generalization of gamma distribution. *Ann Math Stat*, 33:1187–1192, 1962.

G. R. Sutherland, G. Di Salvo, P. Claus, J. D'hooge, and B. Bijnens. Strain and strain rate imaging: a new clinical approach to quantifying regional myocardial function. *J Am Soc Echocardiogr*, 17(7):788–802, 2004.

M. Tanter, J. Bercoff, L. Sandrin, and M. Fink. Ultrafast compound imaging for 2-D motion vector estimation: application to transient elastography. *IEEE Trans Ultrason Ferroelectr Freq Control*, 49(10):1363–1374, 2002.

J. M. Thijssen. Ultrasonic speckle formation, analysis and processing applied to tissue characterization. *Pattern Recognition Lett*, 24:659–675, 2003.

J. M. Thijssen and B. J. Oosterveld. Performance of echographic equipmentand potentials for tissue characterization. In M.A. Viergever and A. Todd-Prokopek, editors, *eds. NATO ASI Series F: Computer and System Sciences*, volume 39, pages 455–468. Springer, Berlin, 1988.

F. M. Valckx, J. M. Thijssen, A. J. van Geemen, J. J. Rotteveel, and R. Mullaart. Calibrated parametric medical ultrasound imaging. *Ultrason Imaging*, 22(1): 57–72, 2000.

N. J. M. van Hees, J. M. Thijssen, R. W. Huyskens, G. Weijers, M. M. Nillesen, C. L. de Korte, and C. Katsaros. Quantitative ultrasound imaging of healthy and reconstructed cleft lip: A feasibility study. *Cleft Palate Craniofac J*, 44(3): 261–268, 2007.

M. van Stralen, J. G. Bosch, M. M. Voormolen, G. van Burken, B. J. Krenning, R. J. van Geuns, C. T. Lancée, N. de Jong, and J. H. Reiber. Left ventricular volume estimation in cardiac three-dimensional ultrasound: a semiautomatic border detection approach. *Acad Radiol*, 12(10):1241–1249, 2005.

M. van Stralen, K. Y. E. Leung, M. M. Voormolen, N. de Jong, A. F. W. van der Steen, J. H. C. Reiber, and J. G. Bosch. Automatic segmentation of the left ventricle in 3D echocardiography using active appearance models. In *Proc IEEE In Ultrason Symp*, pages 1480–1483, New York, NY, U.S.A., 2007.

T. Varghese and J. Ophir. A theoretical framework for performance characterization of elastography: the strain filter. *IEEE Trans Ultrason Ferroelectr Freq Control*, 44(1):164–172, 1997.

T. Varghese, J. Ophir, and I. Céspedes. Noise reduction in elastograms using temporal stretching with multicompression averaging. *Ultrasound Med Biol*, 22(8): 1043–1052, 1996.

J. T. Verhoeven and J. M. Thijssen. Improvement of lesion detectability by speckle reduction filtering: A quantitative study. *Ultrason Imaging*, 15:181–204, 1993.

J. T. Verhoeven, J. M. Thijssen, and A. G. Theeuwes. Improvement of lesion detection by echographic image processing: Signal-to-noise-ratio imaging. *Ultrason Imaging*, 13:238–251, 1991.

O. T. von Ramm, S. W. Smith, and H.G. Pavy Jr. High-speed ultrasound volumetric imaging system. Part II: parallel processing and image display. *IEEE Trans Ultrason Ferroelectr Freq Control*, 38(2):109–115, 1991.

R. F. Wagner, S. W. Smith, J. M. Sandrik, and H. Lopez. Statistics of speckle in ultrasound B-scans. *IEEE Trans Sonics Ultrason*, 30:156–183, 1983.

V. Walimbe, V. Zagrodsky, and R. Shekhar. Fully automatic segmentation of left ventricular myocardium in real-time three-dimensional echocardiography. In *Proc SPIE Med Imaging*, volume 6144, page 61444H, San Diego, U.S.A., 2006.

W. Weibull. A statistical distribution function of wide applicability. *J Appl Mech-Trans ASME*, 18:293–297, 1951.

P. Yan, C. X. Jia, A. Sinusas, K. Thiele, M. O'Donnell, and J. S. Duncan. LV segmentation through the analysis of radio frequency ultrasonic images. *Inf Process Med Imaging*, 20:233–244, 2007.

W.J. Youden. Index for rating diagnostic tests. *Cancer*, 3:32–35, 1950.

Y. Zhu, X. Papademetris, A. Sinusas, and J. S. Duncan. Segmentation of myocardial volumes from real-time 3D echocardiography using an incompressibility constraint. In *Proc Med Image Comput Comput Assist Interv Lect Notes Comput Sc*, volume 4791, pages 44–51, Brisbane, Australia, 2007.

Y. Zimmer, R. Tepper, and S. Akselrod. A two-dimensional extension of minimum cross entropy thresholding for the segmentation of ultrasound images. *Ultrasound Med Biol*, 22:1183–1190, 1996.

Publications

Journal papers

M. M. Nillesen, R. G. Lopata, I. H.Gerrits, L. Kapusta, H. J. Huisman, J. M. Thijssen, and C. L. de Korte. Segmentation of the heart muscle in 3-D pediatric echocardiographic images. *Ultrasound Med Biol*, 33(9):1453-1462, 2007.

N. J. M. van Hees, J. M. Thijssen, R. W. Huyskens, G. Weijers, **M. M. Nillesen**, C. L. de Korte, and C. Katsaros. Quantitative ultrasound imaging of healthy and reconstructed cleft lip: A feasibility study. *Cleft Palate Craniofac J*, 44(3):261-268, 2007.

M. M. Nillesen, R. G. Lopata, I. H. Gerrits, L. Kapusta, J. M. Thijssen, and C. L. de Korte. Modeling envelope statistics of blood and myocardium for segmentation of echocardiographic images. *Ultrasound Med Biol*, 34(4):674-680, 2008.

M. M. Nillesen, R. G. Lopata, W. P. de Boode, I. H. Gerrits, H. J. Huisman, J. M. Thijssen, L. Kapusta, and C. L. de Korte. In vivo validation of cardiac output assessment in non-standard 3D echocardiographic images, *Phys Med Biol*, 54(7):1951-1962, 2009.

R. G. P. Lopata, H. H. G. Hansen, **M. M. Nillesen**, J. M. Thijssen, and C. L. de Korte. Comparison of one-dimensional and two-dimensional least-squares strain estimators for phased array displacement data. *Ultrason Imaging*, 31(1):1-16, 2009.

R. G. Lopata, **M. M. Nillesen**, H. H. G. Hansen, I. H. Gerrits, J. M. Thijssen, and C. L. de Korte. Performance evaluation of methods for two-dimensional displacement and strain estimation using ultrasound radio frequency data. *Ultrasound Med Biol*, 35(5):796-812, 2009.

R. G. Lopata, **M. M. Nillesen**, H. H. Hansen, I. H. Gerrits, J. M. Thijssen, and C. L. de Korte. Performance of two dimensional displacement and strain estimation techniques using a phased array transducer, *Ultrasound Med Biol*, 35(12):2031-2041, 2009.

R. G. Lopata, **M. M. Nillesen**, C. N. Verrijp, S. K. Singh, M. M. Lammens, J. A. van der Laak, H. B. van Wetten, J. M. Thijssen, L. Kapusta, and C. L. de Korte. Cardiac biplane strain imaging: initial in vivo experience. *Phys Med Biol*, 55(4):963-79, 2010.

R. G. P. Lopata, H. H. G. Hansen, **M. M. Nillesen**, J. M. Thijssen, L. Kapusta, and C. L. de Korte. Methodical study on the estimation of strain in shearing and rotating structures using radio frequency ultrasound based 1D and 2D strain estimation techniques. *IEEE Trans Ultrason Ferroelectr Freq Control*, 57(4) 855-865, 2010.

M. M. Nillesen, R. G. Lopata, H. J. Huisman, J. M. Thijssen, L. Kapusta, and C. L. de Korte. Correlation based 3-D segmentation of echocardiographic images using radio frequency data, *submitted*.

Peer-reviewed conference proceedings

C. L. de Korte, R. G. P. Lopata, **M. M. Nillesen**, G. Weijers, N. J. van Hees, I. H. Gerrits, C. Katsaros, L. Kapusta, and J. M. Thijssen. Ultrasound strain imaging: from nano-scale motion detection to macro-scale functional imaging. *Proc Int Symp Biomed Imaging*, 544-547, 2008.

M. M. Nillesen, R. G. P. Lopata, I. H. Gerrits, H. J. Huisman, J. M. Thijssen, L. Kapusta, and C. L. de Korte. Segmentation of 3D cardiac ultrasound images using correlation of radio frequency data. *Proc Int Symp Biomed Imaging*, 522-525, 2009.

M. M. Nillesen, R. G. P. Lopata, H. J. Huisman, J. M. Thijssen, L. Kapusta, and C. L. de Korte. 3D Cardiac segmentation using temporal correlation of radio frequency ultrasound images. *Proc Med Image Comput Comput Assist Interv Lect Notes Comput Sc*, 5762:927-934; 2009.

Other conference proceedings

R. G. P. Lopata, **M. M. Nillesen**, I. H. Gerrits, L. Kapusta, J. M. Thijssen, and C. L. de Korte. 3D Strain estimation for isotropic and anisotropic materials. *Proc IEEE Int Ultrason Symp*, 731-734, 2005.

M. M. Nillesen, R. G. P. Lopata, I. H. Gerrits, L. Kapusta, H. J. Huisman, J. M. Thijssen, and C. L. de Korte. Three dimensional segmentation of the heart muscle using image statistics. *Proc SPIE Med Imaging*, 6147:204-212, 2006.

M. M. Nillesen, R. G. P. Lopata, I. H. Gerrits, L. Kapusta, H. J. Huisman, J. M. Thijssen, and C. L. de Korte. 3D Segmentation of the heart muscle in real-time 3D echocardiographic sequences using image statistics. *Proc Computers in Cardiology*, 129-132, 2006.

R. G. P. Lopata, **M. M. Nillesen**, I. H. Gerrits, L. Kapusta, J. M. Thijssen, and C. L. de Korte. In vivo 3D cardiac and skeletal muscle strain estimation. *Proc IEEE Int Ultrason Symp*, 744-747, 2006.

M. M. Nillesen, R. G. P. Lopata, I. H. Gerrits, L. Kapusta, H. J. Huisman, J. M. Thijssen, and C. L. de Korte. 3D Segmentation of the heart muscle in real-time 3D echocardiographic sequences using image statistics. *Proc IEEE Int Ultrason Symp*, 1987-1990, 2006.

C. L. de Korte, R. G. P. Lopata, H. H. G. Hansen, **M. M. Nillesen**, I. H. Gerrits, L. Kapusta, and J. M. Thijssen, Cardio vascular ultrasound elastography. *Proc Int Congr of Acoustics*, 394-395, 2007.

I. H. Gerrits, **M. M. Nillesen**, R. G. P. Lopata, J. P. T. Rijk, J. M. Thijssen, and C. L. de Korte. A robust deformable simplex mesh model with temporal signal de-correlation constraints in echocardiography. *Proc IEEE Int Ultrason Symp*, 1484-1487, 2007.

R. G. P. Lopata, **M. M. Nillesen**, I. H. Gerrits, J. M. Thijssen, L. Kapusta, and C. L. de Korte. 4D Cardiac strain imaging: methods and initial results. *Proc IEEE Int Ultrason Symp*, 872-875, 2007.

M. M. Nillesen, R. G. P. Lopata, I. H. Gerrits, L. Kapusta, H. J. Huisman, J. M. Thijssen, and C. L. de Korte. Three-dimensional cardiac image segmentation using adaptive filtering and 3D deformable simplex meshes. *Proc IEEE Int Ultrason Symp*, 1468-1471, 2007.

R. G. P. Lopata, **M. M. Nillesen**, I. H. Gerrits, L. Kapusta, J. M. Thijssen and C. L. de Korte. BiPlane cardiac strain imaging: a study on valvular aortic stenosis. *Proc IEEE Int Ultrason Symp*, 950-953, 2008.

M. M. Nillesen, R. G. P. Lopata, W.P. de Boode, I. H. Gerrits, H. J. Huisman, J. M. Thijssen, L. Kapusta, and C. L. de Korte. Cardiac output estimation in non-standard echocardiographic images. *Proc IEEE Int Ultrason Symp*, 1745-1748, 2008.

R. G. P. Lopata, **M. M. Nillesen**, I. H. Gerrits, L. Kapusta, J. M. Thijssen, and C. L. de Korte. 3D Cardiac strain imaging using a novel tracking method. *Proc 4th Eur Conf Int Fed Med Biol Eng*, 22:697-700, 2009.

R. G. P. Lopata, H. H. G. Hansen, **M. M. Nillesen**, J. M. Thijssen, and C. L. de Korte. A novel 2D displacement estimation method using free-shape kernels of radio frequency ultrasound data in rotating and shearing structures. *Proc IEEE Int Ultrason Symp* 2009, *in press*

M. M. Nillesen, R. G. P. Lopata, I. H. Gerrits, L. Kapusta, H. J. Huisman, J. M. Thijssen, and C. L. de Korte. Segmentation of 3D echocardiographic images using deformable simplex meshes and adaptive filtering. *Proc 4th Eur Conf Int Fed Med Biol Eng*, 22:550-554, 2009.

Conferences presentations

M. M. Nillesen, R. G. P. Lopata, I. H. Gerrits, L. Kapusta, H. J. Huisman, J. M. Thijssen, and C. L. de Korte. Three dimensional segmentation of the heart muscle using image statistics. *SPIE Med Imaging, San Diego, CA, U.S.A.,* 2006.

M. M. Nillesen, R. G. P. Lopata, I. H. Gerrits, L. Kapusta, H. J. Huisman, J. M. Thijssen, and C. L. de Korte. 3D Segmentation of the heart muscle in real-time 3D echocardiographic sequences using image statistics. *Computers in Cardiology, Valencia, Spain,* 2006.

M. M. Nillesen, R. G. P. Lopata, I. H. Gerrits, L. Kapusta, H. J. Huisman, J. M. Thijssen, and C. L. de Korte. 3D Segmentation of the heart muscle in real-time 3D echocardiographic sequences using image statistics. *IEEE Int Ultrason Symp, Vancouver, BC, Canada*, 1987-1990, 2006.

M. M. Nillesen, R. G. P. Lopata, I. H. Gerrits, L. Kapusta, H. J. Huisman, J. M. Thijssen, and C. L. de Korte. Three-dimensional cardiac image segmentation using adaptive filtering and 3D deformable simplex meshes. *IEEE Int Ultrason Symp, New York, NY, U.S.A.*, 2007.

M. M. Nillesen, R. G. P. Lopata, W. P. de Boode, I. H. Gerrits, H. J. Huisman, J. M. Thijssen, L. Kapusta, and C. L. de Korte. Cardiac output estimation in non-standard echocardiographic images. *IEEE Int Ultrason Symp, Beijing, China*, 2008.

M. M. Nillesen, R. G. P. Lopata, I. H. Gerrits, L. Kapusta, H. J. Huisman, J. M. Thijssen, and C. L. de Korte. Segmentation of 3D echocardiographic images using deformable simplex meshes and adaptive filtering. *4th Eur Conf Int Fed*

Med Biol Eng, Antwerpen, Belgium, 2008.

M. M. Nillesen, R. G. P. Lopata, I. H. Gerrits, H. J. Huisman, J. M. Thijssen, L. Kapusta, and C. L. de Korte. Segmentation of 3D cardiac ultrasound images using correlation of radio frequency data. *Int Symp Biomed Imaging, Boston, MA, U.S.A.*, 522-525, 2009.

M. M. Nillesen, R. G. P. Lopata, H. J. Huisman, J. M. Thijssen, L. Kapusta, and C. L. de Korte. Segmentation in 3D echocardiography based on temporal correlation of the radio frequency Signal. *IEEE Int Ultrason Symp, Rome, Italy*, 2009.

M. M. Nillesen, R. G. P. Lopata, H. J. Huisman, J. M. Thijssen, L. Kapusta, and C. L. de Korte. 3D Cardiac segmentation using temporal correlation of radio frequency ultrasound images. *Int Conf Med Image Comput Comput Assist Interv, London, UK*, 2009.

Awards

M. M. Nillesen, R. G. P. Lopata, I. H. Gerrits, L. Kapusta, H. J. Huisman, J. M. Thijssen, and C.L. de Korte. Segmentation of the myocardium in real-time 3D pediatric echocardiographic images. *First Dutch Conf Biomed Eng, Egmond aan Zee, the Netherlands*, 2007. ***Best poster presentation.***

M. M. Nillesen, R. G. P. Lopata, W. P. de Boode, I. H. Gerrits, H. J. Huisman, J. M. Thijssen, L. Kapusta, and C. L. de Korte. Cardiac output bepaling in niet-standaard 3D echocardiografische beelden. *Nieuw Licht Conf NVKF, Kaatsheuvel, Netherlands*, 2008. ***Best student poster presentation.***

Dankwoord

Eind april 2010. Een prachtige voorjaarsochtend, de natuur staat letterlijk op springen. Op het moment dat deze nieuwe lente volop begonnen is, rond ik een belangrijke periode in mijn leven af met het schrijven van dit dankwoord. Het proefschrift is af en markeert de afsluiting van een onderzoeksperiode. Een periode waarin ik met veel plezier onderzoek heb gedaan op het gebied van de 3D echocardiografie. Voor mij een zeer interessant vakgebied, waarin techniek en medische kennis op een mooie manier samenkomen en elkaar versterken.
Mijn enthousiasme voor dit onderzoek en de totstandkoming van dit proefschrift zijn te danken aan een groot aantal mensen. Graag wil ik iedereen die een bijdrage heeft geleverd hiervoor bedanken, waaronder enkelen in het bijzonder.

Allereerst gaat mijn dank uit naar mijn promotor Prof. dr. ir. J.M. Thijssen. Beste Han, je enthousiasme, kritische blik en motivatie om alles tot op de bodem toe uit te zoeken hebben mij gestimuleerd om zeer grondig onderzoek te doen. Als senior deskundige op het gebied van ultrageluid stond je bijna aan de wieg van de echocardiografie. Je kennis van dit vakgebied was voor mij dan ook van onschatbare waarde, mede doordat je steeds weer bereid was mij de finesses van de ultrageluidstechnieken bij te brengen. Naast onze uitstekende vakinhoudelijke samenwerking denk ik met veel plezier terug aan ons gezamenlijke muzikale optreden op de Tissue Elasticity Conference in Vlissingen.

Mijn copromotor dr. ir. Chris de Korte, de drijvende kracht achter het 3D cardiac imaging project. Jouw enorme hoeveelheid ideeën en positieve instelling hebben mij enorm gemotiveerd, juist ook op de momenten dat het wat tegenzat. Je hebt me geleerd in te zien wat de sterke punten van het onderzoek zijn en hoe je de wetenschap moet verkopen. Dat is een niet te onderschatte vaardigheid in de onderzoekswereld. Ik heb je ongeëvenaarde betrokkenheid en open-mind (je deur stond letterlijk altijd open) zeer gewaardeerd. Ik kijk er naar uit onze samenwerking de komende jaren voort te zetten.

Een andere belangrijke kracht achter het succes van dit onderzoek was mijn copromotor dr. Livia Kapusta. Livia, je was als zeer betrokken kindercardiologe mijn steun en toeverlaat op het gebied van de cardiologie. Als wiskundige schoot mijn medische expertise natuurlijk te kort. Jij hebt die expertise als geen ander aangevuld. Je zorgde ervoor dat het onderzoek niet verzandde in technische details en kunstjes, maar dat we ons bleven concentreren op dat wat van belang was voor de kindercardiologie. Door je warme persoonlijkheid heb ik het samenwerken met jou als zeer plezierig ervaren.

Prof. dr. R. de Groot wil ik graag bedanken voor zijn rol als promotor bij dit onderzoek. Bovendien heeft hij mij de kans gegeven om naast mijn wetenschappelijke kwaliteiten ook mijn muzikale kwaliteiten te kunnen laten zien binnen het UMC St Radboud. Op zijn uitnodiging om samen met Caroline te musiceren tijdens het kerstdiner van kindergeneeskunde ben ik dan ook graag ingegaan. Dit was het begin van een heel aantal mooie muzikale optredens.

De leden van de manuscriptcommissie, Prof. dr. C. C. A. M. Gielen, Prof. dr. J. L. R. M. Smeets en Dr. ir. J. G. Bosch wil ik graag hartelijk bedanken voor de vlotte afhandeling van de beoordeling van mijn proefschrift. *I would also like to thank Prof. dr. T. Delhaas, Prof. dr. ir. W. M. Niessen, Prof. dr. J. D'hooge, Dr. ir. H. J. Huisman and Prof. J. A. Noble, for being a member of my doctoral committee. Thank your for your time and effort in reading my thesis.*

Al mijn collega's van het Klinisch Fysisch Laboratorium. Hartelijk dank voor de prettige samenwerking, ondersteuning en alle gezelligheid. Mede dankzij de goede sfeer op de afdeling zijn het fijne onderzoeksjaren geweest. De grappige, zeer creatieve posters die er na het winnen van een prijs op een conferentie op mijn kamer hingen, zal ik niet vergeten. In het bijzonder wil ik een paar mensen extra bedanken.
Jan Menssen, zonder jouw programmeerkennis, weliswaar van de oude stempel maar uiterst up-to-date, was het omzetten van mijn ideeën naar een goed werkend computerprogramma nooit gelukt. Dank voor al je hulp. Dank ook aan Gert Weijers, voor alle prettige ondersteuning bij het maken van de echo opnamen en het beheren van de enorme hoeveelheden data. Sonja van de Ven, veel dank voor al je ondersteuning, perfecte voorbereiding van onze conferentiereizen en je gezelligheid.
En dan Richard Lopata. Als er twee mensen in hetzelfde schuitje zaten, dan waren wij dat wel. Als eerste promovendi op de afdeling lag er een promotie traject voor ons vol onzekerheden. Van het allereerste begin, toen er alleen nog maar een berg schijnbaar ongeordende getallen uit het echo apparaat kwam, naar onze eerste stappen in het internationale conferentie circuit met spannende eerste presentaties van ons onderzoek. Onze 5-jarige intensieve samenwerking is mij goed bevallen, zeker ook door je onvervalste Brabantse humor. Hopelijk komt er nog een mooi gezamenlijk vervolgonderzoek.

Mijn dank gaat ook uit naar Dr. ir. Hans Bosch, Dr. Esther Leung en Dr. Marijn van Stralen voor hun betrokkenheid en inspiratie, evenals de gezelligheid tijdens de conferenties die we samen bezochten.

Dr. ir. Henkjan Huisman wil ik bedanken voor alle ondersteuning op het gebied van de beeldbewerking. Zeker in de eerste periode was dit van grote waarde. Heel gezellig was het om uiteindelijk toch een keer samen met je op conferentiereis te gaan en wel naar de prestigieuze MICCAI conference in Londen.

Dr. Willem de Boode dank ik voor de mogelijkheid om unieke echo opnamen te kunnen maken tijdens zijn cardiac output experimenten. Onze plezierige samenwerking heeft geleid tot een mooi artikel.

Veel dank ben ik verschuldigd aan Bob Rijk en Imke Janssen van het kinderhartcentrum. Bob, zonder jou hadden we nooit de mooie 3D opnamen bij kinderen kunnen maken die we zo hard nodig hadden. Je passie voor 3D echo en nieuwe technieken was overduidelijk en inspirerend. Imke, de laatste paar jaar was ook jij zeer geïnteresseerd in de 3D echo en heb je ons enorm geholpen bij het maken van de opnamen. Dank je wel voor al jullie inzet, geduld en gezelligheid.

Dank aan alle kinderen, die mee hebben gedaan aan ons 3D echo onderzoek. Zonder hen was dit proefschrift nooit tot stand gekomen.

Janneke Kammeraad, dank je wel voor je adviezen op het gebied van de kindercardiologie. Het was heel gezellig samen (onder andere op 3D echo cursus in Groenendael) en leerzaam om met je te discussiëren over de echocardiografie.

In een werkomgeving met overwegend mannen is het soms erg verfrissend om uitgebreid bij te praten met dames onder elkaar. Anja Vinck en Renske Raaijmakers wil ik bedanken voor de gezellige thee- en lunchpauzes, al waren de mannen herhaaldelijk verontwaardigd dat ik (weer) niet met hen mee ging lunchen.

Mijn paranimfen Caroline van de Steeg en Bas Rooijmans, ik vind het heel bijzonder dat jullie op deze dag naast mij willen staan.

Buiten het werk vond ik veel gezelligheid bij goede vrienden. Ook het piano en altviool spelen in vele bezettingen met vele gezellige mensen vormde een zeer goede afleiding voor het soms taaie promotie onderzoek.

Anne-Fleur, mijn lieve zusje, met grote belangstelling heb je steeds mijn onderzoek gevolgd. Ik ben inmiddels onder de indruk van je kennis van allerlei technische details. Dank voor al je gezelligheid, humor en belangstellende telefoontjes.

Zeer speciale dank gaat uit naar mijn ouders. Lieve mam, papa en jij hebben mij de beste basis gegeven die je je als kind kunt wensen. Jullie onvoorwaardelijke steun en stimulans om dat te doen wat ik wilde en waar ik goed in ben zijn van zeer grote waarde geweest. Ik heb vast wat geërfd van jouw doorzettingsvermogen en optimisme. Dat kwam zeer goed van pas tijdens het promotietraject.
Lieve pap, wat had ik het je gegund om deze periode van mijn leven mee te mogen maken. Je zou er ongelooflijk trots op geweest zijn dat ik dit bereikt heb. Dat is zeker ook dankzij jouw wijsheid en dankzij het analytisch vermogen dat je mij hebt meegegeven.

Lieve Bart, de laatste twee jaar van mijn promotie kwam jij in mijn leven, een groot geluk. Dank je wel voor al je steun, gezelligheid en de rust die je bracht door er gewoon te zijn. Ik vind het fantastisch om mijn leven met je te delen en kijk uit naar de bijzondere periode die voor ons ligt.

Curriculum Vitae

Maartje Marjolein Nillesen was born in Heemstede, the Netherlands, on February 15, 1974. She graduated in 1992 at the Stedelijk Gymnasium Haarlem. She studied mathematics and music for one year at Leeds University, UK.
Back in Holland, she continued studying mathematics and music (piano) at the University of Groningen and the Conservatory of Groningen respectively. In 1999, she received her Master's Degree in mathematics from the University of Groningen. During her research internship at Thales (Hengelo), she investigated the optimization of controller design.
After graduation she worked in the field of speech processing for several years, focusing on speech recognition by using a model of the human inner ear. In 2004 she joined the Clinical Physics Laboratory of the Radboud University Nijmegen Medical Centre where she has been working towards her Ph.D. degree, investigating 3D segmentation in pediatric echocardiographic images.
Since May 2010, she continued her work on 3D segmentation as a post-doctoral researcher at the Radboud University Nijmegen Medical Centre. Her research interests include 3D medical image segmentation, assessment of cardiac function and tissue characterization.

Automated Segmentation in 3D Pediatric Echocardiographic Images Maartje Nillesen